STUDY OF STAR FORMATION REGIONS
WITH MOLECULAR HYDROGEN EMISSION LINES

by

SOOJONG PAK , B.S., M.A.

DISSERTATION

Presented to the Faculty of the Graduate School of

The University of Texas at Austin

in Partial Fulfillment

of the Requirements

for the Degree of

DOCTOR OF PHILOSOPHY

THE UNIVERSITY OF TEXAS AT AUSTIN

August 1997

STUDY OF STAR FORMATION REGIONS
WITH MOLECULAR HYDROGEN EMISSION LINES

APPROVED BY
DISSERTATION COMMITTEE:

Supervisor: _____

_____

_____

_____

_____

This dissertation is dedicated to

my parents, *Kwang-Hyun Pak* and *Bok-Hee Lee,*

my parents-in-law, *Sang-Soon Lee* and *Kyung-Soon Lee,*

and

my advisor, *Prof. Daniel T. Jaffe,*

for their efforts to make an astronomer.

Acknowledgements

I thank my dissertation committee members, Harriet Dinerstein, Bruce Draine, John Lacy, and Daniel Lester, for their helpful comments on my dissertation. Harriet Dinerstein carefully read my dissertation and gave many critical comments. I consulted John Lacy about instrumentation, science, and my future. Neal Evans, even though he was not in my committee, helped me to learn astronomy. I thank Gordon Stacey for the opportunity to observe at the Palomar where I learned a lot from him. I was lucky to collaborate with Ewine van Dishoeck, when I was stuck in PDR models. It was helpful for me to discuss with Kenji Mochizuki about the PDR models. I thank the UT FPS project members, Mike Luhman, Luke Keller, and Eric Klumpe, with whom I spent many hours in the lab and in observatories. Especially, Luke Keller always kindly helped my works.

I thank Minho Choi for his Monte Carlo code and for his not complaining about my endless questions. I also thank the other Korean astronomers in the Astronomy Department, Soon-Wook Kim, and Jungyeon Cho, for their personal support and relationship during my six-years in the graduate program.

Finally, I should thank my family. My elder brother, Soo-Keun Pak, my elder sister, Suehee Pak, and their families support my works as well as my life. My daughter, Seoyoung (Elaine), makes me happy. I cannot find the right word for my wife, Soyoung Lee.

STUDY OF STAR FORMATION REGIONS
WITH MOLECULAR HYDROGEN EMISSION LINES

Publication No. _____

Soojong Pak , Ph.D.
The University of Texas at Austin, 1997

Supervisor: Daniel T. Jaffe

The goal of my dissertation is to understand the large-scale, near-infrared (near-IR) H_2 emission from the central kiloparsec (kpc) regions of galaxies, and to study the structure and physics of photon-dominated regions (or photodissociation regions, hereafter PDRs). In order to explore the near-IR H_2 lines, our group built the University of Texas near-IR Fabry-Perot Spectrometer optimized for observations of extended, low surface brightness sources. In this instrument project, I designed and built a programmable high voltage DC amplifier for the Fabry-Perot piezoelectric transducers, a temperature-controlled cooling box for the Fabry-Perot etalon, instrument control software, and data reduction software. With this instrument, we observed H_2 emission lines in the inner 400 pc of the Galaxy, the central $\sim$ 1 kpc of NGC 253 and M82, and the star formation regions in the Magellanic Clouds. We also observed the Magellanic Clouds in the CO $J = 1 \rightarrow 0$ line. We found that the H_2 emission is very extended in the central kpc of the galaxies and is mostly UV-excited. The ratios of the H_2 (1,0) S(1) luminosities to the far-IR continuum luminosities in the central kpc regions do not change from the Galactic center to starburst galaxies and to ultraluminous IR bright galaxies. Using the data from

the Magellanic Clouds, we studied the microscopic structure of star forming clouds. We compiled data sets including our H_2 (1,0) S(1) and CO $J = 1 \rightarrow 0$ results and published [C II] and far-IR data from the Magellanic Clouds, and compared these observations with models we made using a PDR code and a radiative transfer code. Assuming the cloud is spherical, we derived the physical sizes of H_2, [C II], and CO emission regions. The average cloud size appears to increase as the metallicity decreases. Our results agree with the theory of photoionization-regulated star formation in which the interplay between the ambipolar diffusion and ionization by far-UV photons determines the size of stable clouds.

Table of Contents

Chapter 1

Introduction

1.1 Background

In the last three decades, astronomers have discovered, primarily through radio and infrared (IR) observations, sites where interstellar molecular clouds have recently collapsed to form new stars. In such regions, the dust is opaque at visible wavelengths. While radio observations (e.g., radio continuum, hydrogen recombination lines) identify H II regions, and millimeter observations (e.g., CO $J = 1 \rightarrow 0$ lines) trace the dynamics of the ambient clouds (Lada 1997), IR observations (e.g., far-IR continuum, [C II] 158 μm, near-IR H_2 emission lines) are unique probes to clarify the complex relationship between the new-born stars and their environment.

1.1.1 Photon-Dominated Regions

Young massive stars emit intense ultraviolet (UV) radiation. Photons in the Lyman continuum, $\lambda < 91.2$ nm, are absorbed in H II regions. The remaining far-UV ($91.2 < \lambda < 206.2$ nm) photons penetrate into nearby molecular clouds where the far-UV photons can dissociate molecules, ionize atoms, and eject electrons from dust grains. From the surface of the cloud, or the H^+/H transition layer, H becomes H_2 typically at $A_V = 1 - 2$ mag, C^+ becomes C and then CO at $A_V = 2 - 4$ mag, and any O not in CO is converted to O_2 at $A_V = 5 - 10$ mag (Tielens & Hollenbach 1985; Burton 1992). These sur-

face regions are called photon-dominated regions or photodissociation regions (hereafter PDRs).

Gas in the outer regions ($A_V < 4$ mag) of PDRs is heated to several hundred K by electrons photoelectrically ejected from dust grains and by collisional de-excitation of UV-pumped H_2 molecules. In this environment, the gas is cooled by far-IR fine structure lines of abundant atoms, e.g., [O I] 63 μm and [C II] 158 μm; and by submillimeter lines of CO. These physical processes could affect the process or mode of star formation (Parravano 1988). It is generally believed that magnetic fields play an important role in supporting the cloud against gravitational collapse. In the photoionization-regulated star formation picture (McKee 1989), the higher ionization fraction in PDRs impedes ambipolar diffusion and inhibits star formation.

1.1.2 C^+

The ionization potential of neutral carbon is 11.3 eV (or 101.1 nm), and most of the carbon atoms are ionized at $A_V < 4$ mag in the PDR. In the ground electronic state of ^2P, C^+ is easily excited from $J = 1/2$ to $J = 3/2$, because the energy level difference is low, $\Delta E/k = 92$ K, and the critical density of the transition is low, $n_{crit} \simeq 3 \times 10^3$ cm^{-3}. The [C II] 158 μm fine structure line is therefore one of the most important coolants in the PDRs and one of the most important tracers of photodissociated material (Crawford et al. 1985; Genzel, Harris, & Stutzki 1989).

1.1.3 H_2

Molecular hydrogen is the most abundant molecule in the molecular clouds. H_2, however, has the lowest moment of inertia of any molecule, and the rotational energy levels are too high ($\Delta E/k \simeq 500$ K, from $J = 0$ to 2) to be collisionally excited in the cold gas ($T < 50$ K at $A_V > 4$ mag). In some special

circumstances, ro-vibrational levels of H_2 are thermally excited in gas heated by shocks, or non-thermally excited by UV fluorescence. X-rays non-thermally excite the H_2 by generating X-ray photoelectrons. Even though X-ray excitation may be important in some circumstances (e.g., supernova remnants, active galactic nuclei; Lepp & McCray 1983; Gredel & Dalgarno 1995; Tiné et al. 1997), its significance in ordinary star formation regions has not been widely demonstrated by observations.

UV-Excitation

H_2 in the ground state absorbs $91.2 - 110.8$ nm photons in the $B^1\Sigma_u^+ - X^1\Sigma_g^+$ Lyman and $C^1\Pi_u - X^1\Sigma_g^+$ Werner bands, and the electronic excitations are followed by fluorescence. About 10 % of the electronically excited H_2 molecules dissociate, and the remaining 90% populate various ro-vibration levels in the electronic ground state. Since H_2 has no electronic dipole moment, the ro-vibration levels decay by electronic quadrupole transitions, principally in the near-IR, on a time scale of 10^6 sec (Black & van Dishoeck 1987 and references therein).

If the density is low ($n(H_2) < 5 \times 10^4$ cm^{-3}) the relative line intensities of the H_2 ro-vibrational lines are insensitive to density or to the UV field strength because the populations of the ground-state energy levels are controlled purely by the radiative cascade (Black and van Dishoeck 1987). At densities $\geq 5 \times 10^4$ cm^{-3}, collisional de-excitation of UV-pumped H_2 thermalizes the ro-vibrational level populations and H_2 is an important heating source for the gas. If the PDR boundaries become sufficiently warm ($T > 1000$ K) and dense, collisional excitation thermalizes the low vibrational ($v \leq 2$) level populations (Sternberg and Dalgarno 1989).

1.2   Motivation for This Project

The goal of my dissertation project is to identify the excitation mechanism for large-scale H_2 emission from the central kpc regions of galaxies and to study the structure of individual PDRs. The knowledge I gain will help us to explore the physical conditions in the central star formation regions in starburst galaxies and luminous infrared galaxies.

The central regions of starburst galaxies and luminous IR galaxies emit strongly in ro-vibrational H_2 lines. H_2 emission can be an important tracer of dynamical activity in the molecular ISM, e.g., shocked material such as in bipolar molecular outflows and in supernova remnants, and of the interaction of far-UV photons from massive young stars with molecular gas, e.g., PDRs. It may also indicate where X-rays from AGNs interact with molecular gas. The identification of the H_2 excitation mechanism is important if we are to understand the physical conditions in the molecular gas. Based on H_2 line ratios of (2,1) S(1) to (1,0) S(1), some authors have argued that the H_2 emission from the central regions of galaxies is predominantly UV-excited (Puxley, Hawarden, & Mountain 1988; Doyon, Wright, & Joseph 1994), while others have argued that it is predominantly excited by shocks (Fisher et al. 1987; Moorwood & Oliva 1990, 1994; Koornneef & Israel 1996). Based on our own experience with observations of the (2,1) S(1) line, the ratio of (2,1) S(1) to (1,0) S(1) is not a very reliable indicator of the excitation mechanism. The strength of the H_2 (2,1) S(1) line is affected by telluric absorption and by telluric OH emission; the detected line flux is therefore usually very uncertain. In addition, the absorption features of late-type stars in the galaxies make flux calibration more difficult. For example, Doyon, Joseph, & Wright (1994) measured the (2,1) S(1)/(1,0) S(1) ratio in NGC 3256 as 0.39 ± 0.06; however, Moorwood & Oliva (1994) measured the ratio in the same galaxy as 0.13 ± 0.03. The (2,1) S(1)/(1,0) S(1) ratio also has a theoretical defect. Sternberg & Dalgarno

(1989) and Draine & Bertoldi (1996) numerically calculated the level populations of the UV-excited H_2, and concluded that the populations are thermalized in dense gas and that the (2,1) S(1)/(1,0) S(1) ratio resembles the ratio from shocked gas.

In order to identify the source of the H_2 excitation and to study the implication of the H_2 emission from other galaxies, we need to compare the H_2 emission with other PDR probes, e.g., [C II], CO $J = 1 \rightarrow 0$, far-IR. We targeted the inner few 100 pc of the Galaxy as the nearest sample of the central regions of galaxies. We also targeted the clouds in Galactic star formation regions and the clouds in the Magellanic Clouds to learn about the individual structure of the PDRs and the characteristics of each of the PDR probes. Comparing these clouds, we can study the role of metallicity in the chemical structure of the star forming clouds in other galaxies. In the PDR models, the locations of the H-to-H_2 and C^+-to-C-to/CO transition layers depend on heavy element abundances. We can apply the cloud-scale knowledge we obtain, to the interpretation of the central regions of the external galaxies where we can only observe the galaxy-scale emission.

1.3   Previous Work

We first observed H_2 (1,0) S(1), (2,1) S(1), and (6,4) Q(1) lines from the Orion A molecular cloud (Luhman et al. 1994). We found that the H_2 emission region is very extended, $> 1\overset{\circ}{.}5$ (or 12 pc at $d \simeq 415$ pc; Anthony-Twarog 1982), and that the far-UV photons from the central ionizing star dominate the excitation of extended H_2. Even though the BN-KL outflow source in Orion A is the archetypal shocked region, the thermally excited H_2 region is relatively compact, $< 3'$ (or 0.4 pc), and its total H_2 (1,0) S(1) luminosity is < 10 % of that of the whole PDR. Luhman & Jaffe (1996) also found a correlation between H_2 intensities and far-IR continuum intensities from star

formation regions in the Galaxy.

1.4   Organization of This Dissertation

Our group built a near-IR spectrometer (the University of Texas Near-IR Fabry-Perot Spectrometer, Luhman et al. 1995) which is optimized for extended, low surface brightness sources. In Chapter 2, I describe my work on the control system for the Fabry-Perot etalon. Additional work on a temperature-controlled cooling box for the Fabry-Perot etalon will be described in a later paper.

In Chapter 3 (Pak, Jaffe, & Keller 1996a), we report the survey of the H_2 (1,0) S(1) line emission from the inner 400 pc of the Galaxy, using the UT FPS at the McDonald Observatory 0.9 m Telescope. The total H_2 (1,0) S(1) line luminosity in the surveyed region is 8000 $L_\odot$, while the luminosity in the inner 5 pc circumnuclear gas ring is only 700 $L_\odot$. In Chapter 4 (Pak, Jaffe, & Keller 1996b), we discuss the excitation mechanism of the H_2 in the Galactic Center and NGC 253, based on the follow-up observations with the UT FPS at the CTIO 1.5 m Telescope, where we observed H_2 (1,0) S(1), (2,1) S(1), and (3,2) S(3) lines.

Even though we know the microscopic structure of PDRs in our Galaxy, we cannot necessarily apply this knowledge to the PDRs in other galaxies where the physical situations are very different. In Chapter 5 (Pak et al. 1997), we studied the chemical structure of the clouds in the Magellanic Clouds, based on our H_2 line observations using the UT FPS at the Cerro Tololo Inter-American Observatory 1.5 m Telescope, and on our CO $J = 1 \rightarrow 0$ observations at the Swedish-ESO Submillimeter Telescope. We compile data sets of H_2 (1,0) S(1), [C II], CO $J = 1 \rightarrow 0$, and far-IR emission from the star forming clouds in our Galaxy and in the Magellanic Clouds, and compare with model results from a PDR code and a radiative transfer code.

REFERENCES

Anthony-Twarog, B. J. 1982, AJ, 87, 1213

Black, J. H., & van Dishoeck, E. F. 1987, ApJ, 322, 412

Burton, M. G. 1992, Aust. J. Phys., 45, 463

Crawford, M. K., Genzel, R., Townes, C. H., & Watson, D. M. 1985, ApJ, 291, 755

Doyon, R., Joseph, R. D., & Wright, G. S. 1994, ApJ, 421, 115

Draine, B. T. 1980, ApJ, 241, 1021

Draine, B. T., & Bertoldi, F. 1996, ApJ, 468, 269

Draine, B. T., Roberge, W. G., & Dalgarno, A. 1983, ApJ, 264, 485

Fischer, J., Geballe, T. R., Smith, H. A., Simon, M., & Storey, J. W. V. 1987, ApJ, 320, 667

Genzel, R., Harris, A. I., & Stutzki, J. 1989, in Proc. of 22nd ESLAB Symposium, Infrared Spectroscopy in Astronomy, ed. B. Kaldeich (ESA SP-290), p115

Gredel, R., Dalgarno, A. 1995, ApJ, 446, 852

Hollenbach, D. J., & McKee, C. F. 1989, ApJ, 342, 306

Koornneef, J., & Israel, F. P. 1996, New Astronomy, 1, 271

Lada, C. J. 1997, in Proc. of the 170th IAU Symp., CO: Twenty-Five Years of Millimeter-Wave Spectroscopy, eds. W. B. Latter, S. J. E. Radford, P. R. Jewell, J. G. Mangum, & J. Bally (Kluwer Academic Pub.), p387

Lepp, S., & McCray, R. 1983, ApJ, 269, 560

Luhman, M.L., & Jaffe, D.T. 1996, ApJ, 463, 191

Luhman, M. L., Jaffe, D. T., Keller, L. D., & Pak, S. 1994, ApJ, 436, L185

Luhman, M. L., Jaffe, D. T., Keller, L. D., & Pak, S. 1995, PASP, 107, 184

McKee, C. F. 1989, ApJ, 345, 782

McKee, C. F. & Hollenbach, D. J. 1980, ARA&A, 18, 219

Moorwood, A. F. M., & Oliva, E. 1990, A&A, 239, 78

Moorwood, A. F. M., & Oliva, E. 1994, ApJ, 429, 602

Mouri, H. 1994, ApJ, 427, 777

Pak, S., Jaffe, D. T., & Keller, L. D. 1996a, ApJ, 457, L43

Pak, S., Jaffe, D. T., & Keller, L. D. 1996b, in the 4th ESO/CTIO Workshop, The Galactic Center, ed. R. Gredel (ASP Conf. Series Vol. 102), 28

Pak, S., Jaffe, D. T., van Dishoeck, E. F., & Johansson, L. E. B. 1997, paper in preparation

Parravano, A. 1988, A&A, 205, 71

Puxley, P. J., Hawarden, T. G., & Mountain, C. M. 1988, MNRAS, 234, 29

Sternberg, A., & Dalgarno, A. 1989, ApJ, 338, 197

Tielens, A. G. G. M., & Hollenbach, D. 1985, ApJ, 291, 722

Tiné, S., Lepp, S., Gredel, R., & Dalgarno, A. 1997, ApJ submitted

Chapter 2

Instrumentation

2.1 Why Do We Need A New Spectrometer ?

PDR models imply that H_2 emission arises on the surfaces of clouds illuminated by nearby massive young stars. The intensity of the H_2 (1,0) S(1) line is faint: $10^{-6.4} < I_{H_2} < 10^{-4.4}$ ergs s^{-1} cm^{-2} sr^{-1}, at $I_{UV} > 10$ and $n_H > 10^{2.7}$ cm^{-3} (see Figure 5.12 in this dissertation). The H_2 emission regions are very extended, however, and cover several degrees in the Orion molecular cloud complex, the Galactic Center (inner 400 pc), and the Magellanic Clouds. The study of PDRs has been done mostly with far-IR fine-structure emission lines of atoms, e.g., [O I] and [C II], and with millimeter emission lines of tracer molecules like CO.

Existing IR cameras or grating spectrometers with array detectors have high spatial resolutions down to sub-arcseconds. These instruments, however, are not optimal for faint and extended objects because the cameras cannot cover the whole emission region in a single observation and cannot provide a way to reliably subtract the air glow and thermal background emission. The principal idea of our new spectrometer is, by decreasing the spatial resolution up to arcminutes (note that this resolution is comparable to those of the existing far-IR data from the Kuiper Airborne Observatory and of the millimeter data from single-dish radio telescopes), to optimize the surface brightness sensitivity.

For the experiment described here, we use a Fabry–Perot interferometer and a single-pixel photovoltaic indium antimonide (InSb) detector ($\eta \sim 0.6$).

The following description and calculations are based on the University of Texas Fabry-Perot Spectrometer System and the 2.7 m telescope at the McDonald Observatory.

2.2 Noise

Noise, signal fluctuations of a random nature, limits the sensitivity of a spectrometer. We can separate the noise sources into three types: photon noise, intrinsic detector noise, and read noise (Kitchin 1991).

The photon noise or signal noise arises from the quantum character of the incoming signal on the detector. The arrival rate of photons fluctuates and the detected number of photons can be characterized by a Poisson distribution. The photon noise in a given integration time is the square root of the average number of detected photons in that time. The electromagnetic sources of the signal are separated into the line emission from the astronomical objects and background thermal radiation, e.g., the atmosphere of the earth, the telescope, the spectrometer, etc. At the detector, the absorbed energies per second from the object (P_{obj}) and from the background (P_{back}) are,

$$P_{obj}[\text{erg s}^{-1}] = I A \Omega \, \tau_{obj} \eta \qquad (2.1)$$

and

$$P_{back}[\text{erg s}^{-1}] = \varepsilon B_\lambda(T) \Delta\lambda \, A\Omega \, \tau_{back} \eta \, , \qquad (2.2)$$

where I is the line intensity of the source whose spectral profile is close to the $\delta(\lambda - \lambda_o)$ function, ε is the emissivity of the background radiation source, $B_\lambda(T)$ is the Planck function, $\Delta\lambda$ is the bandwidth accepted by the cryogenic part or spectrometric part of the system, A is the collecting area of the primary mirror, Ω is the solid angle field of view of the telescope (assuming $\Omega_{source} \gg \Omega$), τ is the transmission of the optical components in the telescope and the

spectrometer, and η is the quantum efficiency of the detector. The value of area-solid angle product $(A\Omega)$ is conserved at the primary mirror of the telescope, at the spectrometer, and at the detector. For a typical intensity of the H_2 emission $(P_{obj} \approx 10^{-9}$ erg s$^{-1})$ and for that of background $(P_{back} \approx 10^{-7}$ erg s$^{-1})$, the dominant signal source is the background radiation, so that we call the photon noise *background noise*. The background noise in number of electrons (η times number of photons)

$$N_{back} = \left[\frac{\lambda}{hc} P_{back}\, t \right]^{\frac{1}{2}}, \tag{2.3}$$

where t is the integration time.

The intrinsic noise originates inside the detector, and the photovoltaic detector has Johnson noise and dark-current shot noise. The *Johnson noise* or thermal noise is generated from the thermal motion of charge carriers in a resistor and depends only on the temperature $(T \sim 50\mathrm{K})$ and the resistance $(R \sim 10^{12}$ $\Omega)$ of the detector itself,

$$N_{Johnson} = \frac{1}{e} \left[\frac{4kT}{R} t \right]^{\frac{1}{2}}, \tag{2.4}$$

where e is the charge of an electron $(1.6 \times 10^{-19}$ C$)$. The random arrival rate of carriers at the $p-n$ junction in the detector generates the *dark current shot noise* which is a function of the internal dark current (I_{dark}),

$$N_{dark} = \left[\frac{2I_{dark}}{e} t \right]^{\frac{1}{2}}. \tag{2.5}$$

The *read noise* (N_{read}) arises from converting the generated charge at the detector into a readable form of voltage and amplifying that voltage. The detector itself has a capacitance and integrates the generated charge during one exposure time $(0.1 - 2$ sec$)$. An integrating preamplifier converts the charge to voltage and amplifies the voltage, and an analog–digital (A/D) converter reads a series of sample voltages at a rate of 10 KHz (B) which is limited by the

A/D bandwidth. We coded a routine to get the best slope of the integrated sample values with the least squares method (Chapman et al. 1990). The value of the slope corresponds to the detected signal. If we assume that read noise dominates over the other noise sources, we can calculate the read noise by multiplying the statistical slope error by the integration time,

$$N_{read} = N_{sample} \left[\frac{12}{B\,t} \right]^{\frac{1}{2}} ,$$ (2.6)

where N_{sample} is the error (root mean square) of each sample.

The total noise is,

$$N_{total}^2 = N_{back}^2 + N_{dark}^2 + N_{Johnson}^2 + N_{read}^2 .$$ (2.7)

For short integration times the read noise ($\propto t^{-\frac{1}{2}}$) is dominant and for long integration times the background noise, dark current noise, and Johnson noise ($\propto t^{\frac{1}{2}}$) become increasingly important. Assuming that the noise is a function of the integration time, $N(t)$, we can find the optimum integration time (t_{op}), at which the total noise is minimum, by equating the read noise function (Equation 2.6) and the other noise functions (Equations 2.3, 2.4, and 2.5),

$$N_{read}^2 = N_{back}^2 + N_{dark}^2 + N_{Johnson}^2 .$$ (2.8)

From the signal value in number of electrons,

$$S = \frac{\lambda}{hc}\,P_{obj}\,t ,$$ (2.9)

the signal to noise ratio (S/N) can be expressed as a function of the integration time, $S/N \propto t^{\alpha}$. The power of t, α, is 3/2 at $t < t_{op}$ and 1/2 at $t > t_{op}$. In section 2.4, we present calculated values of each noise source.

2.3 Fabry-Perot Interferometer

We use a large surface area detector and a short focal length coupling lens, whose value of $A\Omega$ is large enough to detect low surface brightness, extended

sources. A *grating spectrometer*, however, cannot deliver for large $A\Omega$ and small $\Delta\lambda$, because both of the values are proportional to the width of the slit (W), i.e.,

$$A\Omega = \frac{\pi}{4}Wh\left(\frac{D}{f}\right)^2 , \ \Delta\lambda \simeq \lambda\frac{W}{d}\left(\frac{D}{f}\right) , \quad (2.10)$$

where h is the height of the slit, d is the width of the grating, and D and f are the diameter and focal length of the telescope. For typical parameters of the grating and telescope, the spectral resolving power ($\lambda/\Delta\lambda$) of 2000 corresponds to a several arc second beam size. With a Fabry-Perot interferometer or etalon (FP) we can increase the beam size, Ω, to square arcminutes, even though large $A\Omega$ slightly reduces the spectral resolving power. The main disadvantage of the FP in observation is that we cannot get all channels in the line profile in one integration, but we have to scan across the line, increasing the total observation time.

The FP consists of two flat semi-transparent, parallel mirrors separated by some distance (l). Light incident on the mirror surface will undergo multiple reflections between the mirrors. The different reflections interfere, resulting in a narrow bandwidth being transmitted and most of the radiation being reflected by the FP. When we fix the distance between the two mirrors, a series of wavelengths is transmitted in different orders of interference. The wavenumber (in units of cm^{-1}) difference between adjacent transmission maxima is called the free spectral range (FSR),

$$\Delta\left[\frac{1}{\lambda}\right]_{FSR} = \frac{1}{2l} . \quad (2.11)$$

The finesse (F), to which the resolvable spectral bandwidth is inversely proportional, is the effective number of interfering beams and the most important performance parameter of the FP. Mirror reflectivity (F_{ref}), parallelism and planeness of the mirrors (F_{pp}), and the range of the incident angles (F_{ang})

contribute to individual finesse,

$$F_{ref} = \frac{\pi\sqrt{R}}{1-R}\,, \tag{2.12}$$

$$F_{pp} = \frac{\lambda}{2\,\Delta s}\,, \tag{2.13}$$

and

$$F_{ang} = \frac{\lambda}{l(\Delta\theta)^2}\,, \tag{2.14}$$

where R is the mirror reflectance, Δs is the deviation from parallelism and planeness, and $\Delta\theta$ is the range of the incident angle to the FP plate ($A\Omega = A_{FPplate}\pi(\Delta\theta)^2_{max}$). The net finesse can be estimated as,

$$F_{net}^{-2} \simeq F_{ref}^{-2} + F_{pp}^{-2} + F_{ang}^{-2}\,. \tag{2.15}$$

When we assume that only F_{ref} is effective, the formula of the instrument spectral profile is

$$I(\lambda, l, \theta) = \left(1 - \frac{\alpha}{1-R}\right)^2 \left[1 + \frac{4R}{(1-R)^2}\sin^2\left(\frac{2\pi l\cos\theta}{\lambda}\right)\right]^{-1} \tag{2.16}$$

where α is the absorbed or scattered energy fraction on coated surfaces, and θ is incident angle (Born and Wolf 1965; Moore, David, and Coplan 1988). In Figure 2.1 we plot several profiles for various R with a point source ($\theta = 0$) and $\alpha = 0.004$. A convolution of this instrument profile and an object emission profile will make an observed spectral line profile.

2.4   University of Texas Fabry-Perot Spectrometer

The University of Texas Fabry-Perot Spectrometer (UT FPS) is designed to maximize $A\Omega$ up to 4.5×10^{-3} cm^2 sr and minimize noise. The optical layout is shown in Figure 2.2. Inside the fore-optics box, the focused beam from the telescope is collimated and guided to an H-band or K-band Fabry-Perot interferometer. The beam passes through a CaF$_2$ window into a ~ 55 K (solid

nitrogen temperature) dewar. The $0.5 - 1\%$ fixed interference filter next to the window selects a single order from the Fabry-Perot interferometer. Finally the beam is focused by a doublet camera lens of $fl = 20$ mm, and illuminates a 1 mm diameter InSb detector (COBE series, Cincinnati Inc.).

The generated electrons on the detector are integrated by a low noise integrating amplifier (JF-4 model, Infrared Laboratories Inc.). The JF-4 consists of a hybrid circuit containing a balanced junction field-effect transistor (JFET) with a voltage gain of $0.8 - 0.9$, and an input capacitance of 7.5 pF. The JFET needs an external reset pulse to remove the collected charge from the integrating gate before the exposure. A pre-amplifier (RS-1 model, Infrared Laboratories Inc.) amplifies the voltage signal from the JF-4 with gain of 100 and the PC based A/D converter (LSDAS-16, Analogic Co.) reads the final signal.

We use two Burleigh Inc. TL-38 Tunable Etalons in our spectrometer system: one for K-band and the other for H-hand. In the etalon, two reflecting etalon plates are separated by $l \simeq 100$ μm and the reflectance (R) of each plate surface is about 91 %. The etalon plates are permanently mounted in two holders. The rear mirror holder is mechanically tilted by adjusting two spring loaded mounting screws. The front mirror holder is attached to a tunable etalon drive ring and three piezoelectric transducers (PZTs) support the drive ring. The PZT is a kind of actuator and an electrically controllable positioning element whose length varies in proportion to the high DC voltage supplied ($\sim$ 6 μm per 1000 V). Controlling the three PZTs independently aligns the front plate with respect to the rear plate, and driving all three PZTs synchronously changes the plate spacing (l) parallel to the optical axis. To manipulate the etalon plates, three alignment voltages (0–500 V) are applied to the negative poles of the PZTs individually and one scan voltage ($0 - 1000$ V for the K-band etalon and $0 - 1200$ V for the H-band etalon) is applied to the positive poles

simultaneously (Figure 2.3). We can integrate the signal at a fixed scanning voltage and make a spectral profile by increasing or decreasing the scanning voltage step by step. Because of the crystal characteristics of PZTs, the positive field on each PZT should not exceed the maximum operating voltages (1000 V for the K-band etalon and 1200 V for the H-band etalon) or the reverse field should not exceed the half of the maximum operating voltages.

2.5 Shortcomings of the Fabry-Perot

As we expressed in Equations 2.13 and 2.15, the misalignment of the etalon plates in the FP decreases the net finesse (F_{net}) and reduces the spectral resolving power. For the K-band etalon (the following descriptions are only for the K-band etalon), to keep the value of the net finesse over 90% of the reflectivity finesse (e.g., $F_{net} \simeq 39$, $F_{ref} \simeq 43$, and neglecting F_{ang}), the parallelism (alignment) and planeness finesse (F_{pp}) should be over 96, which requires that the deviation from the aligned status be less than 0.011 μm. The corresponding tolerance in aligning voltage is 1.8 V.

A conventional method for alignment is illuminating the FP with a expanded and collimated 653 μm He-Ne laser and looking at the projected interference pattern on a distant screen. For this method we used a commercial control box (Model RC-43, Burleigh Inc.) which has a ramp generating circuit and one amplifying circuit to support three scanning PZTs, and has three power outputs which are adjusted by individual potentiometers to control the alignment. With sequential scanning ramp mode and the reference source, we can see moving interference fringes on the screen. If the two mirrors are aligned well, the fringe pattern becomes a single bright or dark spot. Watching the fringe pattern and with trial and error, we can adjust one of three aligning potentiometers and find the best voltages of the corresponding PZTs in turn.

Surfaces on the reflecting mirrors in our FP, however, are specially

coated for infrared light only. The reflectivity or finesse at visible wavelengths is not sufficient for alignment by eye, and we cannot expect a precise alignment with this method. Another shortcoming of the FP is that the PZTs are not electrically stable and misalign the etalon in ~ 10 minutes. It is very inefficient to align with the conventional method while observing. Thus, we automated the alignment procedure with a closed loop computer controlled method.

2.6 High Voltage Amplifier

To manipulate the PZTs, we built a new high voltage DC amplifier, because the RC–43 is inadequate for the automated alignment system. The new amplifier is used between the PZTs and D/A interface board in the computer. Since our D/A board has four 0 to 10 volt output channels, the HV amplifier needs three independent aligning channels with 50 gain and one scanning channel with 100 gain.

Our HV amplifier box has one regulated high voltage supply (Model 602C-15P, Bertan Associates, Inc.) and four independent noninverting feedback amplifier circuits, each of which contains an identical op–amp (Figure 2.3). To make the high voltage output, we put a power transistor between the op–amp and the output channel using the idea of *current sources* (Horowitz and Hill 1989). The gain of each circuit is determined by R_1 and R_2 ($G = 1 + R_2/R_1$). We chose metal film resistors, because they are very accurate and stable with changes in outside temperature.

Another important thing in designing the circuit is the amount of the output power at each channel, because each PZT has capacitance of 2 nano Farad [nF]. We can simplify the amplifier circuit and the connected PZT with Thévenin's theorem. When a supplied voltage to a PZT is changed (from V_i to V_f), it takes some time for a voltage of the PZT (V) to reach the desired

voltage,

$$V = V_f + (V_i - V_f) \exp\left(-\frac{t}{ZC}\right) , \qquad (2.17)$$

where $Z = R_3 V_f / 1200$, and R_3 is the load resistor. By decreasing R_3, we can decrease the response time and increase the output power. Using low resistance load resistors, however, produces another difficulty in finding stable high power resistors. With these restrictions we need to decide on the appropriate output power. The scanning channel supports three parallel PZTs (3×2 nF) and the response time should be less than 5 msec (the interval between resetting the JFET and integrating) to satisfy our requirements for system speed. Each aligning channel supports only one PZT and the voltage changes do not happen frequently. A certain amount of response time ($\sim$ 10 msec) is allowed in this case. Each aligning channel has 0.1 W output power and the scanning channel has 1 W.

2.7   Automatic Alignment Program

Part of the FP spectrometer system control program is an automatic alignment routine which can be called frequently and performed quickly. Since the behavior of the PZT is very sensitive to outside conditions and is unpredictable, the simplest procedure (i.e., a *trial and error* method) is safe and convenient. We use a Helium 2.112μm line in a He-Ne laser as a spectral reference source. The program monitors the FP alignment by checking the spectral profile of the reference source. If the FP etalon plates are not seriously out of alignment, the observed flux of a reference line is almost constant and independent of the alignment. As the two plates become parallel, the full width at half maximum (FWHM) of the observed profile decreases and the peak signal value (P_i) increases. We use the peak signal to monitor the alignment.

Figure 2.4 shows the flow chart of the automatic alignment program. At first, the program scans the reference spectral line by changing the voltage

of the scanning PZTs (V_{scan}). From the scanned data, a peak signal value of the line is stored in a buffer. Next, one of three aligning PZT voltages (V_{align1}) is adjusted while fixing the other two voltages (V_{align2} and V_{align3}), and the reference line is scanned again. The amount of adjusting voltage (ΔV) is the same as the aligning voltage tolerance (1.8 V) which we deduced in section 2.5. If the new peak value is larger than the previous one, the program adjusts the aligning voltage and scans again. This is repeated until the FP is aligned. With this routine, the other two aligning voltages can be adjusted in turn. It takes less than 30 seconds to align with this program. We call this alignment routine every $5 - 10$ minutes during observations.

Table 2.1
Individual Noise

CONTRIBUTOR	T[K]	$\Delta\lambda[\mu\mathrm{m}]$	ε	N[e]
window	273	2.44×10^{-2}	0.10	$254\ t^{\frac{1}{2}}$
Fabry-Perot	278	2.44×10^{-2}	0.10	$350\ t^{\frac{1}{2}}$
fore-optics box	278	8.05×10^{-4}	0.10	$150\ t^{\frac{1}{2}}$
telescope	278	8.05×10^{-4}	0.15	$106\ t^{\frac{1}{2}}$
atmosphere	278	8.05×10^{-4}	0.40	$69\ t^{\frac{1}{2}}$
Total Background[a]	278			$419\ t^{\frac{1}{2}}$
Dark Current	50			$650\ t^{\frac{1}{2}}$
Johnson Noise[b]	50			$329\ t^{\frac{1}{2}}$
Read Noise				$300\ t^{-\frac{1}{2}}$

[a] We use Equations 2.2 and 2.3 with $\lambda_\circ = 2.122\ \mu$m, $A\Omega = 3.02 \times 10^{-3}$ cm^2 st, and $\eta = 0.6$.

[b] We use Equation 2.4 with $R = 10^{12}\Omega$.
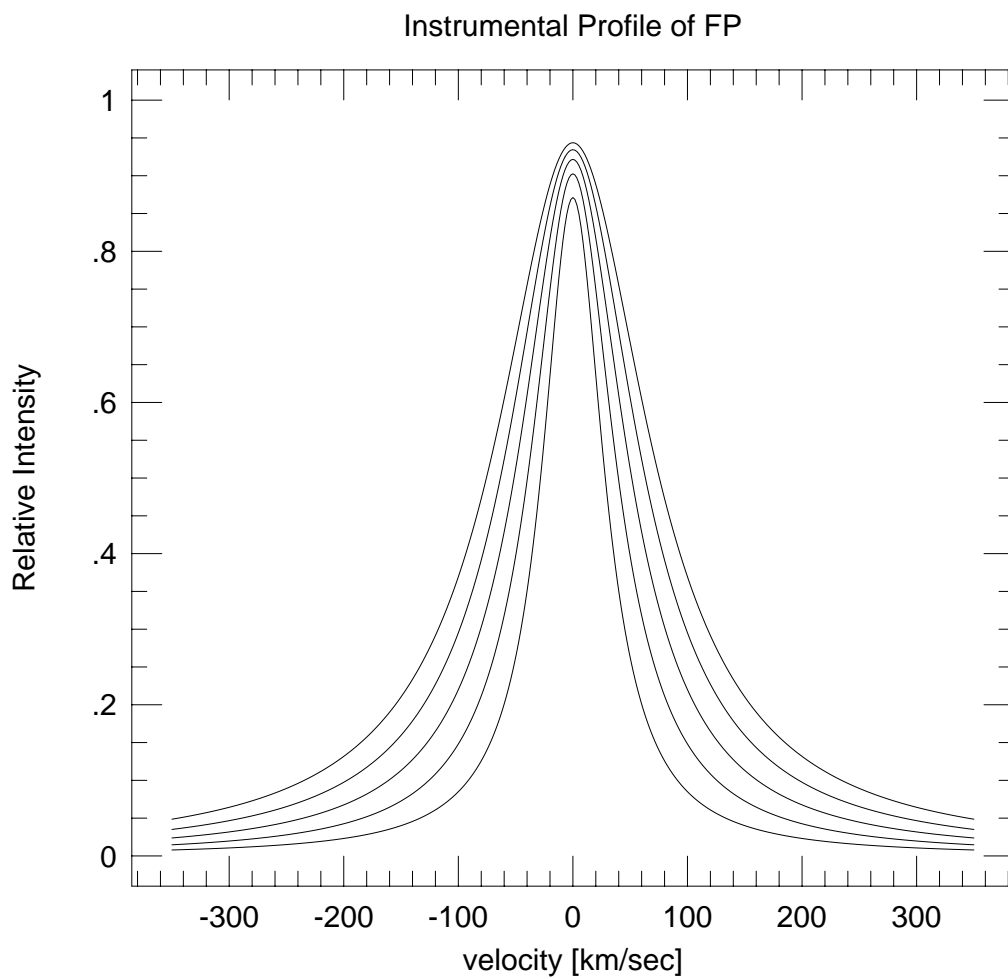
Figure 2.1.— Instrumental Profile of Fabry-Perot Spectrometer in velocity units with various reflectivities (R). From the broadest profile to the narrowest profile, R's are 0.86 ($F_{ref} = 20.8$), 0.88 (24.6), 0.90 (29.8), 0.92 (37.7), and 0.94 (50.8). We assume that the source is point ($\theta = 0$) and $\alpha = 0.004$. The free spectral range (FSR) is 3,333 kms^{-1}.

To Telescope Secondary

Sliding
Mirror

Spectral Calibration/Fabry-Perot
Alignment Source(s)

To Vacuum Pump

Collimator
Lens

LN2   LN2

Fabry-Perot
Etalon

Solid N2

Field Optics,
InSb Detector,
and JFET

Cold
Stop

Filter
Wheel

Pre-amp

High Voltage
Supply and FP
Electronics

D/A
Converters

A/D
Converter

Data
Storage

Microcomputer

Figure 2.2.— A schematic diagram of the optical system of Texas Fabry-Perot Spectrometer.

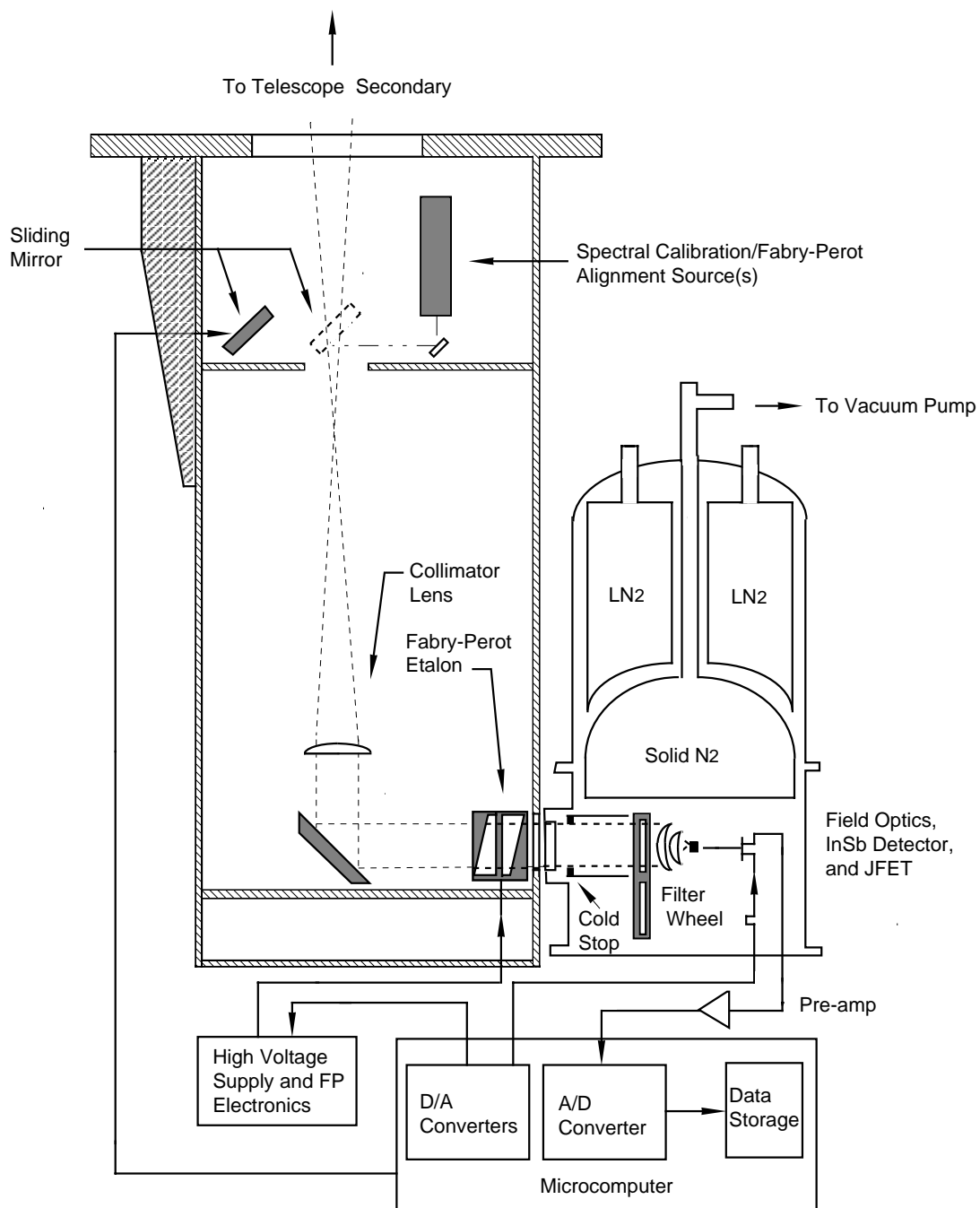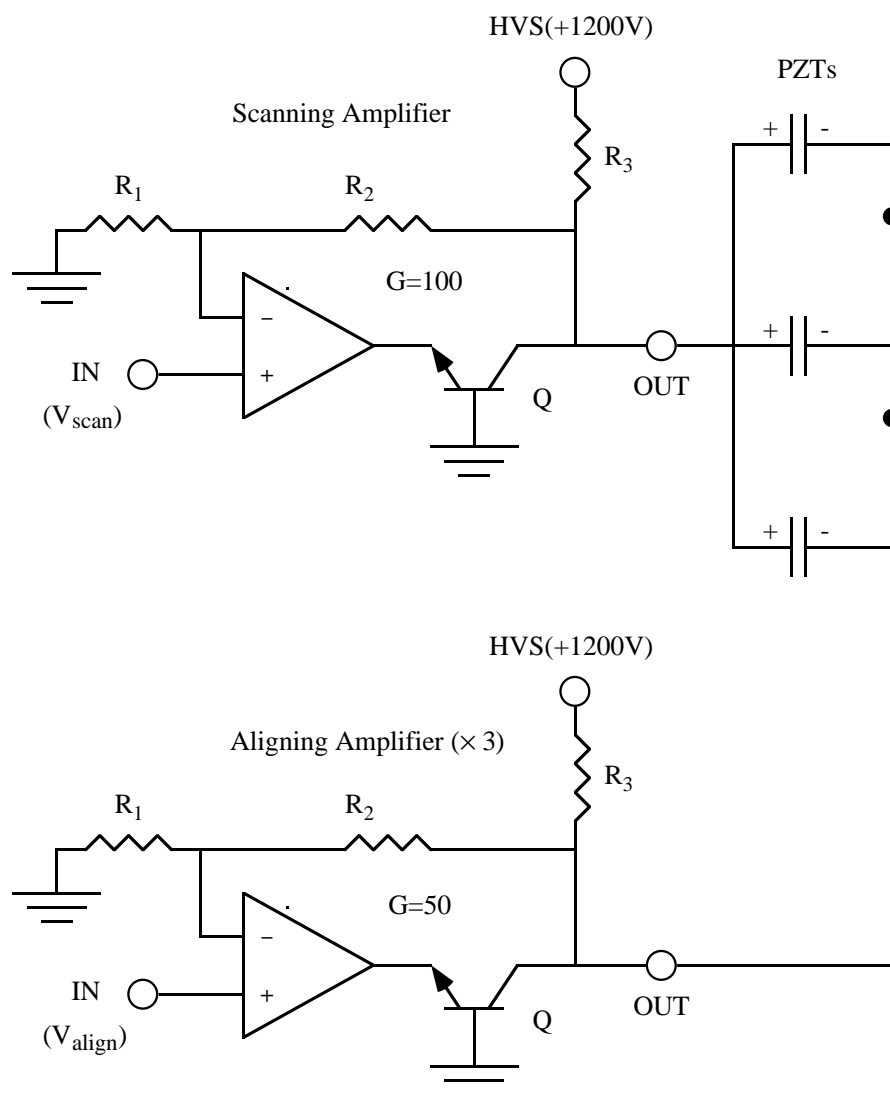Figure 2.3.— Simplified noninverting feedback op-amplifier circuit diagram for the scanning amplifier and one of the aligning amplifiers. The gain (G) is determined by $G = 1 + R_2/R_1$. One regulated high voltage supply (HVS) supports all of the four circuits and each R_3 divides the output power.
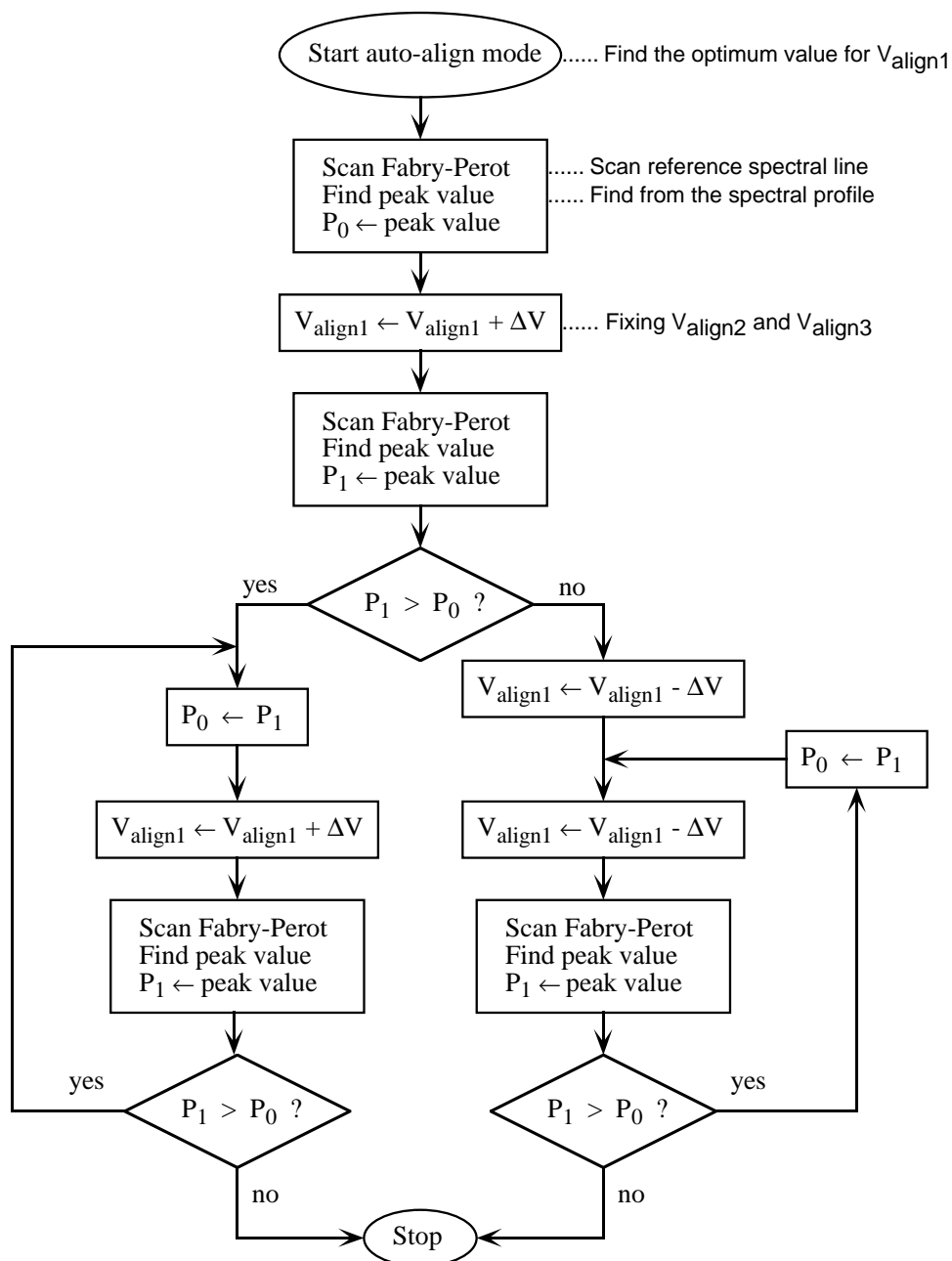
Figure 2.4.— The algorithm of the automatic alignment program. A trial and error approach is used to find the best V_{align1}. The program monitors the aligned status by checking the peak signal value (P_i) of the observed reference spectral profile. Running this routine for V_{align2} and V_{align3} in turn, the FP spectrometer system can maintain optimum alignment.

REFERENCES

Born, M., and Wolf, E. 1965, Principles of Optics (Oxford: Pergamon Press)

Chapman, R., Beard, S. M., Mountain, C. M., Pettie, D. G., & Pickup, D. A. 1990, in Instrumentation in Astronomy VII, ed. D. L. Crawford (Washington: SPIE), p.34

Kitchin, C. R. 1991, Astrophysical Techniques (New York: Adam Hilger) p.38

Moore, J., Davis, C., and Coplan, M. 1988, Building Scientific Apparatus (USA: Addison Wesley), p.242

Chapter 3

H$_2$ (1,0) S(1) Emission from the Inner 400 pc of the Galaxy

ABSTRACT

We have mapped the H$_2$ (1,0) S(1) ($\lambda = 2.1215\,\mu$m) emission line along a 400 pc long strip and in a 50 pc region in the Galactic center. There is H$_2$ emission throughout the surveyed region. The typical de-reddened (A$_K$ = 2.5 mag) H$_2$ (1,0) S(1) surface brightness, $\sim 3 \times 10^{-5}$ ergs s^{-1} cm^{-2} sr^{-1}, is similar to the surface brightness in large-scale photon-dominated regions in the galactic disk. We investigate two possible excitation mechanisms for the H$_2$ emission: UV-excitation by photons from OB stars, and shock waves, and conclude that UV-excitation is more likely. The total H$_2$ (1,0) S(1) luminosity in the inner 400 pc region of the Galaxy is 8000 $L_\odot$. The ratio of the H$_2$ to far-IR luminosity in the inner 400 pc of the Galaxy agrees with that in starburst galaxies and ultraluminous infrared bright galaxies.

3.1   Introduction

Physical conditions in the interstellar medium of the Galactic center[1] are significantly different from those in the solar neighborhood. The thin disk of interstellar material in the Galactic center (size: 450×40 pc) contains $\sim 10^8\ M_\odot$

---

[1] We use here the term "Galactic center" to denote the inner several 100 pc region of our Galaxy. We adopt a distance of 8.5 kpc, with which 1° corresponds to 148 pc.

of dense molecular gas, ~ 10 % of the Galaxy's molecular mass (Güsten 1989). The molecular clouds in the Galactic center have higher density, metallicity, and internal velocity dispersion than the clouds in the solar neighborhood (Blitz et al. 1993). Strong radio continuum radiation from giant H II regions and extended, low-density (ELD) H II (Sofue 1985), as well as far-IR radiation from dust (Odenwald & Fazio 1984), indicate that the UV radiation field is intense. The energetic conditions in the Galactic center can provide a unique view of the interaction between stellar UV radiation and molecular clouds, and a nearby example for the nuclei of other galaxies.

Because H_2 is so light, its excited rotational states are too high ($\Delta E/k > 500$ K) to be thermally excited in cold clouds ($T_{kin} < 50$ K). Ro-vibrational lines of H_2 trace Photon-dominated Regions (PDRs) where far-UV photons excite the H_2 and shocked regions where the H_2 is thermally excited. As a result, the central regions (~ 1 kpc) in starburst galaxies are powerful emitters of near-IR H_2 emission (Puxley, Hawarden, & Mountain 1989; Joseph 1989; Lester et al. 1990; Moorwood & Oliva 1990). Vigorous star formation in these galaxies produces large numbers of UV photons which can excite H_2, while subsequent supernovae can shock excite the H_2.

Gatley et al. (1984, 1986) and Gatley & Merrill (1993) have observed H_2 emission from the inner 5 pc diameter (or $2'$) in the Galactic Center, a much smaller region than those observed in starburst galaxies. With the University of Texas Near-Infrared Fabry-Perot Spectrometer (Luhman et al. 1995), it is now possible to observe H_2 emission over much larger angular scales. We describe here a program to map the Galactic center in H_2 emission on a scale of several degrees (several hundred pc), and discuss the likely H_2 excitation mechanism. We can then compare the central region of our Galaxy with those in other galaxies.

3.2 Observations

We observed the H_2 (1,0) S(1) ($\lambda = 2.1215$ μm) line at the McDonald Obser-
vatory 0.91 m telescope in 1994 May and June, using the University of Texas
Near-Infrared Fabry-Perot Spectrometer (Luhman et al. 1995). To select a
single order from the Fabry-Perot interferometer, we used a 1 % interference
filter cooled to 77 K. The telescope (f-ratio 13.5), a collimator (effective focal
length 343 mm), and a field lens (effective focal length 20 mm) combined to
produce a beam diameter of $3''.3$ (equivalent disk). At a distance of 8.5 kpc,
this corresponds to 8.2 pc.

The Fabry-Perot interferometer operated in 92nd order with an effective
finesse of 17.7, yielding a spectral resolution (FWHM) of 184 km s^{-1}. The scan-
ning spectral range was ± 335 km s^{-1} centered at $V_{LSR} = 0$, with 20 sequentially
exposed channels. We aligned the Fabry-Perot etalon every $5-8$ minutes by ex-
ecuting our automatic alignment routine (Chapter 2 in this dissertation). The
Fabry-Perot etalon plates maintained alignment for $15-30$ minutes, but the
plate separation drifted by the equivalent $2-5$ km s^{-1} (wavelength scale) per
minute. Using the telluric OH (9, 7) $R_1(1)$ 2.12440 μm line (Oliva and Origlia
1992) which was available in each raw spectrum, we calibrated the wavelength
scale to ± 20 km s^{-1}.

We nodded the telescope between the object and the sky every ~ 60
seconds to subtract background and the telluric OH line emission. The sky
positions were offset by $\pm 1°$ in declination ($\Delta l = \pm 0°.85$, $\Delta b = \pm 0°.53$) from
the object positions. The telescope pointing error was $\pm 15''$. We made a
strip map along the Galactic plane running across Sgr A*, at $b = -0°.05$, from
$l = -1°.2$ (178 pc) to $+1°.6$ (237 pc), taking spectra at $0°.1$ or $0°.2$ intervals
(Figure 3.1). We also mapped the central 50 pc region including Sgr A and
the radio "Arc" (the arched filaments and the vertical filaments, Yusef-Zadeh,
Morris, & Chance 1984) on a $0°.05$ grid (see Figure 3.2). The relative flux

calibration is accurate to ± 15 %.

3.3 Results

There is H_2 emission throughout the 400 pc diameter region around the Galactic Center. About 70 % of the observed positions along the strip at $b = -0°.05$ have detections of the H_2 (1,0) S(1) line with a significance of 3σ or more. Figure 3.1 shows the intensity distribution of H_2 (1,0) S(1) along the strip. The H_2 intensity peaks strongly at Sgr A and decreases continuously from $l = -0°.1$ to $-0°.7$. The "dust ridge" seen in 800 μm continuum emission (Lis & Carlstrom 1994) may cause the dip between $l = +0°.1$ to $+0°.3$. Away from the nucleus, the intensity distribution is fairly flat. The average H_2 intensity of the positive longitudes is only a factor of 2 higher than that of the negative longitudes, while observations of [C I] $^3P_1 \rightarrow ^3P_0$, ^{13}CO $J = 1 \rightarrow 0$ (Plume 1995), and radio continuum (Mezger & Pauls 1979) show significantly more emission at the positive longitudes.

Figure 3.2 shows the H_2 (1,0) S(1) intensity distribution in the inner 50 pc of the Galaxy overlayed on a simplified radio continuum map (based on Yusef-Zadeh, Morris, & Chance 1984). We have detected H_2 emission in the arched filaments and in the Sickle at levels comparable to those of the H_2 emission elsewhere along the Plane. The inset in Figure 3.2 shows the strong H_2 (1,0) S(1) distribution in the $0°.022 \times 0°.038$ region around Sgr A West mapped by Gatley et al. (1986). In Gatley's work, the H_2 appears to be brightest along the inner edge of the circum-nuclear gas ring at radius of $1.0-2.5$ pc. Our measured flux at ($l = -0°.05$, $b = -0°.05$), 1.5×10^{-11} ergs s^{-1} cm^{-2}, agrees within the errors with the total flux from the map of Gatley et al. (1986, $F = 2.0 \times 10^{-11}$ ergs s^{-1} cm^{-2}). The H_2 emission observed adjacent to ($l = -0°.05$, $b = -0°.05$) most likely arises from portions of the circum-nuclear ring beyond their map.

3.4   Discussion

3.4.1   Extinction Correction

At 2.2 μm, the emission from the Galactic center is attenuated by interstellar material in the foreground ("foreground extinction", mostly 4-8 kpc from the Galactic Center) and by material in the Galactic center itself ("Galactic center extinction"). Catchpole et al. (1990) mapped the extinction toward the Galactic center by observing the near-IR reddening of giant stars in the central few hundred parsecs. Along our H_2 strip at b $= -0°.05$ (for $-0°.6 < l < +0°.6$), the extinction is fairly uniform with a value $A_K \simeq 2.5$ mag. Although most of this extinction is in the foreground, some of it could occur within the Galactic center since Catchpole et al. (1990) were able to identify patches in their maps with $A_K > 2.5$ mag with known molecular clouds in the Galactic center (see plate 4 in Glass et al. 1987). Based on this work, we adopt $A_K = 2.5$ mag ($A_V \simeq 30$ mag) for the foreground extinction.

The Galactic center extinction, at least in certain directions, greatly exceeds the foreground extinction. Typical ^{12}CO $J = 1 \rightarrow 0$ line strengths along the strip we have surveyed in H_2 are 1500 K km s^{-1} (Oort 1977). This line strength implies an A_K of $10 - 40$ mag, depending on the CO/H_2 and A_K/H_2 ratios in the Galactic center (Sodroski et al. 1994). The extinction through individual clouds may also be substantial ($A_K \simeq 10 - 30$ mag for a 10 pc long cloud with $n(H_2) = 10^4$ cm^{-3}). The relevance of the Galactic center extinction depends on the source of the H_2 emission. Any H_2 emission originating within the clouds will be highly extincted. If the H_2 emission arises on the cloud surfaces, however, we only miss the H_2 flux from the back side of each cloud.

Clouds lying in front of other clouds will further reduce the flux reaching us from the front surfaces. If, in the Galactic Center, the velocity integrated area filling factor of clouds, f, is substantially greater than unity, extinction by overlapping clouds will reduce the H_2 flux observed from the front surfaces

by a factor of $\sim 1/f$ in addition to the foreground extinction and to the loss of emission on the opposite sides of the clouds. Typical clouds in the Galactic center disk have kinetic temperatures ~ 70 K and linewidths ~ 20 $\mathrm{km\,s^{-1}}$ (Güsten 1989). An ensemble of such clouds could produce the observed ^{12}CO J=1$\rightarrow$0 lines in the Galactic center with $f \simeq 1$. We therefore conclude that the extinction of any H$_2$ emission from cloud surfaces facing the sun beyond the foreground extinction of A$_K$= 2.5 mag discussed above is not substantial. Since the extinction of emission from within the clouds or from the sides facing away from us is difficult to estimate and since no correction is usually made for such effects in giant molecular clouds and galactic nuclei, we make no additional extinction corrections here.

3.4.2 UV Excitation of H$_2$

If one ignores the region immediately around Sgr A*, the de-reddened (A$_K$ = 2.5 mag, see Section 3.4.1) H$_2$ (1,0) S(1) surface brightness along the Galactic plane has a roughly constant value of $\simeq 3 \times 10^{-5}$ $\mathrm{ergs\,s^{-1}\,cm^{-2}\,sr^{-1}}$. Any excitation mechanism for the H$_2$ must be able to explain both the absolute intensity and the uniformity and extent of the emission. The excitation of the H$_2$ $v = 1$, $J = 3$ state can result either from radiative decay from UV-excited electronic states or from energetic collisions. H$_2$ can absorb 91–111 nm photons in the $B^1\Sigma_u^+ - X^1\Sigma_g^+$ Lyman and $C^1\Pi_u - X^1\Sigma_g^+$ Werner bands. About 90% of the time, the excited H$_2$ decays to some ro-vibrational level of the ground electronic state. The relative line intensities arising in UV-excited H$_2$ are insensitive to density or to UV field strength if $n(\mathrm{H}_2) < 10^4$ cm^{-3} (Black and van Dishoeck 1987). At densities $\geq 10^5$ cm^{-3}, UV-excited gas can become hot enough that collisions populate states with $v = 1$ (Sternberg and Dalgarno 1989). Collisional excitation can also result from shocks which abruptly heat the gas to $> 10^3$ K (e.g. Hollenbach, Chernoff, & McKee 1989). Several observational results lead us to believe that UV excitation is responsible for

the (1,0) S(1) emission in the Galactic Center.

The denser parts of clouds like Orion and NGC 2024 produce H_2 emission with an intensity close to that observed in the Galactic Center. In Orion and NGC 2024, the degree-scale H_2 emission has a typical surface brightness $\sim 6 \times 10^{-6}$ $\mathrm{ergs\,s^{-1}\,cm^{-2}\,sr^{-1}}$ (Luhman et al. 1994). Along the molecular ridges in these clouds, the H_2 surface brightness is 3-5 times higher. Observations of H_2 transitions arising from higher-lying states indicates that, in these sources, the (1,0) S(1) emission is a result of UV fluorescence. In Orion, the UV-excited emission accounts for at least 90% of the total flux in the (1,0) S(1) line (Luhman et al. 1994).

If large-scale H_2 emission arises in the surface layers of the clouds where UV photons can excite the molecules, the dust, which absorbs the bulk of the incident flux, ought to radiate in the far-IR continuum as well. Luhman & Jaffe (1996) have compared the H_2 (1,0) S(1) observations of clouds in the galactic disk with IRAS far-IR continuum results and derived a relation between the H_2 (1,0) S(1) line and far-IR continuum intensities. We can use this relationship and the measured far-IR intensities in the Galactic center to see if UV-excitation is plausible for our observed (1,0) S(1) emission. In most of the region along our Galactic center H_2 cut, the IRAS 100 μm band detectors were saturated. In order to compare the Galactic center H_2 data to far-IR continuum measurements with comparable angular resolution, we have combined the un-saturated IRAS measurements from the outer ends of our H_2 strip with the 40–250 μm continuum measurements of Odenwald and Fazio (1984). To make the two data sets comparable, we have first converted the IRAS 60 μm and 100 μm fluxes into a total far-IR flux (the FIR parameter of Fullmer and Lonsdale 1989). The IRAS total far-IR flux agrees well with the far-IR flux derived by Odenwald and Fazio in the regions where their data and the unsaturated IRAS data overlap. We then converted the combined datasets into integrated far-IR

intensity for comparison with our H_2 strip. We used the Luhman & Jaffe (1996) galactic disk H_2 dataset to re-derive their H_2/far-IR relation in intensity units. We obtain,

$$\log(I_{H_2 v=1-0S(1)}) = -4.65 + 0.39 \log(I_{FIR}),$$

where both intensities are in $ergs\, s^{-1}\, cm^{-2}\, sr^{-1}$. The dispersion of the galactic disk cloud H_2 intensities about this relation is $\log(\sigma) = 0.23$. If we de-redden the Galactic center H_2 observations by $A_K = 2.5$ mag (*but otherwise do nothing to fit the data to the galactic disk relation*), the Galactic center H_2 intensities have a dispersion $\log(\sigma) = 0.26$ about this relation. The Galactic center results are therefore completely consistent with the empirical far-IR vs. H_2 relationship derived for the UV-excited surfaces of clouds in the galactic disk.

We can also compare the H_2 line intensities predicted by models of photon-dominated regions to the observed intensities. The models use indirect observations of the far-UV field in the Galactic center (radio and far-IR continuum fluxes) as inputs. For the radio, we predict the far-UV field using emission from extended, low-density (ELD) H II regions because the molecular cloud column densities, and therefore the extinction at the wavelength of H_2, tend to be high (and uncertain) toward the discrete H II regions. Away from discrete H II regions, the typical 10.5 GHz flux density is 2.2 Jy in a $3\overset{''}{.}3$ beam (Sofue 1985). Assuming $T_e = 10^4$ K, this flux density corresponds to 2.3×10^{49} Lyman continuum photons per second (Mezger, Smith, & Churchwell 1974), in the corresponding region (8.2 pc). For an ionizing source with an effective stellar temperature, $T_{eff} = 3.5 \times 10^4$ K as the UV source, the 2.3×10^{49} Lyman continuum photons imply $\sim 2.3 \times 10^{49}$ photons in the range which can excite the H_2 (91-123 nm), or a luminosity of 1.2×10^5 $L_\odot$ (Black & van Dishoeck 1987). From our observations, the average H_2 flux in a $3\overset{''}{.}3$ beam is 2.4×10^{-12} $ergs\, s^{-1}\, cm^{-2}$. The corresponding total infrared H_2 luminosity in the 8.2 pc ($3\overset{''}{.}3$) region is 3.3×10^3 $L_\odot$, if we correct for an extinction of

$A_K = 2.5$ mag and use the PDR model of Black & van Dishoeck (1987) to extrapolate to the H_2 cooling in all lines ($I_{H_2 v=1-0S(1)}/I_{H_2} = 0.016$). The ratio of the near-IR H_2 luminosity to the luminosity in the far-UV band that is effective in exciting H_2 is 0.028, which is close to the value of 0.034 from an appropriate PDR model for the Galactic center (Model 19 in Black & van Dishoeck 1987, which has $n_H = 10^4$ and a UV field $I_{UV} = 10^3$). Therefore the UV-excitation can explain the observed H_2 strength.

The far-IR continuum intensities along our Galactic center strip are typically 0.8 ergs s^{-1} cm^{-2} sr^{-1} (Odenwald and Fazio 1984). If all of this emission arises from a single molecular cloud surface filling the beam, it corresponds to a far-UV flux $\sim 2 \times 10^3$ times the mean interstellar radiation field in the solar neighborhood (Draine 1978). Given the likely number of clouds along each line of sight and various geometric effects, the likely far-UV field is $500 - 1000$ times the solar neighborhood value. For this range of UV field strengths and densities between 3×10^3 and 3×10^4 cm^{-3}, Black and van Dishoeck (1987) predict H_2 (1,0) S(1) line intensities in the range $1.2 - 4.2 \times 10^{-5}$ ergs s^{-1} cm^{-2} sr^{-1}, bracketing our typical observed, de-reddened value.

The H_2 emission from the circum-nuclear disk appears to be collisionally excited ($I((2,1) S(1))/I((1,0) S(1)) \simeq 0.1$, Gatley et al. 1984). Gatley et al. suggest that shocks created by mass outflow from the Galactic nucleus might excite the H_2. Such thermal line ratios can also occur, however, in UV-excited gas if the UV fields and densities are sufficiently high (Sternberg and Dalgarno 1989; Luhman et al. 1997). The line ratio does not prove that the molecular gas is heated dynamically by shock waves, because quiescent dense neutral gas, which is heated radiatively by UV photons, emits thermal H_2 line radiation. Since the typical hydrogen density in the circum-nuclear disk is large, i.e., $n_H \simeq 10^5$ cm^{-3}, and the UV field is intense in the central 3 pc, (the number of total Lyman continuum photons absorbed by the gas is $\sim 2 \times 10^{50}$ s^{-1}, Lacy et

al. 1980), the strength and character of the H_2 emission from the circumnuclear disk are also consistent with UV-excitation.

3.4.3 Shock-Excitation

Shock excitation of the H_2 (1,0) S(1) transition must take place, at some level, in the inner 400 pc of the Galaxy. A large variety of dynamical activity may give rise to shocks with appropriate characteristics. Outflows around newly formed stars and shocks caused by supernova remnants impinging on molecular clouds in the galactic disk both produce H_2 emission and should be observable in the Galactic Center. Bally et al (1987; 1988) surveyed the Galactic center region in the CO and ^{13}CO $J = 1 \rightarrow 0$, and CS $J = 2 \rightarrow 1$ lines. The gas distribution is highly asymmetric about the center, and some negative velocity gas is seen at positive longitudes, which is "forbidden" to gas in circular orbits. This gas and other clouds with eccentric orbits may collide with material in more circular orbits. For example, in the Sgr B_2 complex, Hasegawa et al. (1994) suggested that a dense ($n(H_2) \simeq 1.4 \times 10^4$ cm^{-3}), 10^6 $M_\odot$ "Clump" ($l = +0.\!\!^\circ68$, $b = -0.\!\!^\circ03$) has collided with the extended less dense "Shell" of the cloud complex producing a ~ 30 km s^{-1} shock. Finally, the internal velocity dispersion of the molecular clouds is in the range of $\Delta V = 20 - 50$ km s^{-1} (Bally et al. 1988). If the internal collisions efficiently dissipate the relative kinetic energy by radiative cooling following shocks, there should be H_2 emission throughout the molecular clouds, much of it, however, heavily extincted.

Depending on the context, shock-excited H_2 emission could result either from dissociative J-shocks (colliding clouds, supernova remnants), or from C-shocks (outflows, dissipation of turbulence). The J-shocks give rise to H_2 (1,0) S(1) intensities in the range of $3 \times 10^{-5} - 10^{-4}$ ergs s^{-1} cm^{-2} sr^{-1} with the intensity being fairly insensitive to density and shock velocity over the range 10^4cm$^{-3} \leq n_H \leq 10^5$cm^{-3} and 30 km s$^{-1} \leq v_{shock} \leq 150$ km s^{-1} (Hollenbach &

McKee 1989). For $A_K = 2.5$ mag, the predicted intensity matches what we observe in the Galactic center fairly well. In order to explain the distribution of observed H_2 emission, however, the number of shock fronts times the area covered per beam must roughly equal the beam area along virtually every line of sight through the inner 400 pc of the Galaxy, an unlikely picture at best.

C-shocks can produce H_2 (1,0) S(1) intensities in the range of those observe in the Galactic Center. A single C-shock with $n_H = 10^4 \mathrm{cm}^{-3}$ and $V = 20$ km s^{-1} gives $I_{S(1)} \simeq 3 \times 10^{-5}$ ergs s^{-1} cm^{-2} sr^{-1} (Draine, Roberge, & Dalgarno 1983). The emergent intensity, however, is extremely sensitive to the shock velocity, varying (at $n_H = 10^4$ cm^{-3}) by 3 orders of magnitude from $V_{shock} = 18$ to $V_{shock} = 40$ km s^{-1}. A model making use of C-shocks to produce the observed uniform H_2 (1,0) S(1) distribution would have to be somewhat contrived. While there may be some shock-excited H_2 emission from the Galactic Center, it is difficult to argue away the expected PDR emission and then construct a reasonably simple shock model capable of explaining the observations. A reliable test of the excitation mechanism would be to observe H_2 transitions arising higher above ground than the (1,0) S(1) line (see Chapter 4 in this dissertation).

3.4.4 Total H_2 Luminosity

To estimate the total H_2 luminosity of the Galactic Center, we extrapolate from our 400 pc long strip by assuming that the scale height of the H_2 emission equals that of the far-IR radiation ($h \simeq 0°.2$, Odenwald & Fazio 1984). For $A_K = 2.5$ mag and $f \leq 1$ (see Section 3.4.1), the de-reddened H_2 (1,0) S(1) luminosity in the inner 400 pc diameter of the Galaxy is 8.0×10^3 $L_\odot$. Joseph (1989) gives ranges of H_2 (1,0) S(1) luminosity in > 1 kpc regions for various classes of galaxies: (1) merging galaxies: $3 \times 10^6 - 3 \times 10^8$ $L_\odot$; (2) interacting galaxies: $10^5 - 10^7$ $L_\odot$; (3) barred spirals: $10^4 - 10^6$ $L_\odot$. Over its inner ~ 1 kpc,

our Galaxy most likely falls within the range for barred spirals.

In ultraluminous infrared bright galaxies ($L_{IR} \gtrsim 10^{12} \ L_{\odot}$), Goldader et al. (1995) show that $\log(L_{S(1)}/L_{FIR}) = -4.95 \pm 0.22$. For the nearby starburst M82. we can use H_2 (1,0) S(1) measurements of the inner $60''$ (Pak & Jaffe, unpublished) together with far-IR continuum observations (D. A. Harper, as quoted in Lugten et al. 1986) to derive $\log(L_{S(1)}/L_{FIR}) = -5.2$ for the inner 1 kpc. For the inner 400 pc of the Milky Way, the data presented here yield $\log(L_{S(1)}/L_{FIR}) = -4.8$.

There is evidence in some high-luminosity galaxies that the H_2 emission results from UV-excitation. In NGC 3256, a merging galaxy, the H_2 (2,1) S(1)/(1,0) S(1) line ratio in the 600 pc region ($3''\!.5 \times 3''\!.5$) is 0.39 ± 0.06, suggesting that UV fluorescence is responsible for at least 60 % of the H_2 (1,0) S(1) emission (Doyon, Wright, & Joseph 1994) . If H_2 in the Galactic center is UV-excited, as we suggest here, this mechanism could be shared by H_2 emission from galaxies with an enormous range of nuclear conditions.

3.5   Conclusions

We have surveyed the inner 400 pc diameter of the Galaxy in the H_2 (1,0) S(1) emission line. The emission is extremely widespread and has a typical dereddened intensity of 3×10^{-5} ergs s^{-1} cm^{-2} sr^{-1}. Empirical and theoretical models of PDR's both indicate that UV-excitation can explain the strength and distribution of the H_2 emission. Observations of extended (6,4) Q(1) emission in Orion unambiguously demonstrate that the extended H_2 in that source is UV-excited (Luhman et al. 1994). Comparable observations in the Galactic center would be difficult but are possible.

The total H_2 (1,0) S(1) luminosity in the 400 pc of the Galaxy is $8.0 \times 10^3 \ L_{\odot}$, an order of magnitude larger than that in the strong and compact circum-nuclear gas ring ($7 \times 10^2 \ L_{\odot}$). The luminosity ratio of the H_2 (1,0) S(1)

to far-IR in the Galaxy agrees with that in starburst galaxies and in ultraluminous infrared bright galaxies.
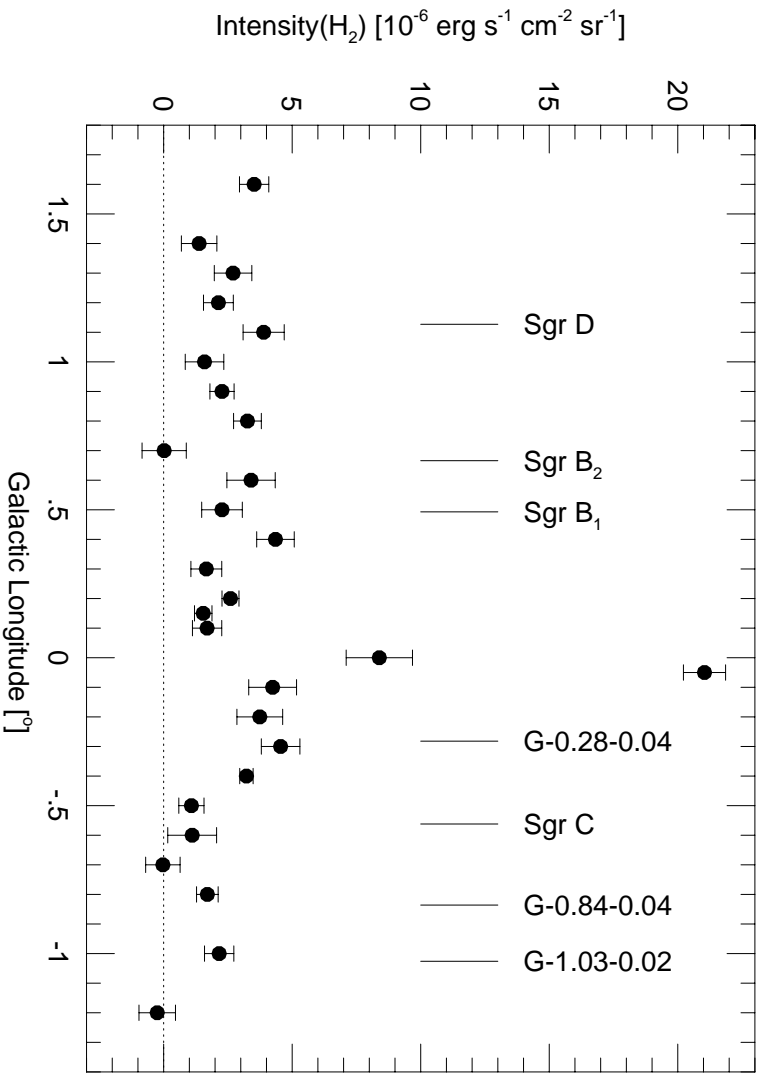
Figure 3.1.— Observed intensity distribution of H_2 (1,0) S(1) ($\lambda = 2.1215 \, \mu m$) along the Galactic Plane at $b = -0°.05$. The beam size was $3'.3$ (8.2 pc at the Galactic center). The intensity values have not been corrected for interstellar extinction. The error bars represent 1σ measurement uncertainties. The strongest emission at $l = -0°.05$ is from Sgr A. The vertical lines give the positions of the prominent radio continuum sources (Altenhoff et al. 1978).

39
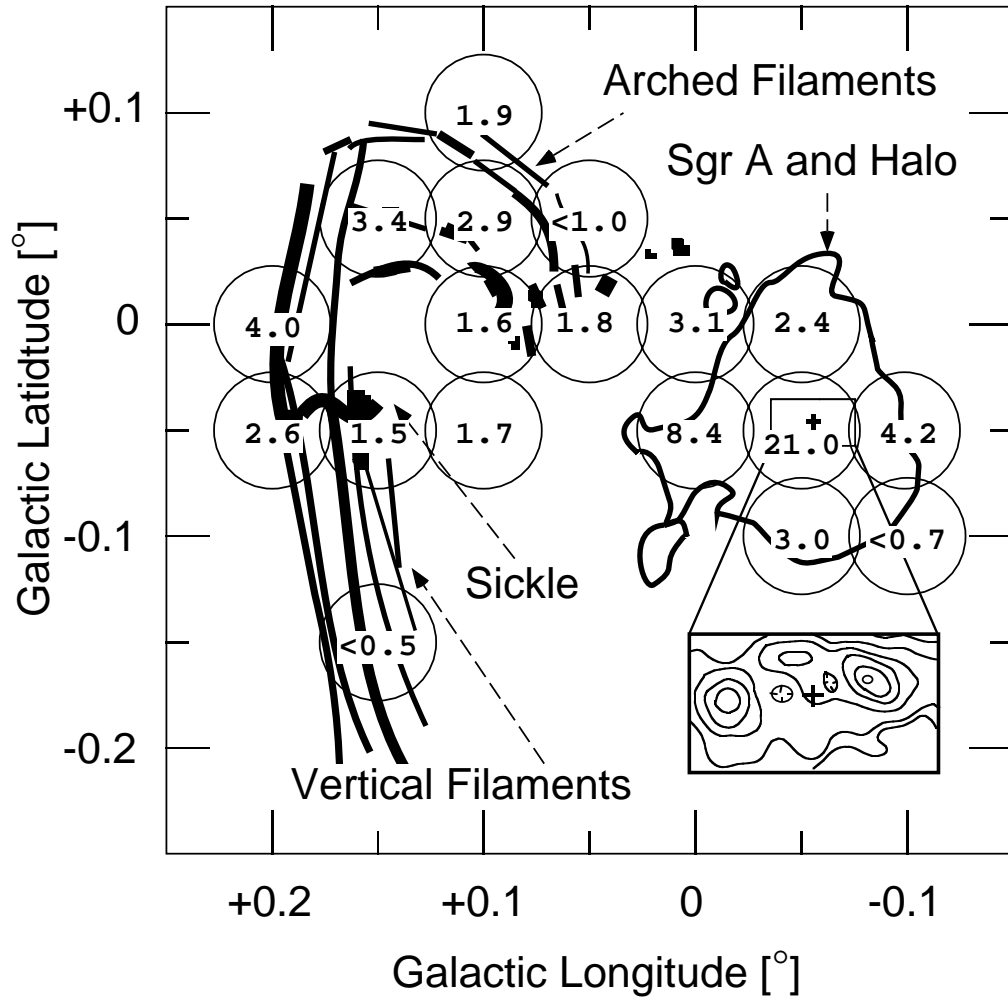
Figure 3.2.— Positions (circles with a diameter of the telescope beam size, 3.3) and measured H_2 intensities (numbers inside the circles in units of 10^{-6} ergs s^{-1} cm^{-2} sr^{-1}) observed in H_2 (1,0) S(1) in the inner 50 pc of the Galaxy. Typical measurement uncertainties are 0.7×10^{-6} ergs s^{-1} cm^{-2} sr^{-1}. The heavy lines show a schematic version of the radio continuum distribution (Yusef-Zadeh, Morris, & Chance 1984). The small box and inset show the H_2 (1,0) S(1) distribution in the circum-nuclear gas ring (Gatley et al. 1986). The plus sign is at Sgr A* ($l = -0.0558, b = -0.0462$).

REFERENCES

Altenhoff, W. J., Downes, D., Pauls, T., & Schraml, J. 1978 A&AS, 35, 23

Bally, J., Stark, A. A., Wilson, R. W., & Henkel, C. 1987, ApJS, 65, 13

Bally, J., Stark, A. A., Wilson, R. W., & Henkel, C. 1988, ApJ, 324, 223

Black, J. H., & van Dishoeck, E. F. 1987, ApJ, 322, 412

Blitz, L., Binney, J., Lo, K. Y., Bally, J., Ho, P. T. P. 1993, Nature, 361, 417

Catchpole, R. M., Whitelock, P. A., & Glass, I. S. 1990, MNRAS, 247, 479

Doyon, R., Wright, G. S., & Joseph, R. D. 1994, ApJ, 421, 115

Draine, B.T. 1978, ApJS, 36, 595

Draine, B. T., Roberge, W. G., & Dalgarno, A. 1983, ApJ, 264, 485

Fullmer, L. & Lonsdale, C. 1989, Catalogued Galaxies and Quasars Observed in the IRAS Survey, version 2, (Pasadena: Infrared Processing and Analysis Center, JPL D-1932).

Gatley, I., Jones, T. J., Hyland, A. R., Beattie, D. H., Lee, T. J. 1984, MNRAS, 210, 565

Gatley, I., Jones, T. J., Hyland, A. R., Wade, R., Geballe, T. R., & Krisciunas, K. 1986, MNRAS, 222, 299

Gatley, I, & Merrill, M. 1993, in SPIE Vol. 1946, Infrared Detectors and Instrumentation, ed. A. M. Fowler, 2

Glass, I. S., Catchpole, R. M., & Whitelock, P. A. 1987, MNRAS, 227, 373

Goldader, J. D., Joseph, R. D., Doyon, R., & Sanders, D. B., 1995, ApJ, 444, 97

Güsten, R. 1989, in IAU Symp. 136, The Center of the Galaxy, ed. M. Morris (Dordrecht: Kluwer), 89

Hasegawa, T., Sato, F., Whiteoak, J. B., & Miyawaki, R. 1994, ApJ, 429, L77

Hollenbach, D. J., Chernoff, D. F., &McKee, C. F. 1989, in Proc. 22nd ESLAB Symposium, Infrared Spectroscopy in Astronomy, ed. B. Kaldeich (Noordwijk: ESA SP-290), 245

Hollenbach, D.J., & McKee, C.F. 1989, ApJ, 342, 306

Joseph, R. D. 1989, in Proc. 22nd ESLAB Symposium, Infrared Spectroscopy in Astronomy, ed. B. Kaldeich (Noordwijk: ESA SP-290), 439

Lacy, J. H., Townes, C. H., Geballe, T. R., & Hollenbach, D. J. 1980, ApJ, 281, 132

Lester, D. F., Carr, J. S., Joy, M., & Gaffney, N. 1990, ApJ, 352, 544

Lis, D. C., & Carlstrom, J. E. 1994, ApJ, 424, 189

Lugten, J.B., Watson, D.M., Crawford, M.K., & Genzel, R. 1986, ApJ, 311, L51

Luhman, M.L., & Jaffe, D.T. 1996, ApJ, 463, 191

Luhman, M. L., Jaffe, D. T., Keller, L. D., & Pak, S. 1994, ApJ, 436, L185

Luhman, M. L., Jaffe, D. T., Keller, L. D., & Pak, S. 1995, PASP, 107, 184

Luhman, M. L., Jaffe, D. T., Sternberg, A., Herrmann, F., & Poglitsch, A. 1997, ApJ, 482 (June 10 issue)

Mezger, P. G., Smith, L. F., & Churchwell, E. 1974, A&A, 32, 269

Mezger, P. G., & Pauls, T. 1979, in IAU Symp. 84, The Large-Scale Characteristics of the Galaxy, ed. W. B. Burton, 357

Moorwood, A. F. M., & Oliva, E. 1990, A&A, 239, 78

Odenwald, S. F., & Fazio, G. G. 1984, ApJ, 283, 601

Oliva, E., & Origlia, L. 1992, A&A, 254, 466

Oort, J. 1977, ARA&A, 15, 295

Plume, R. 1995, Ph.D. dissertation in the University of Texas at Austin

Puxley, P., Hawarden, T., & Mountain, M. 1988 in Proc. 22nd ESLAB Symposium, Infrared Spectroscopy in Astronomy, ed. B. Kaldeich (Noordwijk: ESA SP-290), 517

Sodroski, T.J. et al. 1994, ApJ, 428, 638

Sofue, Y. 1985, PASJ, 37, 697

Sternberg, A., & Dalgarno, A. 1989, ApJ, 338, 197

Yusef-Zadeh, F., Morris, M., & Chance, D. 1984, Nature, 310, 557

Chapter 4

H_2 Excitation Mechanism in the Central Regions of Galaxies

ABSTRACT

We have observed near-IR H_2 line emission on large scales in the Galactic center and NGC 253. Chapter 3 discussed our 400 pc long strip map and 50 pc map of the H_2 (1,0) S(1) line. In this chapter, we present observations of the higher vibrational lines (H_2 (2,1) S(1) and (3,2) S(3)) at selected positions and conclude that strong far-UV radiation excites the H_2. We compare the H_2 (1,0) S(1) emission to far-IR continuum emission and show that the ratio of these two quantities in the Galactic center equals the ratio seen in the starburst galaxies, M82 and NGC 253, and in ultraluminous infrared bright galaxies.

4.1   Introduction

The central kpc regions in starburst galaxies and ultraluminous IR bright galaxies are powerful emitters of near-IR H_2 emission (Puxley, Hawarden, & Mountain 1990; Goldader et al. 1995). Ro-vibrational lines of H_2 can trace both photon-dominated regions (PDRs), where far-UV photons excite the H_2, and shocked regions, where the H_2 is thermally excited. Vigorous star formation in these galaxies produces large numbers of UV photons which fluorescently excite H_2, while subsequent supernovae shock-excite the H_2.

We have used the University of Texas near-IR Fabry-Perot Spectrometer, to survey giant molecular clouds (GMCs) on $1 - 10$ pc scales (Luhman et at. 1994; Luhman & Jaffe 1996; Luhman et al. 1996). In Orion A, for example, the H_2 (1,0) S(1) line emission extends up to 8 pc (1°) from the central UV source, θ^1 Ori C. The detection of higher vibrational state H_2 lines, e.g., (6,4) Q(1) and (2,1) S(1), showed that far-UV photons excite the H_2. Although the shock-excited H_2 emission is intense in the Orion $BN - KL$ region, the emission region is relatively compact ($\sim 1'$). The total H_2 luminosity in the $BN - KL$ region is only $\sim 1\%$ of the Orion PDR H_2 luminosity. Similarly, UV-excited H_2 dominates the large-scale H_2 emission from other GMCs.

We have observed the H_2 emission in the inner ~ 400 pc ($\sim 3°$) of our Galaxy in order to investigate H_2 emission on a more global scale and to compare the Galactic center with central ~ 1 kpc regions in external galaxies. The physical conditions in the interstellar medium of the Galactic center are significantly different from those in the solar neighborhood. The thin disk (diameter of 450 pc, height of 40 pc) of dense interstellar material in the Galactic center contains $M(H_2) > 2 \times 10^7 M_\odot$ (Güsten 1989). The molecular clouds in the Galactic center have higher density, higher metallicity, and higher internal velocity dispersion than the clouds in the solar neighborhood (Blitz et al. 1993). There is strong radio continuum radiation from giant H II regions (Sgr A, Sgr B, Sgr C, and Sgr D) and extended low-density (ELD) ionized gas. The spectral index in the areas away from the discrete H II regions shows that thermal bremsstrahlung from ionized gas can account for about half of the emission from the extended gas (Sofue 1985). Another indicator of the intense UV radiation in the central 400 pc is strong far-IR continuum emission (Odenwald & Fazio 1984). About 90% of the far-UV energy is absorbed by dust and reradiated in the far-IR. From the far-IR intensity, we estimate that the far-UV radiation field is $\sim 10^3$ times the value in the solar neighborhood ($I_\circ = 4 \times 10^{-4}$ ergs s^{-1} cm^{-2} sr^{-1}, Draine 1978). The energetic conditions in the

Galactic center mean that the center can provide a unique view of the interaction between stellar UV radiation and molecular clouds, and serve as a nearby model for the nuclei of galaxies.

In Chapter 3 we showed the distribution of H_2 (1,0) S(1) emission along a 400 pc-long strip and in the inner 50 pc of the Galactic center. We detected H_2 emission throughout the surveyed region. The typical dereddened ($A_K = 2.5$ mag) H_2 (1,0) S(1) intensity, $\sim 3 \times 10^{-5}$ ergs s^{-1} cm^{-2} sr^{-1}, is similar to the surface brightness in Galactic PDRs (Luhman & Jaffe 1996). In this chapter, we present observations of several H_2 lines, discuss the excitation mechanism, and compare the Galactic center observations to observations of other galaxies.

4.2 Observations and Results

We observed three H_2 emission lines: (1,0) S(1) ($\lambda = 2.121$ μm), (2,1) S(1) ($\lambda = 2.247$ μm), and (3,2) S(3) ($\lambda = 2.201$ μm), at the Cerro Tololo Inter-American Observatory 1.5 m telescope in 1995 July and October. We used the University of Texas Near-Infrared Fabry-Perot Spectrometer. The instrument was specially designed to observe very extended, low surface brightness objects, and has a single channel InSb detector with diameter of 1 mm to maximize the beam size (Luhman et al. 1995). The telescope ($f/30$), a collimator (effective focal length 686 mm), and a field lens (effective focal length 20mm) produce a beam diameter of 1$.\!\!'$35 (equivalent disk).

The Fabry-Perot interferometer operates in 94th order ($\lambda_o = 2.121\mu$m) with an effective finesse of 26, yielding a spectral resolution of 125 km s^{-1} (FWHM). Our scans covered 15 sequential steps, ± 300 km s^{-1} centered at V_{LSR} $\simeq 0$ km s^{-1}. In order to subtract background and telluric OH line emission, we chopped the secondary mirror to $\Delta b = +16'$ or $-16'$ at 0.5 Hz.

We observed five positions: $(l, b) = (-0\!\!.\!\!^\circ0433, -0\!\!.\!\!^\circ0462)$, $(-0\!\!.\!\!^\circ0683, -0\!\!.\!\!^\circ0462)$, $(0\!\!.\!\!^\circ00, -0\!\!.\!\!^\circ05)$, $(-0\!\!.\!\!^\circ30, -0\!\!.\!\!^\circ05)$, and $(+1\!\!.\!\!^\circ60, -0\!\!.\!\!^\circ05)$. In Figure 4.1,

we plot the new H_2 (1,0) S(1) data overlaid on the data from Chapter 3 and compare the two data sets. The $3\!\!''\!\!.3$ beam of the McDonald 0.9 m telescope centered at Sgr A* ($l = -0\!\!°\!\!.0558$, $b = -0\!\!°\!\!.0462$) covers the whole circumnuclear gas ring (Gatley et al. 1986), while, with the $1\!\!''\!\!.35$ beam of the CTIO 1.5 m telescope, we observed the $+\Delta l$ H_2 peak ($-0\!\!°\!\!.0433$, $-0\!\!°\!\!.0462$) and the $-\Delta l$ H_2 peak ($-0\!\!°\!\!.0683$, $-0\!\!°\!\!.0462$). The difference between the $3\!\!''\!\!.3$ beam data and the $1\!\!''\!\!.35$ beam data toward Sgr A is an effect of different beam sizes because the H_2 emission sources are relatively compact. In the large-scale emission beyond Sgr A, the two data sets agree to within the errors, indicating that the H_2 emission varies slowly on $1' - 3'$ scales.

4.3 Extinction Correction

The extinction in K-band toward the Galactic center is significant. Figure 4.2 shows the classification of the extinction into *foreground extinction* by material in spiral arms at $R = 4 - 8$ kpc, and *Galactic center extinction* by material in the Galactic center clouds. Catchpole, Whitelock, & Glass (1990) measured the foreground extinction as $A_K \simeq 2.5$ mag.

A discussion of the Galactic center extinction requires a different approach because individual clouds in the Galactic center are almost opaque in the near-IR ($A_K = 10 - 30$ mag for typical clouds of $D \simeq 10$ pc and $n(H_2)$ $\simeq 10^4$ cm^{-3}). If the UV-excited H_2 emission arises on the cloud surfaces, we need only consider the effects of shadowing by other Galactic center clouds (see Figure 4.3). From millimeter observations of CO $J = 1 \rightarrow 0$ emission, we can estimate the velocity-integrated area filling factor of clouds, f. If the millimeter telescope beam size is smaller than the individual clouds and covers only one cloud along the line-of-sight, the area filling factor, f, is 1. The upper diagram in Figure 4.3 shows an expected CO $J = 1 \rightarrow 0$ spectrum of typical clouds in the Galactic center which have kinetic temperature of ~ 70 K and line widths

of $\sim$ 20 km s^{-1} (Güsten 1989). In general, the clouds have different sizes and may overlap along the line-of-sight. The lower diagram in Figure 4.3 shows an observed typical CO $J = 1 \rightarrow 0$ spectrum where the velocity-integrated intensity is $\sim$ 1500 K km s^{-1} (Bally et al. 1987; Bally et al. 1988). The value f is the ratio of the observed velocity-integrated intensity of CO $J = 1 \rightarrow 0$ to the single typical cloud intensity (70 K $\times$ 20 km s^{-1}). The f toward the Galactic center clouds is $\sim$ 1, implying that there is little or no overlap along a typical line-of-sight. If $f \leq 1$, we only miss the near-IR H$_2$ flux from the back sides of the clouds. If $f > 1$, H$_2$ radiation is blocked by the foreground clouds, and the ratio of the observed H$_2$ flux to the emitted flux is inversely proportional to f. Since $f \simeq 1$, we use the foreground values, $A_K = 2.5$, for the extinction correction.

4.4　H$_2$ Excitation Mechanism

4.4.1　H$_2$ Line Ratios

In UV-excited H$_2$, the branching ratios in the downward cascade determine the relative strengths of the near-IR lines. On the other hand, the energy level populations of shock-excited H$_2$ are thermalized. We use the line intensity ratios of higher vibrational level lines to the (1,0) S(1) line in order to identify the H$_2$ excitation mechanism.

In Figure 4.4, the observed ratios in the large-scale Galactic center and the central 1 kpc region of NGC 253 imply that the H$_2$ emission may result from UV-excitation. In the circumnuclear gas ring ($l = -0°.0433$ and $-0°.0683$), the UV-excited H$_2$ energy levels are partially thermalized because of the relatively high density (Sternberg & Dalgarno 1989; see also Ramsay-Howat, Mountain, & Geballe 1996 for the H$_2$ observations in the circumnuclear gas ring). The determination of line ratios consistent with UV excitation in the large-scale Galactic center and NGC 253 means the gas is not dense enough for collisions

to significantly alter the radiative cascade, $n(H_2) < 10^5$ cm^{-3} (Luhman et al. 1996).

4.4.2 I_{FIR} versus I_{H2}

If large-scale H_2 emission arises in the surface layers of the clouds where far-UV photons can excite the molecules, the dust, which absorbs the bulk of the incident flux, ought to radiate in the far-IR continuum as well. If we de-redden the Galactic center H_2 observations by $A_K = 2.5$ mag, the Galactic center results are consistent with the empirical far-IR vs. H_2 relationship derived for the UV-excited surfaces of clouds in the galactic disk (see Figure 4.5).

4.5   Comparison with Other Galaxies

We extrapolate from our 400 pc long strip to the total H_2 (1,0) S(1) luminosity of the Galactic Center by assuming that the scale height of the H_2 emission equals that of the far-IR radiation ($h \simeq 0°2$, Odenwald & Fazio 1984) and that $A_K = 2.5$ mag and $f \simeq 1$. The H_2 (1,0) S(1) luminosity in the inner 400 pc diameter of the Galaxy is 8.0×10^3 $L_\odot$.

For ultraluminous and luminous infrared bright galaxies ($L_{IR} \gtrsim 10^{11}$ $L_\odot$), Goldader et al. (1995) showed the correlation between L_{FIR} and L_{H2}. We can extend the relationship to nearby starburst galaxies like M82 and NGC 253, and to the Galactic center (see Figure 4.6). The strong correlation between the far-IR and H_2 luminosity for various classes of galaxies indicates that the far-UV radiation may excite large scale H_2 emission in all of these sources.
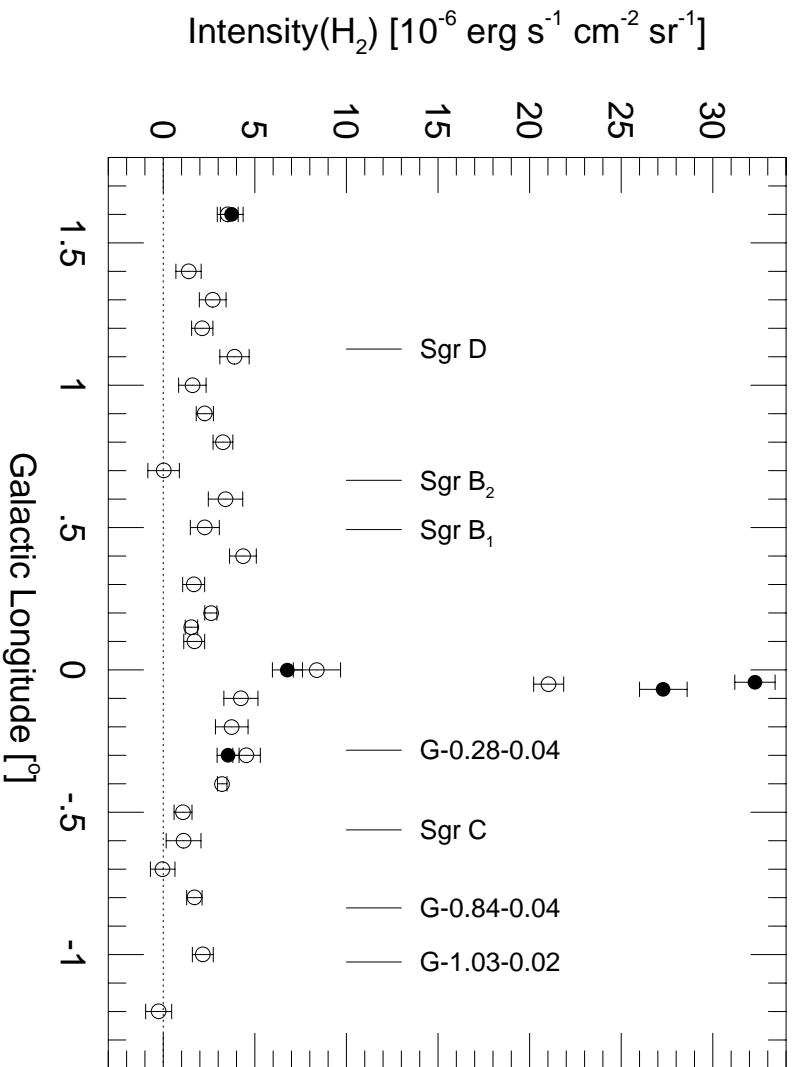
Figure 4.1.— Observed intensity distribution of H_2 (1,0) $S(1)$ ($\lambda = 2.121$ μm) along the Galactic plane at $b = -0°\!.05$. The open circles were taken at the McDonald 0.9 m telescope with a 3″.3 beam (Chapter 3) and the filled circles at the CTIO 1.5 m telescope with a 1″.35 beam. The intensities have not been corrected for interstellar extinction. The error bars represent 1σ measurement uncertainties.

FUV from OB star

UV-excited H$_2$ emission

SN

D ~ 10 pc
n ~ 10^4 cm^{-3}

☉

The Sun

Foreground Extinction
A_k = 2.5 mag

The Galactic Center Cloud Extinction
A_k = 10 - 30 mag
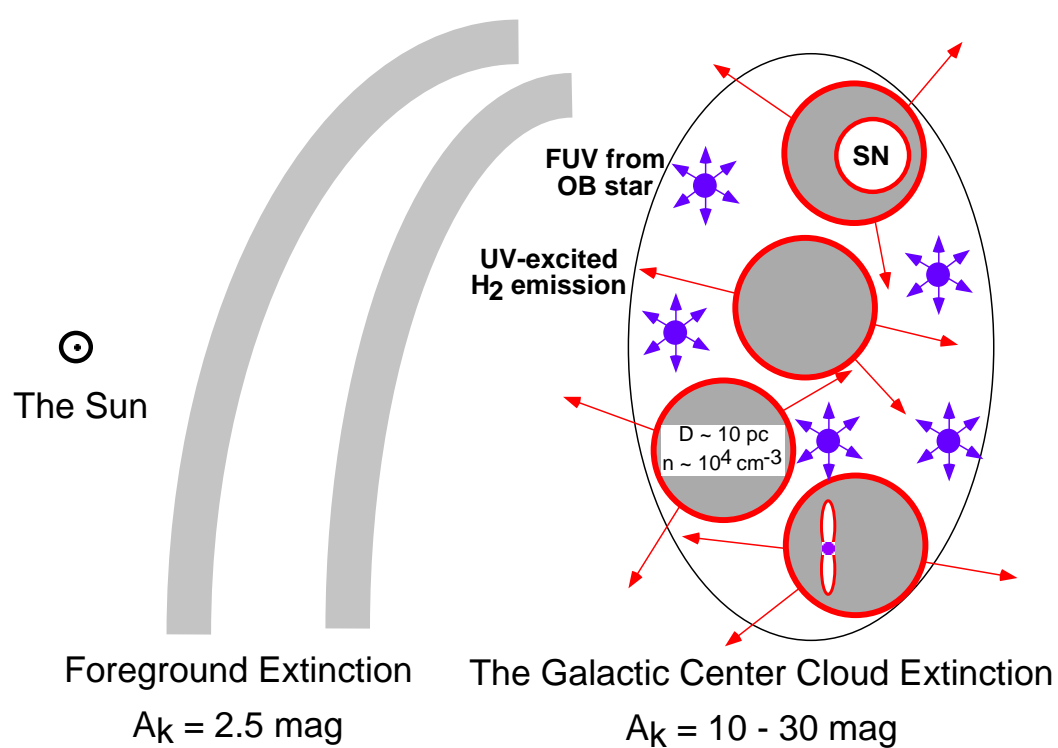
Figure 4.2.— Top-view schematic of the distribution of interstellar material in two foreground spiral arms (foreground extinction) and in the GMCs in the inner ~ 400 pc of the Galaxy (Galactic center extinction).
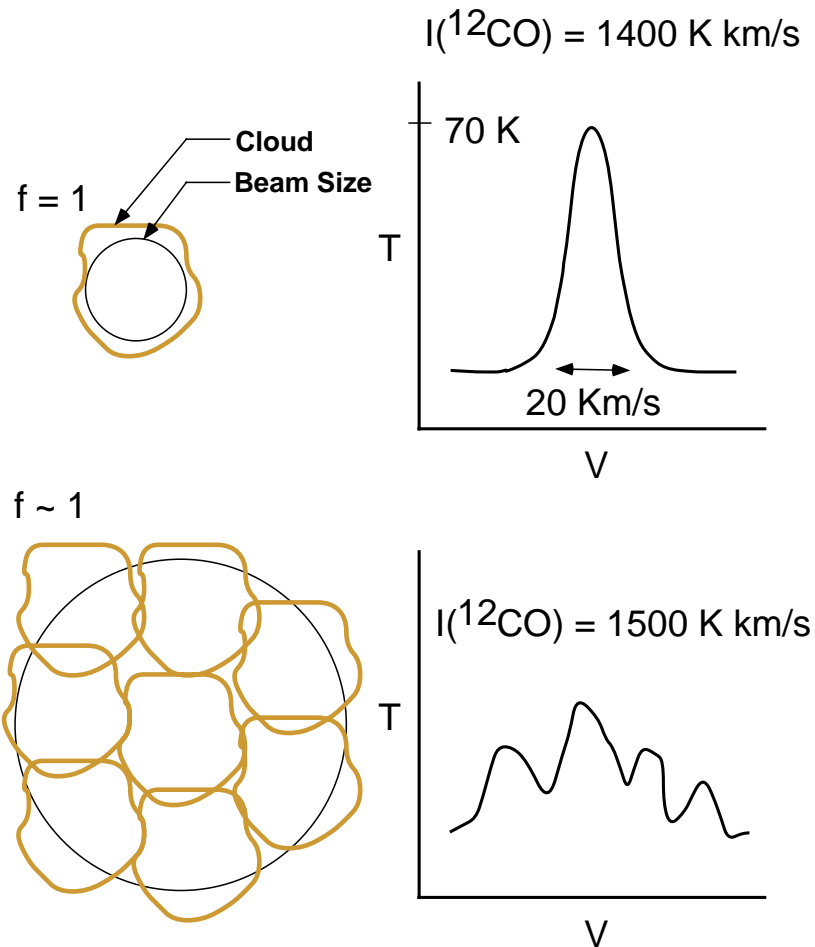
Figure 4.3.— Schematic diagram of small and large beam observations in the Galactic center. CO $J = 1 \rightarrow 0$ spectrum of a typical cloud is beam diluted. The velocity-integrated intensity including the clouds in the beam at other velocities is ~ 1500 K km s^{-1}, which indicates that the area filling factor, f, is ~ 1. The cloud components do not usually overlap along the line-of-sight.
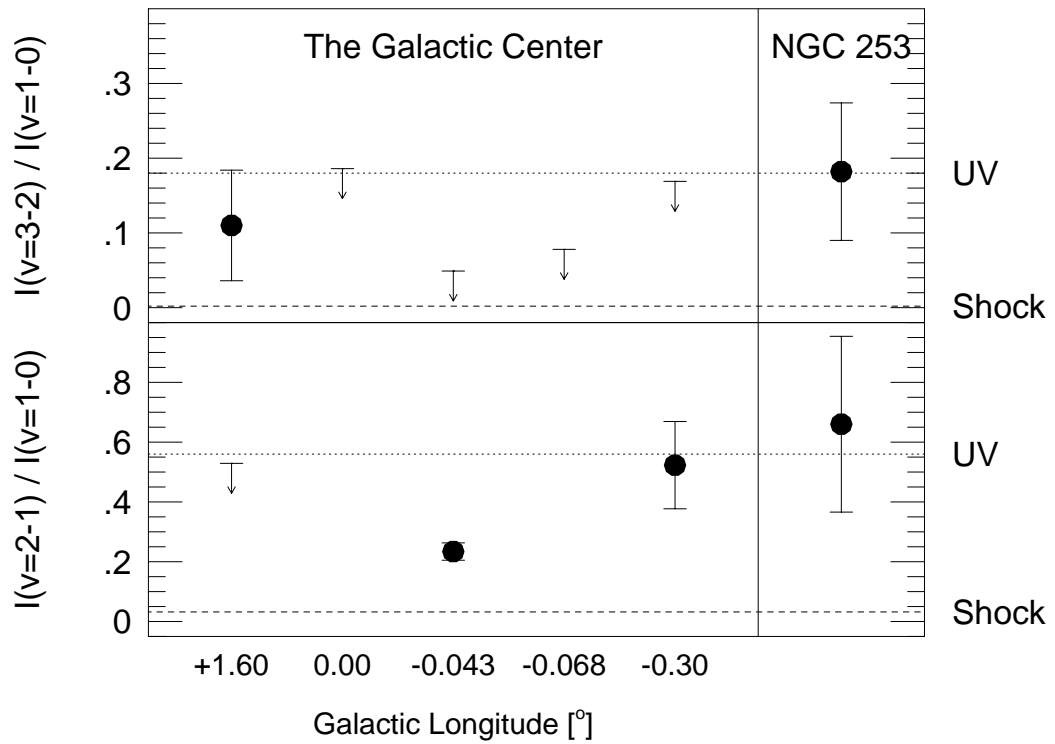
Figure 4.4.— Observed H_2 line ratios at positions along the Galactic Plane ($b = -0°05$) and in the central 1 kpc of NGC 253. The dotted lines are modeled ratios of UV-excited H_2 lines, (Black & van Dishoeck 1987), and shock-excited H_2 lines ($V_{shock} = 30$ km s^{-1}; Draine, Roberge, & Dalgarno 1983). The arrows show the 3σ limits where we did not detect the higher vibrational level lines.
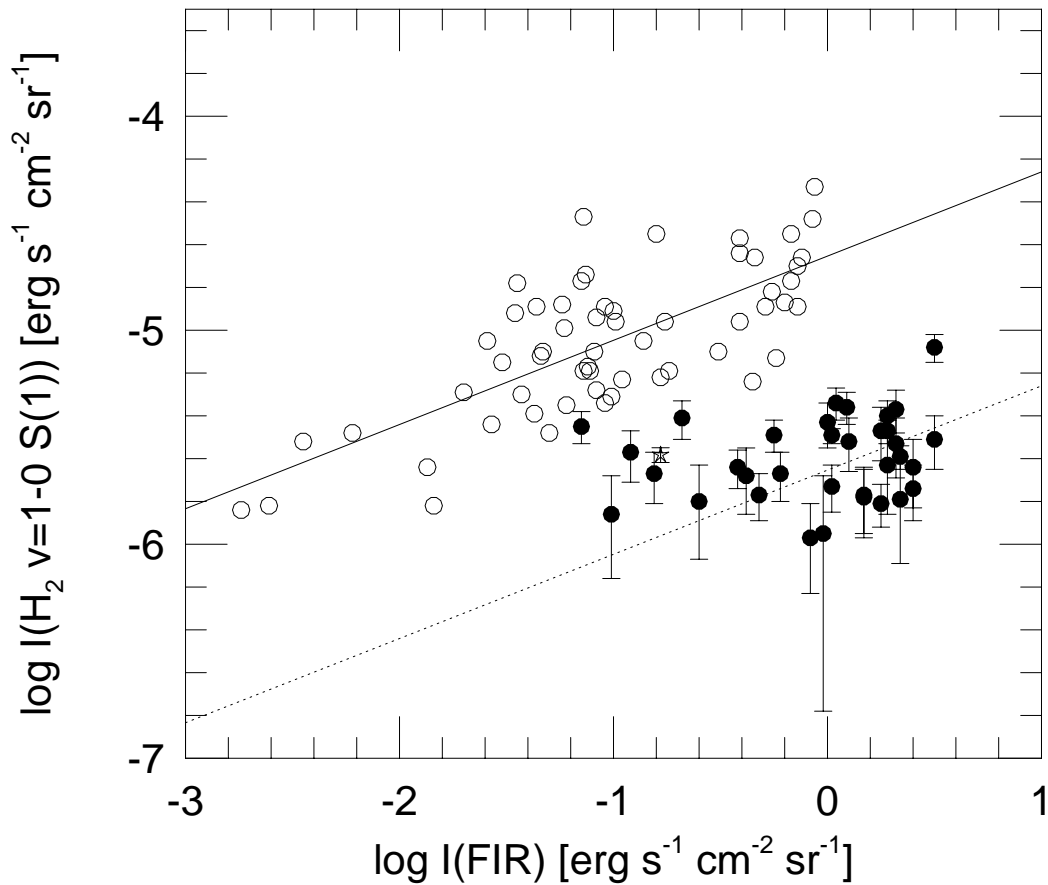
Figure 4.5.— I_{FIR} versus $I(H_2\ (1,0)\ S(1))$ for the Galactic PDRs and the Galactic center. The open circles are from Orion A and B, ρ Ophiuchi, and G236+39 (Luhman & Jaffe 1996), and the filled circles are from the Galactic center (Chapter 3). The Galactic center data are not corrected for extinction. The solid line (log $I_{H2} = -4.65 + 0.39$ log I_{FIR}) is derived from the Galactic PDR data using a least squares method, and the dotted line shows the vertically shifted solid line by $\Delta \log I_{H2} = -1$.
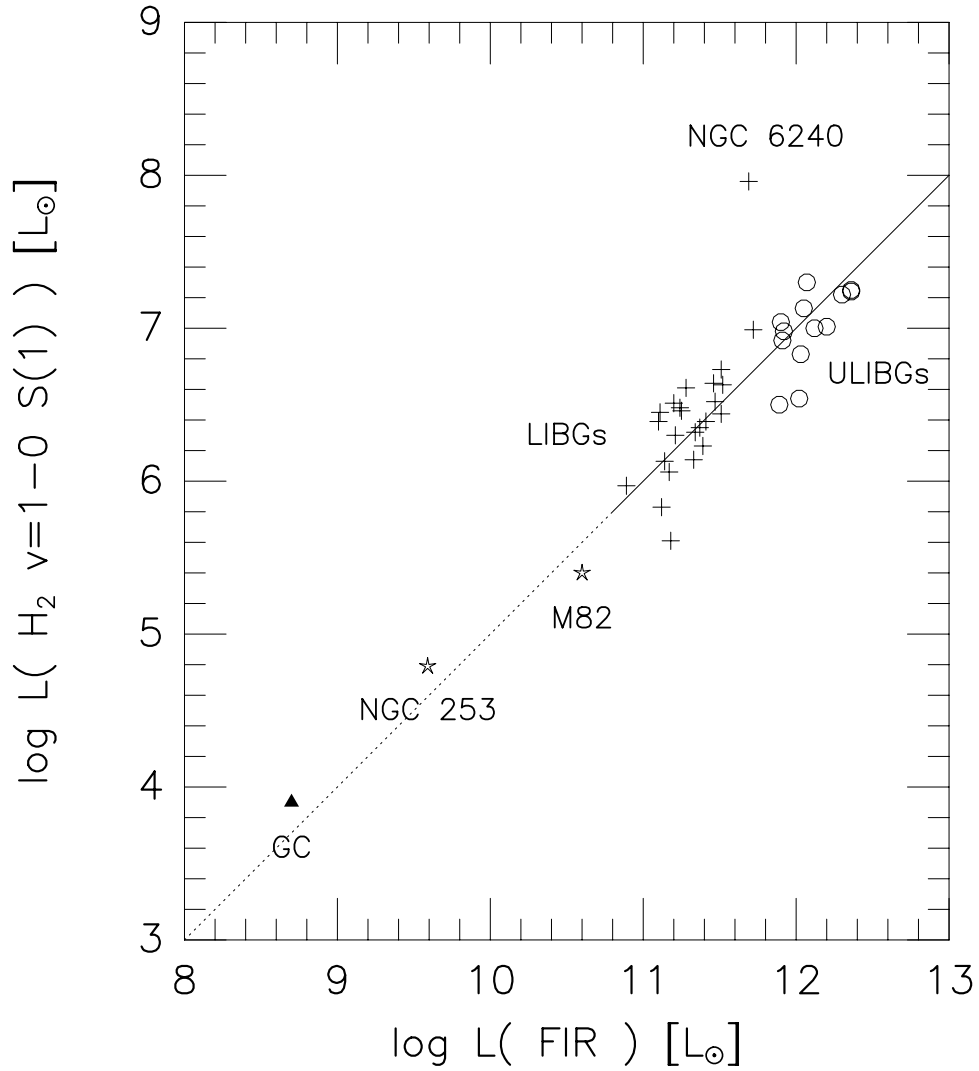
Figure 4.6.— L_{FIR} versus $L(H_2\ (1,0)\ S(1))$ of various kinds of galaxies. The solid line ($\log L_{H2} = -5 + \log L_{FIR}$) is derived from data of ultraluminous IR bright galaxies (open circles) and luminous IR bright galaxies (plus signs, Goldader et al. 1995). The dotted line shows extrapolation from the solid line. The H_2 data of M82 were taken at the McDonald 2.7 m telescope and the H_2 data of NGC 253 at the CTIO 1.5 m telescope, both with the UT FPS. The H_2 (1,0) S(1) luminosities in this figure are corrected for interstellar extinction.

REFERENCES

Bally, J., Stark, A. A., Wilson, R. W., & Henkel, C. 1987, ApJS, 65, 13

Bally, J., Stark, A. A., Wilson, R. W., & Henkel, C. 1988, ApJ, 324, 223

Black, J. H., & van Dishoeck, E. F. 1987, ApJ, 322, 412

Blitz, L., Binney, J., Lo, K. Y., Bally, J., Ho, P. T. P. 1993, Nature, 361, 417

Catchpole, R. M., Whitelock, P. A., & Glass, I. S. 1990, MNRAS, 247, 479

Draine, B.T. 1978, ApJS, 36, 595

Draine, B. T., Roberge, W. G., & Dalgarno, A. 1983, ApJ, 264, 485

Gatley, I., Jones, T. J., Hyland, A. R., Wade, R., Geballe, T. R., & Krisciunas, K. 1986, MNRAS, 222, 299

Goldader, J. D., Joseph, R. D., Doyon, R., & Sanders, D. B. 1995, ApJ, 444, 97

Güsten, R. 1989, in IAU Symp. 136, The Center of the Galaxy, ed. M. Morris (Dordrecht: Kluwer), 89

Luhman, M.L., & Jaffe, D.T. 1996, ApJ, 463, 191

Luhman, M. L., Jaffe, D. T., Keller, L. D., & Pak, S. 1994, ApJ, 436, L185

Luhman, M. L., Jaffe, D. T., Keller, L. D., & Pak, S. 1995, PASP, 107, 184

Luhman, M. L., Jaffe, D. T., Sternberg, A., Herrmann, F., & Poglitsch, A. 1997, ApJ, 482 (June 10 issue)

Odenwald, S. F., & Fazio, G. G. 1984, ApJ, 283, 601

Pak, S., Jaffe, D. T., & Keller, L. D. 1996, ApJ, 457, L43

Puxley, P. J., Hawarden, T. G., & Mountain, C. M. 1990 ApJ, 364, 77

Ramsay-Howat, S. K., Mountain, C. M., & Geballe, T. R. 1996, in the proc. of the 4th ESO/CTIO Workshop, the Galactic Center, ed. R. Gredel, A.S.P. Conf. Series vol. 102, p163

Sofue, Y. 1985, PASJ, 37, 697

Sternberg, A., & Dalgarno, A. 1989, ApJ, 338, 197

Chapter 5

Molecular Cloud Structure in the Magellanic Clouds: Effect of Metallicity

ABSTRACT

We examine the structure of neutral clouds in low metallicity environments. We observed the Magellanic Clouds where the CO emission from star forming clouds is lower than one would expect based on other star formation indicators (e.g., Hα emission and H I content). Two possibilities have been suggested to explain the low CO luminosity in dwarf irregular galaxies: (1) Most CO molecules are dissociated by intense UV fields from the local massive young stars; (2) For a given far-UV field, the CO core in a spherical cloud becomes smaller as the metallicity and the dust-to-gas ratio become smaller ("spherical geometry" effect). To examine the first possibility, we observed near-IR H$_2$ (1,0) S(1), (2,1) S(1), and (5,3) O(3), lines and the ^{12}CO $J = 1 \rightarrow 0$ line from 30 Doradus and N159/N160 in the Large Magellanic Cloud and from SMC-B1, SMC-B2, and LIRS 36 in the Small Magellanic Cloud. We also used published [C II] 158 μm line data at the same positions. We find that the H$_2$ emission is UV-excited and that CO emission always (in our surveyed regions) exists toward positions where H$_2$ and [C II] emission have been detected. In other words, there are no large-scale molecular regions where CO is completely dissociated. To examine the effect of spherical geometry, we compiled data sets of H$_2$ (1,0) S(1), CO $J = 1 \rightarrow 0$, and [C II], from the Magellanic Clouds as well as from Galactic star formation regions (Orion and NGC 2024). We used a PDR code and a radiative transfer code to simulate the line

emission from spherical clouds and from large planar clouds. Because the [C II] emission and H_2 emission arise on the surface of the cloud and the lines are optically thin, these lines are not affected by spherical geometry, while the CO emission can be strongly affected. We deduce the expected size of clouds by measuring the deviation of CO emission strength from that predicted by a planar cloud model. The average cloud size increases as the metallicity decreases. A possible reason for such behavior was given by McKee (1989), who suggested that the ionization state in molecular clouds is controlled by far-UV photons and the ability of clouds to resist collapse depends on the fractional ionization.

5.1   Introduction

Stars form in dense, cold molecular clouds. Measuring the molecular gas content of the clouds is very important, if we are to estimate the star formation efficiency and relate it to the properties of the clouds and to their environments. The total H_2 mass, however, cannot be measured directly, because the lowest levels of H_2 from which the observable emission can arise have excitation energies ($\Delta E/k \simeq 500$ K, $J = 2$ to 0) too high to be thermally excited in the cold (< 50 K) molecular clouds. In the Milky Way, the molecular gas content has been traced indirectly using the strength of the optically thick CO $J = 1 \rightarrow 0$ line[1] which has been related to H_2 column density via the virial theorem ($\alpha^{GAL} = (2.5 - 4.1) \times 10^{20}$ cm^{-2}/(K km s^{-1}), Solomon et al. 1987), or via gamma-ray emission ($\alpha^{GAL} = 2.8 \times 10^{20}$ cm^{-2}/(K km s^{-1}), Bloemen et al. 1986). Can we apply this conversion factor to clouds in other galaxies where the physical environments, especially the metallicities, are much different from the Galactic clouds? By measuring the CO $J = 1 \rightarrow 0$ luminosities and the virial masses of the Local Group galaxies, observers have found that the empirical conversion

---

[1]In this chapter, CO denotes ^{12}CO, and the CO $J = 1 \rightarrow 0$ intensity means the velocity integrated main beam brightness temperature, $I = \int T_R^* \, dv$.

factor increases as the metallicity of the individual galaxy decreases (Cohen et al. 1988; Wilson 1995; Arimoto, Sofue, & Tsujimoto 1996).

In this chapter, we discuss observations of individual molecular clouds in the Large Magellanic Cloud (LMC) and the Small Magellanic Cloud (SMC). With these observations, we use numerical models to learn about how metallicity changes affect the chemistry and physics of molecular cloud boundaries and the overall structure of clouds. The Magellanic Clouds are the best targets for such a study because of their proximity ($d^{LMC} = 50.1$ kpc and $d^{SMC} = 60.3$ kpc, Westerlund 1990); their low metal abundance ($Z_C^{LMC} = 0.28$, $Z_O^{LMC} = 0.54$, $Z_C^{SMC} = 0.050$, and $Z_O^{SMC} = 0.21$, where Z is normalized to the Galactic value; Dufour 1984); and their low dust-to-gas ratio ($\rho_{dust}^{LMC} = 0.25$ and $\rho_{dust}^{SMC} = 0.059$, where ρ is normalized to the Galactic value; Koornneef 1984).

Far-UV photons from massive young stars affect the surfaces of nearby molecular clouds, producing photodissociation regions or photon-dominated regions (hereafter PDRs, Tielens & Hollenbach 1985). In these surface layers, the far-UV photons dominate ionization of atoms and formation and destruction of molecules, and the heating and cooling of the gas. Inside the PDR, absorption by dust, C, and H_2, diminishes the far-UV field. Maloney & Black (1988)[2] and Maloney & Wolfire (1997) modeled the chemical structure of the clouds in the Galaxy, the LMC, and the SMC. In dwarf irregular galaxies, where metallicities and dust-to-gas ratios are lower than those in the Galaxy, far-UV photons penetrate deeper into clouds, and dissociate CO molecules in bigger regions (Israel et al. 1986). Therefore, for a molecular cloud with a given H_2 column density the CO column density is lower in the lower metallicity model. If the cloud column density is high enough to keep a sufficient number ($N(CO) \gtrsim 10^{14}$ cm^{-2}, Tielens & Hollenbach 1985) of CO molecules from dissociating, the

---

[2] Figure 4 in Maloney & Black (1988) is not correct. The figure should be replaced by Figure 2 in Israel (1988) or by Figure 2 in van Dishoeck & Black (1988).

CO $J = 1 \rightarrow 0$ line will still be optically thick, and the CO $J = 1 \rightarrow 0$ line intensity will not depend strongly on the metallicity. On the other hand, if the cloud column density is not high, most of the CO will be dissociated and the resulting CO line will be optically thin and very weak.

In this Chapter, we compare the line intensities of H_2 (1,0) S(1), CO $J = 1 \rightarrow 0$, and [C II] 158 μm emission lines from the PDRs in the Magellanic Clouds. These lines have been measured at 21 positions with similar spatial resolutions ($\sim$ 1$'$ or 15 pc at the distance of the LMC). Some limited regions in the Magellanic Clouds were previously observed in the H_2 lines, (Koornneef & Israel 1985; Israel & Koornneef 1988; Kawara, Nishida, & Taniguchi 1988; Israel & Koornneef 1992; Krabbe et al. 1991; Poglitsch et al. 1995). However, the published [C II] and CO data (Johansson et at. 1994; Poglitsch et al. 1995; Israel et al. 1996) cover more extended regions than the existing H_2 maps. We observed near-IR H_2 emission lines from the Magellanic Clouds with the University of Texas Near-IR Fabry-Perot Spectrometer whose beam size is comparable to the existing [C II] and CO $J = 1 \rightarrow 0$ line data (see Section 5.2). We also observed CO $J = 1 \rightarrow 0$ lines at positions where no emission had been detected at the sensitivity of the existing CO surveys (see Section 5.2). LMC data are compared with the data from the Galactic star formation regions in Section 5.4. In Section 5.5, we apply PDR models resulting from numerical codes to the data, and discuss the inferred differences between the chemical structure of the Galactic clouds and the clouds in the Magellanic Clouds.

5.2   Observations

5.2.1   Near-IR H_2 Emission Lines

We observed the H_2 (1,0) S(1) and (2,1) S(1) lines in 1994 December, and (1,0) S(1) and (5,3) O(3) lines in 1995 October, at the Cerro Tololo Inter-

American Observatory[3] 1.5 m telescope using the University of Texas Near-Infrared Fabry-Perot Spectrometer (UT FPS). The instrument was designed to observe extended, low surface brightness line emission, and has a single 1 mm diameter InSb detector to maximize the area-solid angle product. This product, $A\Omega$, depends on the telescope coupling optics but can be made as large as 4.5×10^{-3} cm^2 sr (Luhman et al. 1995). The beam from the $f/30$ secondary of the telescope is collimated and guided to an H-band or K-band Fabry-Perot interferometer and to a ~ 55 K (solid-liquid nitrogen temperature) dewar in which a doublet camera lens of focal length = 20 mm focuses onto the detector. To select a single order from the Fabry-Perot interferometer, we used a 0.5 % (for the H$_2$ (5,3) O(3) line) or a 1 % (for the H$_2$ (1,0) S(1) and (2,1) S(1) lines) interference filter in the dewar. We used a collimator of focal length = 838 mm in 1994 December run and a collimator of focal length = 686 mm in 1995 October. The change of the collimator affected the beam size and spectral resolution (see Table 5.1). Since the coupling of the 686 mm collimator with the telescope optics is better, the beam profile in 1995 October is much closer to a box-function than 1994 December beam profile (see Figure 5.1).

We aligned the Fabry-Perot etalon every $5 - 8$ minutes by executing an automatic alignment routine (see Chapter 2 in this dissertation). The Fabry-Perot etalon maintained alignment for $15 - 30$ minutes, but the plate separation drifted by the equivalent of $2 - 5$ km s^{-1} per minute. Using telluric OH lines (Oliva and Origlia 1992), we calibrated the wavelength scale to within ± 30 km s^{-1}.

We operated the Fabry-Perot interferometer in *scanning mode* at selected positions and in *frequency switching mode* at most positions. In the scanning mode, the plate separation of the etalon was varied to cover ± 200 km s^{-1}

---

centered at the H_2 line in 15 sequential steps. At each step, we took one exposure with an integration time of $0.5 - 1$ second. Figure 5.2 shows observed H_2 (1,0) S(1) and (5,3) O(3) lines at the 30 Doradus (0, 0) position (see the object list in Table 5.3), and telluric OH lines. The OH (9,7) R_2(2) ($\lambda = 2.12267$ μm, Oliva & Origlia 1992) and the (9,7) R_1(1) ($\lambda = 2.12440$ μm) lines are within the H_2 (1,0) S(1) scan range. In the H_2 (5,3) O(3) spectrum, we can see the red-wing of the OH (4,2) P_1(3) ($\lambda = 1.61242$ μm) line and, one free spectral range displaced, (4,2) P_1(2) ($\lambda = 1.60264$ μm, at $V_{LSR} \simeq 420$ km s^{-1} in Figure 5.2) which penetrated through the blue side of the order sorting filter. The typical intensity of the OH (4,2) P_1(3) and (4,2) P_1(2) lines is $\sim 4 \times 10^{-3}$ ergs s^{-1} cm^{-2} sr^{-1} which is more than 10^3 times the H_2 (5,3) O(3) intensity. The OH intensity fluctuates spatially and temporally. The $1/f$ power spectrum of the temporal fluctuations limits the sensitivity of the system.

In the frequency switching mode, we tuned the Fabry-Perot interferometer to λ_{on} and λ_{off}. One observing cycle consists of four steps: $\lambda_{on} \rightarrow \lambda_{off} \rightarrow \lambda_{off} \rightarrow \lambda_{on}$. We tried to place λ_{off} away from wings of the H_2 instrument spectral profile for λ_{on} and at positions away from telluric OH lines (see Table 5.2). In order to subtract background and telluric OH line emission, we also chopped the secondary mirror to $\Delta\alpha = +16'$ or $-16'$ at 0.25 Hz in H-band and 0.5 Hz in K-band in both the scanning mode and the frequency switching mode.

For flux calibration, we measured HR 1713 (B8I, $m_K = +0.18$ mag) in 1994 December and HR 8728 (A3V, $m_H = +1.03$ mag and $m_K = +1.00$ mag) in 1995 October. H_2 (1,0) S(1) intensities measured at the same positions in 1994 December and 1995 October agree to within the errors. The absolute flux calibration is accurate to ± 20 %.

5.2.2 CO $J = 1 - 0$ Emission Line

We[4] observed CO $J = 1 \rightarrow 0$ line in 1995 December at the SEST[5] located on La Silla in Chile. The beam size (FWHM) of the SEST is $45''$, and the main beam efficiency is 0.7. The CO intensities presented in this paper are the main beam brightness temperatures, T_R^* (or the atmosphere-corrected antenna temperatures, T_A^*, divided by the main beam efficiency). We used frequency switching to gain a factor of 2 in observing time and to avoid possible emission from reference positions. Since this method can leave residual ripples in the spectra, the detection limit for weak signals is determined by the ripple. For some positions, we complemented the frequency switched data with beam switched data with a reference beam about $12'$ away in AZ. For example, in the 30 Dor $(0, -6')$ region, it turned out to be impossible to use the frequency switched data.

We mapped CO $J = 1 \rightarrow 0$ spectra around positions where we detected H_2 emission and where the CO emission was below the lowest contour level (6 K km s^{-1}) of previously published CO maps (Booth 1993; Johansson et al. 1994). The CO maps are fully sampled on $20''$ grids within each $81''$ H_2 beam. The typical 1σ statistical uncertainty of the intensity in a single $45''$ beam, $I = \int T_R^* dv$, integrated over a velocity range of 15 km s^{-1}, is 0.2 K km s^{-1}.

5.3 Results

In low metallicity objects, the low dust abundance allows far-UV photons to penetrate for long distances beyond the H II/H boundary. The transparency to UV photons could potentially lead to substantial regions of neutral gas

---

[4] L. E. B. Johansson observed the Magellanic Clouds in the CO $J = 1 \rightarrow 0$ line.

[5] The Swedish-ESO Submillimeter Telescope, SEST, is operated jointly by ESO and the Swedish National Facility for Radio Astronomy, Onsala Space Observatory at Chalmers University of Technology.

where far-UV photons have dissociated CO but where self shielding may permit hydrogen to be primarily in the form of H_2. The greater extent of the [C II] 158 μm emission from the N159/N160 complex makes such a possibility seem reasonable in the LMC. Near-IR H_2 emission in response to far-UV radiation provides a direct test for the presence of molecular gas near cloud boundaries, albeit with no direct information about column density or total abundance.

We selected observing targets in regions of the LMC where high spatial resolution ($\sim 1'$) [C II] maps and CO $J = 1 \rightarrow 0$ maps existed, and in regions of the SMC where CO $J = 1 \rightarrow 0$ had been mapped [6] (Rubio et al. 1993; Booth 1993; Johansson et al. 1994; Poglitsch et al. 1995; Israel et al. 1996). We list the observed sources and their reference $(0,0)$ positions in Table 5.3.

5.3.1 H_2, CO, [C II], and far-IR

The H_2 (1,0) S(1) line intensity in the surveyed regions is $< 4 \times 10^{-6}$ erg s^{-1} cm^{-2} sr^{-1}, except in the central regions of 30 Doradus and N160. About 70% of the observed points have detections of (1,0) S(1) line with a significance of 2σ or more. The H_2 (1,0) S(1) intensities are listed in Table 5.4, and the H_2 (2,1) S(1) and (5,3) O(3) intensities in Table 5.5. Reddening toward the stars in the LMC has been measured using $(U-B)$ and $(B-V)$ colors. The Galactic foreground extinction, A_V, toward the LMC is 0.23 ± 0.07 mag (Greve, van Genderen, & Laval 1990; Lee 1991). Applying $A_K = 0.112A_V$ (Rieke & Lebofsky 1985), we get the foreground A_K of ~ 0.03 mag, which is negligible. The local molecular clouds in the LMC extinct the H_2 emission from the back sides of the clouds, if the clouds are not overlapped along the line-of-sight. We may estimate A_V of the molecular cloud itself, using the CO $J = 1 \rightarrow 0$ intensity and the CO-to-H_2 conversion factor (Cohen et al. 1988). In this case,

---

[6]After our observations, we gained access to [C II] maps in parts of the SMC (Israel & Maloney 1993). Their mapped positions unfortunately do not coincide with the positions where we took the H_2 spectra.

the extinction varies cloud-by-cloud, but we do not know the beam filling factor of the CO observations in the LMC. We discuss the H_2 emission from the back side of the clouds, in Section 5.5.3,

In Table 5.4, we also list the CO $J = 1 \to 0$ and [C II] intensities, convolved to the beam size of the H_2 observations ($\theta_{ED} = 81''$). We assumed that the beam profile of the University of Texas Fabry-Perot Spectrometer is a box function.

The columns for far-IR intensity and dust temperature in Table 5.4 are from the IRAS data processed at IPAC[7] using standard HIRES processing. The HIRES processor provides spatial resolution enhanced IRAS images through an implementation of the Maximum Correlation Method algorithm (Aumann, Fowler, & Melnyk 1990). The FWHM sizes are $1.'0 - 1.'6$ for the 60 μm beam and $1.'6 - 2.'4$ for the 100 μm beam. We calculate the integrated fir-IR intensity using the approximation of Helou et al. (1988):

$$I_{FIR} = 1.26 \times 10^{-5} \ (2.58 \ I_{60\mu m} + I_{100\mu m}) \ , \qquad (5.1)$$

where $I_{60\mu m}$ and $I_{100\mu m}$ are in units of MJy/sr and I_{FIR} in $\mathrm{ergs \, s^{-1} \, cm^{-2} \, sr^{-1}}$. We deduce the dust temperature, T_{dust}, from the ratio of 60 μm to 100 μm intensity:

$$\frac{I_{60\mu m}}{I_{100\mu m}} = \left(\frac{\nu_{60\mu m}}{\nu_{100\mu m}} \right)^4 \frac{\exp(h\nu_{100\mu m}/kT_{dust}) - 1}{\exp(h\nu_{60\mu m}/kT_{dust}) - 1} \ , \qquad (5.2)$$

where h is the Planck's constant, k is the Boltzmann's constant, and ν is the frequency in units of Hz. In the above equation, we assumed that the 60 μm emission is dominated not by small ($D \simeq 5$ nm), thermally-spiking, grains but by large grains in steady state temperatures (Draine & Lee 1984), and that the dust emissivity (Q_ν) is proportional to ν^n where $n = 1$.

---

[7]IPAC is funded by NASA as part of the IRAS extended mission program under contract to JPL.

5.3.2 H$_2$ Results

SMC

In the SMC, we detected H$_2$ (1,0) S(1) emission, with $S/N > 2$, near IRAS sources in the SMC-B1, SMC-B2, and LIRS 36 regions. At supernova remnants, e.g., SMC-B2 $(+0\rlap{.}'4, -3\rlap{.}'3)$ and LIRS 36 $(-3', 0)$, however, we did not detect H$_2$ emission down to a level of $1\sigma \simeq 2 \times 10^{-6}$ ergs s^{-1} cm^{-2} sr^{-1}.

LMC: 30 Doradus

Figure 5.3 shows the far-IR, CO $J = 1 \to 0$, and H$_2$ (1,0) S(1), intensity maps of the 30 Doradus region. At the 30 Doradus $(0,0)$ point, our 81$''$ beam measured that $I_{H_2} = 1.1 \times 10^{-5}$ ergs s^{-1} cm^{-2} sr^{-1} (hereafter, I_{H_2} denotes the intensity of the H$_2$ (1,0) S(1) line). Poglitsch et al. (1995), using their imaging NIR-spectrometer FAST, observed intense H$_2$ (1,0) S(1) emission around the central cluster R136 and showed that the H$_2$ source appears highly fragmented ($< 5''$ or 1 pc scale) with a typical intensity of $\sim 1.6 \times 10^{-4}$ ergs s^{-1} cm^{-2} sr^{-1}.

Our observations show that the H$_2$ emission in 30 Doradus is very extended, (> 20 pc). One and a half arc minutes from the $(0,0)$ position, the H$_2$ (1,0) S(1) intensity is only a factor of two lower than at the peak. We also detected faint H$_2$ (1,0) S(1) emission at $(0, -6')$, $I_{H_2} = 1.6 \times 10^{-6}$ ergs s^{-1} cm^{-2} sr^{-1}, where CO $J = 1 \to 0$ emission had not been detected during the survey of the ESO-SEST Key Program (Booth 1993).

LMC: N159/160

The N159/N160 H II complexes are 40$'$ south of 30 Doradus. The [C II] line distribution (Israel et al. 1996) and the far-IR continuum distribution (left map in Figure 5.4) show that the far-UV fields are strong both near N159 and N160. On the other hand, the CO intensity around N159 is more than four times stronger than that around N160.

H$_2$ (1,0) S(1) line had been detected at "N159 Blob" (a compact H II source with a size of $8'' \times 6''$, Heydari-Malayeri & Testor 1985) by several groups. In Table 5.6, we compare the previous data with our new results. The flux increases as the beam size increases, suggesting that the emission region is more extended than $\sim 20''$. In our H$_2$ survey, we observed very extended ($> 5'$ or 70 pc) H$_2$ (1,0) S(1) emission from the N159/N160 H II complex (see the right map in Figure 5.4). In the N159 region, we detected H$_2$ emission where the CO cloud complex is bright and extended (see Figure 1 in Johansson et al. 1994). In the N160 region, however, we also detected the H$_2$ emission beyond the lowest CO $J = 1 \rightarrow 0$ contour level (6 K km s^{-1}, size of $1' \times 3'$) in the map by Johansson et al. (1994). In spite of the weak or absent CO emission in the N160 region, the H$_2$ observations indicate that the size of the molecular cloud complex is as big as that in the N159 region.

5.3.3 CO $J = 1 \rightarrow 0$

From our H$_2$ results, we found that the H$_2$ molecules are widespread in pho-todissociated gas in the Magellanic Clouds, in spite of the low dust extinction and the strong far-UV fields ($I_{UV} > 10^2$, see Section 5.4.2). The next question was whether the CO molecules, especially in the outer regions of 30 Do-radus and N160, are completely dissociated or not. We observed these regions again in CO $J = 1 \rightarrow 0$ line (see Section 5.2.2) with higher sensitivity ($\sigma \simeq 0.2$ K km s^{-1}) than the previous observations (Johansson et at. 1994) whose lowest contour level was 6 K km s^{-1}.

We made a fully sampled CO map inside the UT FPS beam at $(0, -6')$ in the 30 Doradus region, and detected CO $J = 1 \rightarrow 0$ at a level of 0.5 K km s^{-1} (see Figure 5.3). We also made CO maps in the outer regions of N160 where the previous CO $J = 1 \rightarrow 0$ map did not show any CO emission higher than 6 K km s^{-1}. We sampled some positions in N159 to confirm the flux calibration

of the new observations by comparing with the previous observations. Figure 5.5 and the middle map in Figure 5.4 show the new CO $J = 1 \rightarrow 0$ results. We plot the contours at logarithmic intervals to emphasize the edges of the molecular cloud complexes; note the dense contour lines on the northwestern side and on the western side of the N160 complex. The CO $J = 1 \rightarrow 0$ emission regions cover the H_2 emission regions except the $(-2\overset{.}{.}5, +7')$ and the $(-2', +10')$ positions where the CO cloud complex fills $50 - 70$ % of the H_2 beams. CO emission is detected in each beam where H_2 was detected.

5.3.4 H_2 Excitation Mechanism

In Table 5.5, we list the observed H_2 line ratios of (2,1) S(1)/(1,0) S(1) and (5,3) O(3)/(1,0) S(1) in the Magellanic Clouds. Observations of the H_2 lines in the archetypal shocked regions, e.g., Orion BN-KL, HH 7, and the supernova remnant IC 443, show that the H_2 ratios of (2,1) S(1)/(1,0) S(1) are almost constant ~ 0.08 or $T_{exc} \simeq 2 \times 10^3$ K (Burton et al. 1989; Richter, Graham, & Wright 1995). Assuming that the excited levels are in LTE and $T_{exc} = 2000$ K, the H_2 ratio of (5,3) O(3)/(1,0) S(1) is only $\sim 9 \times 10^{-5}$. The observed H_2 line ratios, which are much higher than those in the shock models, exclude the possibility of shock-excitation as being responsible for the emission we observed.

Molecular hydrogen in PDRs absorbs $91.2 - 110.8$ nm photons in the $B^1\Sigma_u^+ - X^1\Sigma_g^+$ Lyman and $C^1\Pi_u - X^1\Sigma_g^+$ Werner bands. About 10 % of the electronically excited molecules are dissociated. The remaining 90% of the excitations result in populations of various ro-vibration levels of the ground electronic state. If $n(H_2) < 5 \times 10^4 \text{cm}^{-3}$, the relative line intensities arising in UV-excited H_2 are insensitive to density or to UV field strength (Black & van Dishoeck 1987). In this pure-fluorescent transition case, the H_2 ratio of (2,1) S(1)/(1,0) S(1) is 0.56 and (5,3) O(3)/(1,0) S(1) is 0.38. At densities $\geq 5 \times 10^4 \text{cm}^{-3}$, the collisional de-excitation of UV-pumped H_2 becomes important

in the ro-vibrational level populations. If the PDR boundaries become sufficiently warm ($T > 1000$ K) and dense, collisional excitation thermalizes the low vibrational ($v \leq 2$) level populations (Sternberg & Dalgarno 1989; Luhman et al. 1997).

As we list in Table 5.5, the detections of H_2 (5,3) O(3) line in the Magellanic Clouds verify the UV-excitation of H_2. The observed H_2 line ratios from the N160 region are those expected for pure-fluorescence. The ratios toward other regions show that the H_2 ro-vibration levels are affected somewhat by collisions. In 30 Doradus, the peak H_2 (1,0) S(1) intensity is 2.3×10^{-4} ergs s^{-1} cm^{-2} sr^{-1} (Poglitsch et al. 1995) which is brighter than the maximum predicted by our PDR models ($I_{H_2} \leq 9.6 \times 10^{-5}$ ergs s^{-1} cm^{-2} sr^{-1}, see Figure 5.12) because of the collisional excitation of H_2 in clouds subjected to intense far-UV fields.

5.4   Comparing with Galactic Clouds

We compare the H_2 (1,0) S(1), [C II] 158 μm, CO $J = 1 \rightarrow 0$, and far-IR emission from the clouds in the Magellanic Clouds (see Table 5.4) to the emission from star forming clouds in Orion and NGC 2024 (see Table 5.7). In the LMC, we select positions where complete H_2, [C II], and CO data sets exist: 5 positions in the 30 Doradus region, 4 positions in the N159 region, and 8 positions in the N160 region. In the SMC, we use 4 positions with only CO and H_2 data sets, because [C II] data are not available.

5.4.1   Data from NGC 2024 and Orion A Star Formation Regions

For the Galactic cloud data, we make use of the published H_2 (1,0) S(1), [C II] 158 μm and CO $J = 1 \rightarrow 0$ data in Schloerb & Loren (1982), Stacey et al. (1993), Jaffe et al. (1994), Luhman et al. (1994), Luhman & Jaffe (1996), and Luhman et al. (1997). The far-IR data are from the HIRES processed IRAS

data (see Section 5.3.1). In the Orion molecular cloud, Stacey et al. (1993) made two [C II] strip maps in Right Ascension, both of which passes close to the CO $J = 1 \rightarrow 0$ peak. The [C II] flux along the strips was "bootstrapped", integrated by assuming zero flux at the ends of the cut and summing the chopped differences. The data from *cut 1* (observed west to east) and *cut 2* (observed east to west) are not in complete agreement; therefore, we take only those data with:

$$2 \frac{\mid I_{cut1} - I_{cut2} \mid}{I_{cut1} + I_{cut2}} < 0.4 \ . \tag{5.3}$$

We also exclude positions where the IRAS data are saturated, i.e., $I_{60\mu m} >$ 1500 MJy/sr, and where the H_2 ro-vibrational level populations begin to show effects of collisional de-excitation ((6,4) Q(1)/(1,0) S(1) < 0.15, see Table 2 in Luhman & Jaffe 1996). Some positions were not observed in the H_2 (6,4) Q(1) line, but we still include the data in our list (see the discussion in Section 5.5.5). In Table 5.7, we list the compiled data sets in the Galactic Clouds: 4 positions from the Orion A molecular cloud (hereafter "Orion"), and 11 positions from the cloud in the NGC 2024 H II region (hereafter "NGC 2024").

In Figure 5.6, we examine our collected data sets from 15 positions in the Galactic clouds. Jaffe et al. (1994) presented CO $J = 1 \rightarrow 0$ and [C II] data from NGC 2024, and showed that the different parts of the source have very different distributions on a I_{CII} versus I_{CO} plot. The left plot in Figure 5.6 shows the distinction between *the cloud proper zone* ($\Delta RA > -10'$ with respect to NGC 2024 IRS 1, shown as open circles) and *the western edge zone* ($\Delta RA < -10'$, shown as open triangles) in NGC 2024. Data from the cloud proper zone agrees with the PDR models of Wolfire et al. (1989), while many of the I_{CII}/I_{CO} ratios toward the western edge zone are much higher than any of the model ratios. Jaffe et al. (1994) interpreted the western edge zone results as implying that the mean column density of clumps decreases to the west. The right plot in Figure 5.6 shows the location in the $I_{CII} - I_{CO}$ space

of the data sets in Table 5.8, which will be used to compare with those from the Magellanic Clouds.

5.4.2 Beam Filling Factor of far-IR Data

A beam size of $\sim 1'$ corresponds to ~ 15 pc at the distance of the LMC ($d = 50.1$ kpc, Westerlund 1990), while the same beam size corresponds to ~ 0.12 pc at the Orion ($d = 415$ pc, Anthony-Twarog 1982). The molecular clouds in Galactic giant molecular cloud (GMC) complexes, especially in UV influenced regions, are clumpy on a size scale of ~ 1 pc (Burton, Hollenbach, & Tielens 1990; Jaffe et al. 1994), comparable to or larger than the Orion beam but very much smaller than the beams in the LMC. Since the measured intensity is a beam average over any source structure, we have to correct for the effects of different beam filling factors in order to directly compare the emitted intensities from the LMC with those from the Galactic clouds.

I_{UV} *versus* I_{FIR}

The intensity of the interstellar far-UV radiation field is usually expressed in terms of the scaling factor I_{UV}, the mean intensity in the solar neighborhood (Draine 1978; also see the footnote 2 in Black & van Dishoeck 1987):

$$I_\nu = \frac{h\nu}{4\pi} \left(\frac{1.068350 \times 10^{-4}}{\lambda} - \frac{0.01719258}{\lambda^2} + \frac{0.6853491}{\lambda^3} \right) , \qquad (5.4)$$

where I_ν is in units of $\mathrm{ergs\,s^{-1}\,cm^{-2}\,sr^{-1}\,Hz^{-1}}$, and λ is in units of nm. The critical part of the UV range for H_2 fluorescence, C ionization, and CO dissociation is $91.2 < \lambda < 113$ nm (Black & van Dishoeck 1987; van Dishoeck & Black 1988). The intensity of the $I_{UV} = 1$ field integrated over $91.2 < \lambda < 113$ nm is 3.71×10^{-5} $\mathrm{ergs\,s^{-1}\,cm^{-2}\,sr^{-1}}$. Note that some authors (e.g., Tielens & Hollenbach 1985) use the Habing field (Habing 1968), and use a symbol, $G_\circ$ $= 1.3 \times 10^{-4}$ $\mathrm{ergs\,s^{-1}\,cm^{-2}\,sr^{-1}}$, for the integrated intensity between $6 < h\nu < 13.6$ eV or $91.2 < \lambda < 206.6$ nm. The corresponding intensity of the Draine

field integrated over the same band as the $G_{\circ}$ is 2.13×10^{-4} ergs s^{-1} cm^{-2} sr^{-1} (for the detailed comparison between the Draine field and the Habing field, see Draine & Bertoldi 1996).

Most of the far-UV energy is absorbed by grains and reradiated in far-IR:

$$I_{FIR} = 2 \times (2.13 \times 10^{-4}) \, I_{UV} \; \text{ergs s}^{-1} \, \text{cm}^{-2} \, \text{sr}^{-1}, \tag{5.5}$$

where the factor of 2 accounts for incident radiation at longer wavelength, $I_{\nu}(\lambda > 206.6 \text{ nm})$ (Wolfire, Hollenbach, & Tielens 1989).

I_{FIR} versus T_{dust}

We can use the far-IR emission to normalize the various line intensities to compensate for beam filling factor effects. Before we do so, however, we need to understand how the far-IR emission arises. In Figure 5.7, we plot I_{FIR} versus T_{dust} for the Galactic star forming cloud positions and the Magellanic Clouds positions in our sample. We deduce I_{FIR} from Equation 5.1, and T_{dust} from Equation 5.2. Assuming that the dust is heated by an external far-UV field, we can approximate the results of PDR models:

$$T_{dust} = 13.5 \left(I_{UV} \frac{T_{eff}}{3 \times 10^4} \right)^{1/5} \text{ K} \tag{5.6}$$

(Hollenbach, Takahashi, & Tielens 1991; Spaans et al. 1994). Assuming T_{eff} = 3×10^4 K, the expected relation between T_{dust} and I_{FIR} is:

$$\log I_{FIR} = -9.02 + 5 \log T_{dust}, \tag{5.7}$$

which is shown as a dotted line in Figure 5.7.

The T_{dust} and I_{FIR} distributions of the Orion and NGC 2024 data agree with the model in Equation 5.7. I_{FIR} is proportional to the beam filling factor, while T_{dust}, which was deduced from the ratio of $I_{60\mu m}/I_{100\mu m}$, is independent of the beam filling factor. With a beam size of $\sim 1'$ (or ~ 0.12 pc at $d \simeq 415$

pc; Anthony-Twarog 1982), the projected beam filling factor for the clouds in Orion and NGC 2024 is ~ 1, which explains the agreement between the observed $T_{dust} - I_{FIR}$ relation and the model. If we assume that the dust size distribution is independent of metallicity and that the clouds are optically thick in the far-UV, the T_{dust}-I_{FIR} relation should be independent of the dust abundance. For the Magellanic Clouds, the observed I_{FIR} values are an order of magnitude weaker than the values predicted by the $T_{dust} - I_{FIR}$ relation. This difference implies a beam filling factor in the Magellanic Clouds of ~ 0.1.

5.4.3 Line Intensities Divided by I_{FIR}

The line and continuum emission we describe here arises in the layers of molecular clouds where UV photons influence the chemistry and the physical conditions. Various parameters affect the emergent intensity:

$$
\begin{aligned}
I_i &= \eta \, \epsilon_i \, f_i(n_H, I_{UV}, \delta v_D, Z), \; i = \mathrm{CO}, \mathrm{C\,II}, \mathrm{H_2} \;, & (5.8) \\
I_{FIR} &= \eta \, \epsilon_{FIR} \, 4.26 \times 10^{-4} \, I_{UV} \;,
\end{aligned}
$$

where I_i is the *observed* CO $J = 1 \rightarrow 0$, [C II] 158 μm, or H$_2$ (1,0) S(1) emission line intensity, and I_{FIR} is the *observed* far-IR continuum intensity in units of $\mathrm{ergs\,s^{-1}\,cm^{-2}\,sr^{-1}}$. f_i is the combined intensity arising from the front and back sides of a plane-parallel model cloud which fills the beam. The front and back surfaces of the cloud are exposed to external far-UV radiation, and are perpendicular to the line-of-sight. f_i depends on the hydrogen number density, $n_H = n(\mathrm{H}) + 2n(\mathrm{H_2})$, where $n(\mathrm{H})$ and $n(\mathrm{H_2})$ are the atomic and molecular hydrogen density, respectively; the far-UV field strength, I_{UV}; the Doppler velocity dispersion, δv_D (or half-width at 1/e point); and the metal abundance, Z.

We define the beam filling factor, η, as the fraction of the observed beam area filled by a single cloud (not an ensemble of clouds), using the outermost

edge as the cloud boundary (or the boundary between H II and H I regions):

$$\eta = \left(\frac{2R_{cloud}}{d\ \theta_{ED}}\right)^2 \leq 1 \qquad (5.9)$$

where R_{cloud} is the radius of the cloud to the outer (H II/H) boundary, d is the distance to the cloud, and θ_{ED} is the diameter of the telescope equivalent disk in radians. η is same for all types of emission in the same cloud. In order to simplify model simulations in Section 5.5, we assume that only one cloud is in the telescope beam, the telescope has a box-function beam profile, and the telescope beam area is always larger than the cloud size, i.e., $d\ \theta_{ED} \geq 2R_{cloud}$.

It may be more realistic to consider spherical rather than planar clouds. In case of a spherical cloud with an external far-UV field whose intensity is uniform on the surface of the cloud, the far-IR, [C II], and H_2 emission arise in the outer shells of the cloud, while the CO $J = 1 \rightarrow 0$ emission arises from the surface of the CO core inside the cloud. We use a "spherical geometry parameter", ϵ_i, in Equation 5.8 to simulate the *observed* intensity of a spherical cloud. The spherical geometry parameter accounts for limb-brightening and for the size differences between the CO, [C II], and H_2 emission regions in a given spherical cloud.

When examining our spherical model clouds, we can eliminate the beam filling factor, η, by dividing I_i by I_{FIR}:

$$\frac{I_i}{I_{FIR}} = \frac{\epsilon_i}{\epsilon_{FIR}} \frac{f_i(n_H, I_{UV}, \delta v_D, Z)}{2 \times 4.26 \times 10^{-4}\ I_{UV}} \ . \qquad (5.10)$$

We will therefore divide the observed intensities by the far-IR intensity at each position as a means of removing distance-related beam filling factor effects in our subsequent analysis of the data from the Galaxy and the Magellanic Clouds.

5.4.4   Relationship between I_{CO}, I_{CII}, and I_{H2}

Table 5.8 shows the average ratios between the observed H_2 (1,0) S(1), CO $J = 1 \rightarrow 0$, and C II intensities, and the standard deviations of the ratio distri-

butions in the Galactic clouds and in the Magellanic Clouds.

In Figures 5.8, 5.9, and 5.10, and we plot I_{H_2}/I_{FIR} versus I_{CII}/I_{FIR}, I_{CII}/I_{FIR} versus I_{CO}/I_{FIR}, and I_{H_2}/I_{FIR} versus I_{CO}/I_{FIR}, for the Galactic clouds and for the clouds in the Magellanic Clouds. From these figures and Table 5.8, the line ratios of $\log(I_{H_2}/C\,\text{II})$ between the Galaxy and the Magellanic Clouds are in good agreement, while the ratios of $\log(I_{CII}/I_{CO})$ and $\log(I_{H_2}/I_{CO})$ in the Magellanic Clouds are higher than those in the Galaxy. In Section 5.5, we will discuss our PDR models and compare the observed data with PDR models with various input parameters.

5.5 Models

Using plane-parallel codes, the metallicity dependence of PDR structure and of emergent line intensities has been calculated and discussed by several authors (Maloney & Black 1988; van Dishoeck & Black 1988; Wolfire, Hollenbach, & Tielens 1989; Maloney & Wolfire 1997). The emergent intensities of the H_2 (1,0) S(1), [C II], and CO $J = 1 \rightarrow 0$ lines from PDRs depend on n_H, I_{UV}, δv_D, and Z (see Section 5.4.3). As long as the CO $J = 1 \rightarrow 0$ line is optically thick, the resulting intensities of CO, [C II], and H_2 (1,0) S(1) lines are not very sensitive to the metallicity. The results can be explained with a simplified analysis. In the outer part of the PDR, gas-phase carbon is in the form of C^+. When the metallicity is lowered, the number density of C^+ ions drops, but the far-UV photons penetrate deeper into the clouds because of the low dust-to-gas ratio. Thus, the column density of C^+ in the PDR is almost independent of the metallicity. The [C II] line is optically thin, and the intensity is proportional to the column density of C^+. On the other hand, the CO $J = 1 \rightarrow 0$ intensity does not depend on the CO column density, because the line is optically thick and arises on the surface of the CO region inside the cloud. Therefore, the CO $J = 1 \rightarrow 0$ intensity does not depend on the metallicity. We will discuss the

metallicity dependence of H_2 in Sections 5.5.2 and 5.5.3.

As we discussed in Section 5.4.3, spherical geometry effects (denoted as ϵ_i) account for: (1) limb-brightening; and (2) the size differences between the outer shells from which far-IR, [C II], and H_2 (1,0) S(1) emissions arise and the inner CO core from which CO $J = 1 \rightarrow 0$ emission arises. The depths from the cloud surface to the C^+/C transition layer and to the H/H_2 transition layer are about inversely proportional to the dust abundance, so the metal and dust abundance is a more important parameter in spherical-shell PDRs than in plane-parallel models. Störzer, Stutzki, & Sternberg (1996) and Mochizuki (1996) modeled a PDR on the surface of a spherical cloud with Galactic metallicity. In this Section, we present our own models of spherical-shell PDRs and calculate the emergent line intensities for a range of densities, UV fields, and metallicities.

5.5.1 Codes

We first ran the plane-parallel PDR code of van Dishoeck and Black (van Dishoeck & Black 1986; Black & van Dishoeck 1987; van Dishoeck & Black 1988) with a range of densities ($n_H = 5 \times 10^2$, 5×10^3, 5×10^4 cm^{-3}), UV fields ($I_{UV} = 10$, 10^2, 10^3, 10^4), and metallicities (for the Galaxy and the LMC). In this code, one side of the model cloud is exposed to UV radiation, and the cloud is divided into 200 slabs, each of which is in chemical steady state. Since the code does not include inelastic collisions of H_2, the ro-vibrational level populations of H_2 are not correct at $n_H \geq 5 \times 10^4$ cm^{-3}. The PDR code calculates the gas temperature and chemical abundances in each slab. In Table 5.9, we list input parameters for the code.

We use the output of the plane-parallel code to assign chemical abundances and kinetic temperatures to the spherical shells of the cloud used in the radiative transfer model. We map the temperatures and abundances derived

at each distance from the H II/H I interface by the plane-parallel model into the spherical radiation transfer model, ignoring any changes in the chemistry or thermal balance due to the difference in geometry. We use the Monte Carlo code of Choi et al. (1995; hereafter MC) to calculate the level populations of the atoms and molecules. The MC code simulates photons in a one-dimensional (spherical) cloud, and adjusts the level populations according to the result of simulations until the populations converge. We assume a purely turbulent velocity field with a Doppler velocity dispersion of 1 km s^{-1} (δv_D or half-width at $1/e$ point) with no systematic motion. Since the MC calculation only includes 40 slabs, we smoothed the 200 slab model in such a way as to retain high resolution at the transition regions (Li 1997).

We use the output of MC to calculate emission line profiles using the Virtual Telescope code (Choi et al. 1995; hereafter VT). The VT code convolves the integrated emission from each spherical shell along the line-of-sight with a virtual telescope beam profile to simulate observations.

5.5.2   Effect of H_2 Self-Shielding

Inside neutral clouds, the external far-UV field is attenuated by dust absorption, and by C and H_2 absorption. CO absorption of far-UV is negligible in the outer part of the cloud because most of the carbon is ionized. H_2 can survive in the outer parts of the cloud, either as a result of self shielding or as a result of shielding by dust. We can analyze the conditions under which H_2 self-shielding from far-UV photons is dominant over shielding by dust (adapted from Burton, Hollenbach, & Tielens 1990). Within a plane-parallel cloud, the H_2 formation rate, $F(x)$, at depth x measured from the surface of the cloud toward the center is

$$F(x) = n(\text{H}, x) \, n_H \, q \, \Re \, , \tag{5.11}$$

where n_H is the hydrogen number density, $n_H = n(\mathrm{H}, x) + 2n(\mathrm{H_2}, x)$, assumed to be constant over the cloud; $n(\mathrm{H}, x)$ and $n(\mathrm{H_2}, x)$ are number densities, at x, of H atoms and $\mathrm{H_2}$ molecules respectively; $\Re$ is the $\mathrm{H_2}$ formation rate coefficient for the Galactic dust abundance; q is the dust abundance corrector incorporated in $\Re$, and normalized to the Galactic value, i.e., $q^{GAL} = 1$. $\Re$ is a slowly varying function of the gas temperature ($\Re \propto T^{1/2}$), so we take an average value (3×10^{-17} cm^{-3} s^{-1}, Burton, Hollenbach, & Tielens 1990) for this analysis. If we assume that the dust optical depth is negligible and the $\mathrm{H_2}$ absorption is governed by the square root portion of the curve of growth (Jura 1974) the far-UV field is attenuated by $N(\mathrm{H_2}, x)^{1/2}$, where

$$N(\mathrm{H_2}, x) = \int_0^x n(\mathrm{H_2}, x) \, dx \ . \qquad (5.12)$$

The $\mathrm{H_2}$ destruction rate, $D(x)$, at depth x is

$$D(x) = \frac{I_{UV} \, I_\circ, \beta}{N(\mathrm{H_2}, x)^{1/2}} \, n(\mathrm{H_2}, x) \ , \qquad (5.13)$$

where $I_\circ$ is the unshielded dissociation rate of $\mathrm{H_2}$ at $I_{UV} = 1$ (7.5×10^{-11} s^{-1}, Black & van Dishoeck 1987); and β is the self-shielding parameter (4.2×10^5 cm^{-1}, Jura 1974). We can integrate the steady state equation, $F(x) = D(x)$, over x:

$$n_H \, q \, \Re \int_0^x n(\mathrm{H}, x) \, dx = I_{UV} \, I_\circ \, \beta \int_0^x \frac{n(\mathrm{H_2}, x)}{N(\mathrm{H_2}, x)^{1/2}} \, dx \ . \qquad (5.14)$$

By substituting Equation 5.12 into the above equation, we get:

$$n_H \, q \, \Re \, N(\mathrm{H}, x) = 2 \, I_{UV} \, I_\circ \, \beta \, N(\mathrm{H_2}, x)^{1/2} \ . \qquad (5.15)$$

$\mathrm{H_2}$ self-shielding is more important than shielding of far-UV photons by dust, when, at the point $x_\circ$ where the molecular hydrogen column density becomes equal to the atomic hydrogen column density,

$$N(\mathrm{H}, x_\circ) = 2N(\mathrm{H_2}, x_\circ) \ , \qquad (5.16)$$

the far-UV field attenuation by dust is still negligible,

$$\tau_{dust}(x_\circ) \leq \frac{1}{2} \; .$$ (5.17)

$\tau_{dust}(x)$ is the optical depth of dust at $\lambda = 100$ nm (Bohlin et al. 1983; Black & van Dishoeck 1987):

$$\tau_{dust}(x) \;\simeq\; 3.0 A_V(x) \;, \text{and}$$ (5.18)
$$A_V(x) \;=\; 6.29 \times 10^{-22} \rho_{dust} N_H(x) \;,$$

where ρ_{dust} is the dust-to-gas ratio normalized to the Galactic value (see Table 9), and $N_H(x)$ is the hydrogen column density, $N_H(x) = N(\text{H}, x) + 2N(\text{H}_2, x)$. Substituting Equation 5.16 into Equation 5.15, we get:

$$N_H(x_\circ)^{1/2} \;=\; 2 \frac{\beta \, I_\circ}{\Re} \frac{I_{UV}}{q \, n_H}$$
$$\simeq\; 2.1 \times 10^{12} \frac{I_{UV}}{q \, n_H} \; .$$ (5.19)

From Equations 5.17, 5.18, and 5.19, we derive the conditions under which the H_2 self-shielding is dominant over shielding by dust:

$$\frac{n_H}{I_{UV}} \geq 1.3 \times 10^2 \, \rho_{dust}^{-1/2} \; ,$$ (5.20)

where we assume that the optical absorptivity and the H_2 forming ability of the dust, per unit H atom, vary in the same way with dust abundance: $q = \rho_{dust}$. In Figure 5.11, we plot the linear sizes of the C^+ region (X_{C+}) and the H_2^* region $(X_{H_2^*})$ from the PDR model results: X_{C+} and $X_{H_2^*}$ are the distances from the surface of the cloud to the inner edges of the C^+ region and of the H_2^* region respectively.

The plot of $X_{H_2^*}$ in Figure 5.11 shows how H_2 self-shielding affects the depth of the H_2^* region from the surface of the cloud. Based on Equation 5.20, we divide the $(I_{UV}, n_H, X_{H_2^*})$ space into the dust absorption dominant region and the H_2 self-shielding dominant region (shown as dotted lines). We can

predict the behavior of $X_{H_2^*}$ as a function of I_{UV}, n_H, and ρ_{dust}, using the relations we derived in this section. When dust absorption is more important than H_2 self-shielding, the far-UV field at the inner edge of the H_2^* zone is determined by τ_{dust} and is constant even when the external far-UV field, I_{UV}, varies:

$$I_{UV} \exp(-\tau_{dust}) = C \ , \tag{5.21}$$

where C is a constant. Substituting Equation 5.18 into the above equation gives that

$$N_H(X_{H_2^*}) \simeq 1.22 \times 10^{21} \, \frac{\log I_{UV} - \log C}{\rho_{dust}} \ , \tag{5.22}$$

where $N_H(X_{H_2^*})$ is the hydrogen column density at $X_{H_2^*}$. In other words, if we increase I_{UV} by an order of magnitude, $N_H(X_{H_2^*})$ is added by only 1.22×10^{21} cm^{-2}.

When H_2 self-shielding is dominant, from Equation 5.19,

$$\log N_H(X_{H_2^*}) \simeq 24.6 + 2 \log \left(\frac{I_{UV}}{q \, n_H} \right) \ , \tag{5.23}$$

e.g., if I_{UV} decreases by an order of magnitude, $N_H(X_{H_2^*})$ decreases by two orders of magnitude. The above equation explains, in the H_2 self-shielding dominant condition, why the depth of the H_2^* shell decreases rapidly as I_{UV} decreases or as n_H increases (see Figure 5.11).

In the LMC, $(\rho_{dust}^{LMC})^{-1/2} \simeq 2.2$ (see Equation 5.20), and the dotted line is shifted toward lower I_{UV} by only a factor of 2.2. Even in the case of the SMC, $(\rho_{dust}^{SMC})^{-1/2} \simeq 3.2$. Variations in metal abundance, therefore, do not significantly affect the H_2 self-shielding criterion.

5.5.3 Emission Intensities without Spherical Geometry Effects, ϵ

We first ran the MC and VT codes to obtain results where the spherical natures of the model clouds, e.g., limb-brightening and the geometrical size differences

(see Section 5.4.3), are not important, by setting the virtual telescope beam size (θ_D) much smaller than the cloud size ($2R_{cloud}$). This permits us, in effect, to obtain the line intensities from a plane-parallel cloud with a finite thickness whose front and back surfaces are exposed to external far-UV radiation. The surfaces of the cloud are perpendicular to the line-of-sight. These models are equivalent to setting $\eta = 1$ and $\epsilon_i = 1$ in Equation 5.8: $I_i = f_i$. The resulting [C II] intensity is from both the front and back surfaces, because the [C II] line emission is nearly optically thin (Stacey et al. 1991). The CO $J = 1 \rightarrow 0$ line is optically thick, so the resulting CO emission is almost entirely from the front surface.

The VT code does not calculate the ro-vibrational lines of H_2. We derive the H_2 (1,0) S(1) emission from the H_2^* column density, $N(H_2^*)$, which results from the plane-parallel PDR model. The electronically excited H_2 energy levels cascade by emitting ro-vibrational lines. Because relative H_2 line ratios are insensitive to n_H and I_{UV}, we can simply use a constant conversion factor between $N(H_2^*)$ and H_2 (1,0) S(1) intensity (Black & van Dishoeck 1987):

$$f_{H_2}^{front} = 2.67 \times 10^{-21} \, N(H_2^*) \text{ ergs s}^{-1} \text{ cm}^{-2} \text{ sr}^{-1} \,, \qquad (5.24)$$

where $f_{H_2}^{front}$ is the intensity from the front surface of the cloud.

While the ro-vibrational lines of H_2 are optically thin, the emission from the back surface, $f_{H_2}^{back}$, is affected by the extinction, A_K, through the cloud itself. Using $A_K = 0.112A_V$ (Rieke & Lebofsky 1985) and Equation 5.18, we estimate the observed intensity from the back surface:

$$\log(f_{H_2}^{back}) = \log(f_{H_2}^{front}) - \frac{\rho_{dust} N_H}{3.5 \times 10^{22} \text{cm}^{-2}} \,. \qquad (5.25)$$

From our CO observations in the LMC (see Section 5.3), the CO $J = 1 \rightarrow 0$ line is optically thick in the observed regions. As we will discuss in Section 5.5.4, the cloud size (in units of hydrogen column density N_H) has a lower

limit to keep the CO molecules from being dissociated completely in intense far-UV field ($I_{UV} > 10^3$). Figure 5.13 shows that $\rho_{dust} N_H$ should be larger than $2 \times 10^{22}\,\mathrm{cm^{-2}}$; therefore,

$$f_{H_2}^{back} < 0.3\, f_{H_2}^{front} \,. \tag{5.26}$$

We will neglect the H_2 emission from the back side of the cloud in the following discussion: $f_{H_2} \simeq f_{H_2}^{front}$. In some cases, there may be a bit of additional flux from the back side which can penetrate through the thinner parts of the cloud.

In Figure 5.12, we plot the [C II], H_2 (1,0) S(1), and CO $J = 1 \to 0$ emission intensities from the PDR code and the MC/VT code for the two sided planar clouds. When dust absorption dominates (Equation 5.20), the H_2 intensity increases as n_H increases. On the other hand, when H_2 self-shielding dominates, the H_2 intensity increases as I_{UV} increases. In the LMC model (the right plot in Figure 5.12), the H_2 intensity is enhanced by a factor of $10^{0.1} - 10^{0.3}$ over the intensity in the Galactic model with the same n_H and I_{UV}. The enhancement is mainly due to the different H_2 self-shielding criteria in the Galactic model and in the LMC model.

5.5.4   Emission Intensities with Spherical Geometry Effects, ϵ

In order to understand the effects of limb-brightening and differences in the physical sizes of the C^+, H_2^*, and CO zones in spherical clouds of varying metallicity, we ran the VT code, setting the virtual telescope beam size (θ_{ED}) to match the cloud size ($2R_{cloud}$). The resulting intensities are equivalent to setting $\eta = 1$ in Equation 5.8: $I_i = \epsilon_i f_i$. In Figure 5.13, we plot the model values of I_{CII}, I_{H_2}, and I_{CO} versus cloud size. In Figures 5.6, 5.9, and 5.10, we overlay the results on the observed data. I_{CII} and I_{CO} are obtained directly from the VT code, and the far-IR continuum emission and I_{H_2} are from Equation 5.8 with ϵ_{FIR} and ϵ_{H_2} derived as follows:

As we discussed in Section 5.4.3, the spherical geometry effects include

both limb-brightening and size differences between the different emission regions in the cloud. The far-IR emission has very low optical depth and the H_2 (1,0) S(1) emission is optically thin. These emission regions arise on the surface of the cloud and fill the telescope beam. We can analyze the spherical geometry effects for these lines by projecting the three dimensional emission shell onto a two dimensional emission disk:

$$
\begin{aligned}
\epsilon_i &= \frac{\int_{R_{cloud}-X_i}^{R_{cloud}} 4\pi R^2 dR}{2\, X_i\, \pi R_{cloud}^2} \\
&= 2 - 2\frac{X_i}{R_{cloud}} + \frac{2}{3}\left(\frac{X_i}{R_{cloud}}\right)^2 \;,
\end{aligned}
\tag{5.27}
$$

where X_i is the depth from the cloud surface to the transition regions, e.g., X_{C+} and $X_{H_2^*}$ which are defined in Section 5.5.2; and R_{cloud} is the radius of the cloud. A different result can be derived for the far-IR emission, if we consider that the incident far-UV energy is conserved as the output far-IR energy (see Equation 5.5):

$$
\begin{aligned}
\epsilon_{FIR} &= \frac{4\pi R_{cloud}^2}{2\,\pi R_{cloud}^2} \\
&= 2\;.
\end{aligned}
\tag{5.28}
$$

We use Equation 5.27 to obtain ϵ_{H_2}, and Equation 5.28 to obtain $\epsilon_{FIR} = 2$.

The CO line arises on the surface of the CO core. Because the external UV radiation provides most of the heating, the gas temperature gradient is positive, $dT/dR > 0$ ($R = 0$ at the cloud center). As we observe an optically thick line, the edge of the projected CO disk has a higher brightness temperature than the center, and we can see this limb-brightening effect. On the other hand, the size of the CO core (R_{CO}) is smaller than the cloud size (R_{cloud}); therefore, we can also see the effect from the size difference. When R_{cloud} is larger than X_{C+}, and I_{CO} is optically thick:

$$
\epsilon_{CO} \simeq \left(\frac{R_{CO}}{R_{cloud}}\right)^2 = \left(1 - \frac{X_{C+}}{R_{cloud}}\right)^2 \;,
\tag{5.29}
$$

where $R_{CO} = R_{cloud} - X_{C+}$. The effect of the change of the CO core size (R_{CO}) is more significant than the limb-brightening effect. Using the above equation, we calculate ϵ_{CO}, and plot $\epsilon_{CO} f_{CO}$ in dash-and-dot lines in Figure 5.13, where f_{CO} from the results in Section 5.5.3, assuming that the C$^+$-to-CO transition is discontinuous. When R_{cloud} decreases and becomes close to X_{C+} (or $R_{CO} \to 0$), ϵ_{CO} decreases rapidly as we see in Equation 5.29. We also plot the CO intensity (by setting $\eta = 1$) resulting from the numerical code in dotted lines in Figure 5.13. As $R_{CO} \to 0$, the resulting I_{CO} decreases less rapidly than that in the dash-and-dot lines, $I_{CO} \propto R_{cloud}^{10}$, because the C$^+$-to-C-to-CO transition is not discontinuous in the model clouds.

5.5.5   Applying the Model to the Data

As we discussed in Sections 5.5.3 and 5.5.4, the observed far-IR, [C II], and H$_2$ (1,0) S(1) line intensities depend on n_H and I_{UV}, while the observed CO $J = 1 \to 0$ line intensity depends on n_H, I_{UV}, Z, and R_{cloud}. In this section, we apply the model results to the data and estimate n_H, I_{UV}, and R_{cloud} in the regions we observed.

I_{H_2} versus I_{CII}

In Table 5.8, the standard deviations of $\log(I_{H_2}/I_{CII})$ are relatively small ($0.1 - 0.2$) compared to those of other ratios ($0.2 - 0.4$), because f_{CII} and f_{H_2} depend similarly on n_H and I_{UV} (see Figure 5.12), and the [C II] and H$_2$ intensities are not very sensitive to spherical geometry effects, i.e., $2/3 < (\epsilon_{CII}, \epsilon_{H_2}) < 2$ (see Equation 5.29 and Figure 5.13).

In Figure 5.8, most of the data from NGC 2024 are within the model grids at $3.2 < \log n_H < 4.2$, and $1.5 < \log I_{UV} < 3$. There are positions (at $\Delta\alpha = -17'$, $-16'$, and $-15'$) in NGC 2024, however, where the I_{H_2} intensities lie at least a factor of 2.5 above the model grids. At these positions, the clouds

may be small enough to be transparent for H_2 emission from the back side of the cloud (see Equation 5.25). Although, based on our experience with other positions, it is extremely unlikely, we cannot exclude the possibility that the H_2 level populations at these positions are thermalized by effects present in high density PDR's ($n_H > 5 \times 10^4$ cm^{-3}) or by shocks (see Section 5.3.4) because these positions have not been observed in other H_2 lines, e.g., H_2 (6,4) Q(1). The ratios of $\log(I_{H_2}/I_{CII})$ in Orion are larger than those in NGC 2024. The Orion data in Figure 5.8 lie slightly below and slightly above models for $\log n_H$ = 4.7, implying that the gas density in Orion is higher than that in NGC 2024.

The mean ratios of $\log(I_{H_2}/I_{CII})$ in 30 Doradus, N159, and N160 are similar to each other, suggesting that the observed clouds in the LMC have similar densities, and that collisional de-excitations do not affect the H_2 level populations (see Table 5.8). In Figure 5.8, most of the data in the LMC are in the range of $3.7 < \log n_H < 4.7$ and $2 < \log I_{UV} < 3$.

By comparing the observed data and the model results in Figure 5.8, we measured the median density and far-UV field at each object. With this derived n_H and I_{UV}, we found the C$^+$ region depth, X_{C+} using Figure 5.11. The measured values of n_H, I_{UV}, and X_{C+} are listed in Table 5.10.

I_{CII} versus I_{CO}

Figure 5.14 demonstrates, using simplified chemical structures of clouds in the Galaxy and in the LMC, how cloud size differences and metallicity differences affect the observed I_{CII}/I_{CO} and the I_{H_2}/I_{CO} ratios. For the clouds in NGC 2024, the size of the clouds (R_{cloud}) in the western edge zone is smaller than in the cloud proper zone (See Section 5.4.1), while the depth of the C$^+$ region in the cloud is not much different. As we discussed in Section 5.5.4, with given n_H and I_{UV}, the observed I_{CO} is proportional to ϵ_{CO}. In the LMC, the dust-to-gas ratio, ρ_{dust}^{LMC}, is lower than in the Galaxy by the factor of ~ 4, and the far-UV

radiation penetrates much deeper inside the clouds:

$$\frac{X_{C+}^{LMC}}{X_{C+}^{GAL}} = \frac{\rho_{dust}^{GAL}}{\rho_{dust}^{LMC}} \simeq 4 \ . \tag{5.30}$$

If we assume the cloud size is same in the Galaxy and the LMC, the ϵ_{CO}^{LMC} is less than ϵ_{CO}^{GAL}. In other words, if $\epsilon_{CO}^{LMC} \simeq \epsilon_{CO}^{GAL}$, the cloud in the LMC is larger than the cloud in the Galaxy.

The I_{CII}/I_{CO} ratio is also affected by the strength of I_{UV}. Mochizuki et al. (1994) compared the $\log(I_{CII}/I_{CO})$ ratios in the LMC with the ratios in the Galactic plane. Their log-ratio in the LMC, 4.4 ± 0.3, agrees well with our ratio in 30 Doradus, N160, and N159 ($4.2 - 4.8$, see Table 5.8); however, their ratio in the Galactic plane, 3.1 ± 0.5, is much smaller than the ratio in Orion and NGC 2024 ($3.7 - 4.3$). We argue that the *Galactic plane* ($-12° < l < +26°$) has a different physical environment from active star formation regions like Orion and NGC 2024. Most of the $I_{60\mu m}/I_{100\mu m}$ ratios at the positions in the Galactic plane are between 0.2 and 0.3 (Figure 2 in Nakagawa et al. 1995). Applying these ratios to Equations 5.2, 5.5, and 5.7, we can estimate that the far-UV fields in the Galactic plane are in the range of $1.5 < \log I_{UV} < 1.7$ (see also Equation 5.32). The far-UV field is, therefore, much lower than toward the positions we observed in Orion and NGC 2024 ($1.9 < \log I_{UV} < 3.2$). Our model results in Figure 5.12 show that, at $\log I_{UV} = 1.6$ and $\log n_H = 3.7$, the $\log(I_{CII}/I_{CO})$ ratio is 3.2, which agrees with the observed value of the Galactic plane in Mochizuki et al. (1994). On the other hand, the far-UV fields in 30 Doradus, N160, and N159 are very high ($2.0 < \log I_{UV} < 3.8$). Even the extended regions in the LMC in which Mochizuki et al. (1994) measured the $\log(I_{CII}/I_{CO})$ ratio show higher far-UV fields ($1.8 < \log I_{UV} < 2.7$, derived from the $I_{60\mu m}/I_{100\mu m}$ ratios) than those in the Galactic plane. The more intense far-UV fields, e.g., in Orion, NGC 2024, 30 Doradus, N160, and N159, dissociate more CO molecules and have deeper X_{C+} in Equation 5.29; therefore, the I_{CII}/I_{CO} ratio is larger.

In Figure 5.9, we plot the observed data (I_{CII}/I_{FIR} versus I_{CO}/I_{FIR}), and overlay the results from planar cloud models and the spherical cloud models. The tick marks along dashed lines give the column density ($N_H(2R_{cloud})$) along the diameter of a cloud with the corresponding values of $\epsilon_{CII}f_{CII}$ and $\epsilon_{CO}f_{CO}$. The solid lines and dotted lines show the results of the planar cloud model (f_{CII} and f_{CO}). Only the data from the cloud proper zone in NGC 2024 are within the planar cloud model space, and most of the observed data deviate systematically toward lower I_{CO}/I_{FIR} or higher I_{CII}/I_{FIR} from the model results. The models do not include spherical geometry effects (see Section 5.5.3), and Equation 5.27 implies that the observed I_{CII} data should not be significantly affected by going from plane-parallel to spherical geometry. Therefore, the offset of observed points from the models on the I_{CII} versus I_{CO} plot in Figure 5.9 is solely a result of the effect of spherical geometry on the observed I_{CO} emission (ϵ_{CO}). Given the observed value of I_{CII}/I_{FIR}, we measured how much the observed I_{CO}/I_{FIR} is shifted from the point expected from the models for a given density and far-UV intensity on the model grids in Figure 5.9:

$$\Delta \log(I_{CO}/I_{FIR}) = \log \epsilon_{CO} \ . \tag{5.31}$$

Applying the measured X_{C+} and ϵ_{CO} to Equation 5.29, we derived the expected sizes of the spherical clouds (Table 5.10). For the data from the cloud proper zone in NGC 2024, we use the observing uncertainty to set the lower limit, i.e., $\epsilon_{CO} \geq 10^{-0.2}$.

I_{H_2} versus I_{CO}

Models indicate that, like I_{CII}, I_{H_2} is not affected strongly by changing from planar to spherical geometry. Therefore, the similar offset of the data from models in Figure 5.10 is probably due to the inappropriateness of plane-parallel models for predicting I_{CO}. As were the data in Figure 5.9, only the data from

the cloud proper zone in NGC 2024 are within the model space, and most of the observed data deviate systematically leftward from the model results.

The data from the SMC, which are not available in Figure 5.9, also deviate toward lower $\log(I_{CO}/I_{FIR})$ or higher $\log(I_{H_2}/I_{FIR})$ from the LMC model results, if we assume that the SMC models without the spherical geometry effects are not very different from the LMC models. The observed H_2 emission can be higher than the model results, because of the unreddened H_2 emission from the back side of the cloud. Because [C II] data are not available and the H_2 data are not certain, we cannot measure ϵ_{CO}^{SMC} from the I_{H_2} versus I_{CO} plane. We can still estimate a lower limit on the cloud size in the SMC, assuming $\epsilon_{CO} \geq 10^{-1}$. Applying the dust temperature of $10^{1.65}$ K from IRAS 60μm/100μm ratios (see Figure 5.7) to Equations 5.5 and 5.7,

$$\log I_{UV} = -5.65 + 5\log T_{dust} , \tag{5.32}$$

we obtain a far-UV field (I_{UV}) of $10^{2.6}$ at the observed positions in the SMC. Assuming $\log n_H = 3.7$, we get $N_H(X_{C+}^{SMC}) = 4.5 \times 10^{22}$ cm^{-2}. Therefore, the central column density (N_H) of the clouds in the SMC should be at least 1.3×10^{23} cm^{-2}(see Table 5.10).

5.5.6 Deduced Cloud Sizes

We estimated n_H and I_{UV} by comparing the observed data and the model results in the I_{H_2}/I_{FIR} versus I_{CII}/I_{FIR} plot (Figure 5.8). We take a median value of the data in each object except in N159 where we consider each position separately. Using the values of n_H and I_{UV} derived from Figure 5.8, we found X_{C+}, the depth from the surface of the cloud to the C$^+$-to-C-to-CO transition layer, in Figure 5.11. We also found ϵ_{CO}, the parameter of the spherical geometry effect, by comparing the data and models in Figure 5.9. When we do not have C$^+$ or H_2 data, we assumed that $\log n_H = 3.7$, and estimated I_{UV} from dust color temperature using $I_{60\mu m}/I_{100\mu m}$ and Equations 5.2 and 5.32. We

finally derived the sizes of clouds using Equation 5.29, and list them in Table 5.10 (see also Figure 5.15). The cloud sizes derived in this way measure the distance from the H $\textsc{ii}$/H boundary to the cloud center, not the overall scale of GMC complexes.

The cloud size measured in the western edge zone in NGC 2024 is at least a factor of 5 smaller than the size measured in the cloud proper zone in NGC 2024. At the four data positions in N159, the variations of n_H and I_{UV} are not significant, e.g., $3.7 < \log n_H < 4.1$, and $2.3 < \log I_{UV} < 2.7$; however, the I_{CO} intensities change by a factor of $10^{1.2}$, indicating that the cloud size varies more than a factor of 5 within the N159 region. The cloud sizes in the LMC ($N_H^{LMC} = 3 - 15 \times 10^{22}$ cm^{-2}) and the SMC ($> 1.3 \times 10^{23}$) are bigger than those in the Galaxy ($N_H^{GAL} = 1 - 4 \times 10^{22}$ cm^{-2}).

5.5.7 Cloud Size and Metallicity

Table 5.10 and Figure 5.15 show that the cloud size depends roughly linearly on metallicity and therefore the visual extinction through clouds is constant as one goes from the Galaxy to the LMC and SMC. This result contradict the assumption, in Figure 5.14, that the clouds in the LMC and the clouds in the cloud proper zone in NGC 2024 are same.

McKee (1989) presented the theory of *photoionization-regulated star formation*. According to his theory, the rate of low-mass star formation is governed by ambipolar diffusion in magnetically supported clouds, and the ionization of gas is mostly by far-UV photons. He suggested that the mean extinction of molecular clouds in dynamical equilibrium is in the range of $A_V = 4 - 8$ mag. Using Equation 5.18, the range of extinction corresponds to:

$$0.64 \times 10^{22} < \rho_{dust} \, N_H < 1.3 \times 10^{22} \, \text{cm}^{-2} \, . \qquad (5.33)$$

This range of column density roughly agrees with the empirical values of Galactic GMCs using I_{CO} and virial theorem: $N_H = 4 - 8 \times 10^{22}$ cm^{-2} (Scoville et

al. 1987; Solomon et al. 1987). Our data from the Galaxy, the LMC, and the SMC are also within $A_V = 4 - 16$ mag, and agree with the theory to within a factor of two.

5.6   Conclusions

The Magellanic Clouds have lower metal abundances than the Galaxy. Because of the lower dust-to-gas ratio, far-UV photons from massive-young stars in the Magellanic Clouds penetrate deeper into molecular material, dissociating more CO molecules. The CO luminosities from dwarf irregular galaxies, e.g., the Magellanic Clouds, are weaker than those from spiral galaxies. It has been suggested that the CO molecules could be completely dissociated in some clouds exposed by intense far-UV radiation ($I_{UV} > 10^3$) in the dwarf irregular galaxies (Maloney & Black 1988).

We observed H_2 (1,0) S(1), (2,1) S(1), and (5,3) O(3) lines from the Magellanic Clouds, and detected emission even in regions where CO had not been seen during the ESO-SEST Key Programme. With deeper CO observations, we also detected weak ($0.5 - 5$ K km s^{-1}) CO emission in PDRs where the previous ESO-SEST Programme did not detect CO $J = 1 \rightarrow 0$. We conclude that, in all regions where we could detect H_2, CO is not completely dissociated and that the CO $J = 1 \rightarrow 0$ emission is still optically thick in the Magellanic Clouds.

We ran a PDR code and a radiative transfer code with a range of densities, far-UV fields, and metallicities (for the Galaxy and the Magellanic Clouds). We simulate the observed line intensities from a plane-parallel cloud with a finite thickness whose front and back surfaces are exposed to external far-UV radiation, and from a spherical-shell cloud whose surface is exposed to homogeneous external far-UV radiation. The spherical-shell cloud model has effects ("spherical geometry effects") of limb-brightening and differences in the physi-

cal sizes of the C^+, H_2^*, and CO zones. Without the spherical geometry effects, the H_2, [C II], and CO line intensities from the plane-parallel cloud model are not very sensitive to the metallicity. With the spherical geometry effects, the H_2, and [C II] line intensities normalized to the far-IR intensity are also not very sensitive to the metallicity; however, the CO intensity is proportional to the surface area of the CO core. As we decrease the cloud size (or the hydrogen column density), the CO intensity normalized to the far-IR intensity decreases.

We compiled data of H_2 (1,0) S(1), CO $J = 1 \rightarrow 0$, [C II], and far-IR in the star formation regions in the Magellanic Clouds and in the Galaxy, and compared them with with simulated line intensities from a plane-parallel cloud. The data in the I_{H_2}/I_{FIR} versus I_{CII}/I_{FIR} plot agree with the model results, and show no significant difference between the Magellanic Clouds and the Galaxy. We use the I_{H_2}/I_{FIR} versus I_{CII}/I_{FIR} plot as an n_H and I_{UV} indicator at the position observed. In the I_{CII}/I_{FIR} versus I_{CO}/I_{FIR} plot and the I_{H_2}/I_{FIR} versus I_{CO}/I_{FIR} plot, the data from the western edge zone in NGC 2024 and from the Magellanic Clouds are shifted to the lower I_{CO} then the model results, which can be explained as an effect of the spherical geometry. We measured the amount of the effect, and derived the size of the clouds.

On galaxy scales, the derived average size of the clouds appears to increase as the metallicity of the galaxy decreases. Our observational result, that the mean extinction of clouds is constant and independent of their metallicity, is consistent with the idea that photoionization may play a role in regulating star formation.

Table 5.1. H_2 Lines and Instrument Parameters

H_2 Line	λ[a]	Date	θ_{ED}[b]	F[c]	m[d]	ΔV_{FWHM}[e]	ΔV_{BW}[f]
(5,3) O(3)	1.61308	1995 Oct.	81.0	23.0	125	104	163
(1,0) S(1)	2.12125	1995 Oct.	81.0	25.4	94	125	196
		1994 Dec.	88.9	26.4	94	120	189
(2,1) S(1)	2.24710	1994 Dec.	88.9	26.4	89	127	199

[a]Wavelength in air, in units of μm (Black & van Dishoeck 1987)

[b]Beam size (equivalent disk) in arcsec. The beam profiles are in Figure 5.1.

[c]Effective Finesse of the Fabry-Perot interferometer including the reflectivity, parallelism, surface quality, and incident angles

[d]Order of interference

[e]Full-width at half maximum of the instrument profile of an extended source.

[f]$\Delta V_{BW} = \int I(V)dV/I_{peak}$, in units of $km\,s^{-1}$. $I(V)$ is the instrument profile of an extended source.

Table 5.2.   Frequency Switching Parameters

Object	H_2 Line	ON		OFF	
		μm	$km\,s^{-1}$	μm	$km\,s^{-1}$
SMC	(5,3) O(3)	1.61386	+124	1.61506	+347
	(1,0) S(1)	2.12219	+112	2.12069	−100
LMC	(5,3) O(3)	1.61464	+274	1.61584	+477
	(1,0) S(1)	2.12321	+261	2.12171	+49
	(2,1) S(1)	2.24935	+249	2.24785	+49

Table 5.3.   Object List

Object[a]	α_{1950}	δ_{1950}	Reference
SMC-B1	00 43 35.0	−73 38 12	1
SMC-B2	00 46 15.9	−73 32 50	1
LIRS 36	00 44 50.5	−73 22 23	1
30 Dor	05 39 11.5	−69 06 00	2
N159/N160	05 40 18.2	−69 47 00	3

[a] (0, 0) Position

References. — (1) Based on the CO survey of the ESO-SEST Key Program (Rubio et al. 1993); (2) The CO peak (Poglitsch et al. 1995); (3) Center of the CO map in the N159/N160 region (Booth 1993; Johansson et al. 1994). Because the reference position of N160 is also N159 (0, 0) position, the center of N160 is close to the (-1, 7) position in this reference system.

Table 5.4.   Intensities from the Magellanic Clouds

Object	$\Delta\alpha$ [a]	$\Delta\delta$ [a]	H$_2$ [b] I	H$_2$ σ	CO [c] I	CO σ	C II [d] I	far-IR [e] I	T_{dust} [f] K	Ref. CO;C II
SMC-B1	0	-1	3.43	0.66	2.19	0.11	$\cdots$	0.432	49.4	2;
	0	0	1.60	0.66	2.39	0.11	$\cdots$	0.274	41.5	2;
SMC-B2	$+0.4$	-3.3	0.99	2.20	$\cdots$	$\cdots$	$\cdots$	$\cdots$	$\cdots$	
	0	0	2.4	1.1	0.584	0.073	$\cdots$	0.648	44.8	1;
LIRS 36	-3	0	1.33	1.77	$\cdots$	$\cdots$	$\cdots$	$\cdots$	$\cdots$	
	0	0	3.2	1.3	6.20	0.060	$\cdots$	0.330	42.2	1;
30 Dor	0	-1.5	4.2	2.7	2.87	$\cdots$	2.60	14.0	45.4	3;3
	-1.5	0	5.3	2.2	3.45	$\cdots$	4.15	18.3	50.6	3;3
	0	0	10.8	0.93	10.5	$\cdots$	8.10	35.2	75.0	3;3
	$+1.5$	0	8.6	2.4	2.23	$\cdots$	3.73	7.80	44.4	3;3
	0	$+1.5$	3.8	2.9	3.39	$\cdots$	2.85	6.57	42.0	3;3
	3	-9	0.94	0.75	$\cdots$	1.5	$\cdots$	1.36	43.3	4;
	0	-6	1.63	0.78	0.746	0.052	$\cdots$	2.63	42.8	1;
	-6	0	-0.28	0.53	$\cdots$	1.5	$\cdots$	1.21	55.5	4;
N159	-0.5	-5	2.1	1.5	25.0	0.14	$\cdots$	0.310	33.7	5;
	$+1$	-5	0.94	0.90	46.0	0.14	$\cdots$	0.323	34.8	5;
	-2.5	0	0.5	1.9	29.4	0.14	0.774	1.77	30.8	5;6
	-1.5	0	4.5	1.4	47.3	0.14	2.28	7.14	46.2	5;6
	0	0	3.23	0.99	7.70	0.052	2.45	8.21	41.9	1;6
	$+1$	$+1$	4.8	1.3	19.8	0.052	2.86	8.67	56.2	1;6
	0	$+3$	1.80	0.72	0.634	0.052	1.04	1.67	46.0	1;6
N160	0	$+4.5$	0.8	1.2	$\cdots$	4.3	0.492	1.16	37.4	5;6
	-2.5	$+7$	1.95	0.80	1.59	0.073	0.772	2.64	36.3	1;6
	-1	$+7$	6.45	0.91	9.89	0.073	2.04	15.1	76.0	1;6
	0	$+7$	2.46	0.71	5.82	0.073	1.70	6.47	53.7	1;6
	-2	$+8$	1.86	0.64	4.25	0.073	1.07	2.91	39.0	1;6
	0	$+8$	2.18	0.56	6.76	0.073	1.11	1.79	34.0	1;6
	-3	$+9$	-0.21	0.65	$\cdots$	4.3	0.677	0.971	34.9	5;6
	-1	$+9$	1.98	0.59	2.76	0.073	0.746	1.07	33.6	1;6
	-2	$+10$	1.72	0.51	1.64	0.073	0.547	1.00	45.8	1;6
	0	$+10$	2.05	0.52	3.86	0.073	0.361	0.751	42.8	1;6
	-1	$+12$	-0.6	1.3	4.49	$\cdots$	$\cdots$	0.705	40.6	5;

[a] Offset from the object (0, 0) position, in units of arcmin.

[b] Measured H$_2$ (1,0) S(1) intensity with the 1σ statistical uncertainty, in units of 10^{-6} ergs s^{-1} cm^{-2} sr^{-1}.

[c] Velocity integrated CO $J = 1 \rightarrow 0$ intensity, $I = \int T_R^* \, dv$, in units of K km s^{-1}. 1 K km s$^{-1} = 1.57 \times 10^{-9}$ ergs s^{-1} cm^{-2} sr^{-1}.

[d] [C II] intensities, in units of 10^{-4} ergs s^{-1} cm^{-2} sr^{-1}.

[e] IRAS Far-IR continuum intensity, in units of 10^{-2} ergs s^{-1} cm^{-2} sr^{-1}. See Equation 5.1.

[f] Dust temperature deduced from the ratio, $I_{60\mu m}/I_{100\mu m}$. See Equation 5.2.

References. — (1) This work; (2)Rubio et al. 1993; (3) Poglitsch et al. 1995; (4) Booth et al. 1993; (5) Johansson et al 1994; (6) Israel et al. 1996.

Table 5.5.   H$_2$ Line Ratios

Object	$\Delta\alpha$	$\Delta\delta$	(2,1) S(1)		(5,3) O(3)	
			Intensity[a]	Ratio[b]	Intensity	Ratio
SMC-B1	0	-1	$\cdots$	$\cdots$	0.76 ± 0.34	0.22 ± 0.11
	0	0	$\cdots$	$\cdots$	0.27 ± 0.36	0.17 ± 0.24
30 Dor	0	0	4.0 ± 1.5	0.37 ± 0.14	1.48 ± 0.37	0.138 ± 0.036
	$+1.5$	0	$\cdots$	$\cdots$	1.42 ± 0.51	0.166 ± 0.075
N159	$+1$	$+1$	$\cdots$	$\cdots$	0.65 ± 0.41	0.135 ± 0.091
N160	-1	$+7$	3.6 ± 1.9	0.56 ± 0.30	2.36 ± 0.41	0.366 ± 0.082

[a]Measured intensity with the 1σ statistical uncertainty in units of 10^{-6} ergs s^{-1} cm^{-2} sr^{-1}.

[b]Intensity ratio of the (2,1) S(1) line intensity to the (1,0) S(1) line intensity.

Table 5.6.   Comparing with Other H$_2$ (1,0) S(1) Data in N159

Ref.	Position[a]	Beam[b]	Ω[c]	Flux[d]	Intensity[e]
1	$(+1\rlap{.}'11, +0\rlap{.}'85)$	6×6	0.85	1.7	20
2	$(+1\rlap{.}'11, +0\rlap{.}'85)$	$\phi 13$	3.1	5.2	17
3	$(+1\rlap{.}'11, +0\rlap{.}'85)$	10×21	5.0	8.5	17
4	$(+1', +1')$	$\phi 81$	121	58	4.8

[a] Offset from the N159 (0, 0) position (see Table 3). $(+1\rlap{.}'11, +0\rlap{.}'85)$ corresponds to "N159 Blob" (Heydari-Malayeri & Testor 1985).

[b] Beam Size in units of arcsec. $\phi 13$ denotes $\theta_{ED} = 13''$.

[c] Solid angle of the beam in units of 10^{-9} sr.

[d] Flux in units of 10^{-14}ergs s^{-1} cm^{-2}.

[e] Intensity in units of 10^{-6}ergs s^{-1} cm^{-2} sr^{-1}.

References. — (1) Israel & Koornneef 1992; (2) Krabbe et al. 1991; (3) Kawara, Nishida, & Taniguchi 1988 (4) This work

Table 5.7.   Intensities from the Galactic Clouds

Object[a]	$\Delta\alpha$	$\Delta\delta$	H$_2$		CO	C II	far-IR	T_{dust}	Ref.[b]
			I	σ	I	I	I	K	CO;CII
Orion	+8	0	23	6	34.0	9.85	56.0	55.1	1;2
	+10	0	28	5	29.0	6.13	20.2	39.4	1;2
	+12	0	5.2	1.6	29.5	4.29	8.33	36.1	1;2
	+1.84	+9.83	27	4	60.7	4.50	40.9	41.6	1;3
NGC 2024:Edge	−17	0	9	1.9	13.4	5.60	3.26	36.3	4;4
	−16	0	12	3	18.6	6.70	4.72	37.1	4;4
	−15	0	13	2	14.4	8.60	4.87	37.3	4;4
	−14	0	3.3	1.2	6.70	5.00	4.29	36.6	4;4
	−13	0	4.5	1.8	15.6	4.70	4.40	35.2	4;4
	−12	0	6.4	1.9	51.0	5.60	6.60	38.1	4;4
	−11	0	8	2	84.6	6.30	10.4	40.6	4;4
NGC 2024:Prop	−9	0	9	3	110	8.80	18.5	49.4	4;4
	−8	0	6	3	132	10.5	15.2	42.9	4;4
	−6	0	8	3	154	10.4	26.4	47.4	4;4
	−5	0	11	4	130	9.90	55.4	51.5	4;4

[a] Orion (0,0): $\alpha_{1950} = 5^h32^m49\overset{s}{.}0$, $\delta_{1950} = −05°25'16''$ (θ^1 Ori C). NGC 2024 (0,0): $\alpha_{1950} = 5^h39^m14\overset{s}{.}0$, $\delta_{1950} = −01°57'00''$. *NGC 2024:Edge* and *NGC 2024:Prop* have the same (0, 0) position. See the text for the differences between NGC 2024:Edge and NGC 2024:Prop.

[b] H$_2$ data is from Luhman & Jaffe 1996

References. — (1) Schloerb & Loren 1982; (2) Stacey et al. 1993; (3) Luhman et al. 1997; (4) Jaffe et al. 1994

Note. — See the table footnotes in Table 4 for other columns.

Table 5.8. Intensity Ratios between H$_2$ (1,0) S(1), [C II], and CO $J = 1 \rightarrow 0$

Object	N[a]	$\log(I_{H_2}/I_{CII})$		$\log(I_{CII}/I_{CO})$		$\log(I_{H_2}/I_{CO})$	
		Avg.[b]	S. D.[c]	Avg.	S. D.	Avg.	S. D.
The Galaxy	15	-1.85	0.28	4.04	0.37	2.19	0.47
...Orion	4	-1.53	0.31	4.01	0.25	2.48	0.32
...NGC 2024:Prop	4	-2.08	0.13	3.68	0.03	1.61	0.14
...NGC 2024:Edge	7	-1.91	0.15	4.26	0.37	2.35	0.38
The LMC	17	-1.70	0.17	4.37	0.44	2.71	0.40
...30 Dor	5	-1.81	0.11	4.82	0.14	3.01	0.23
...N160	8	-1.59	0.18	4.18	0.21	2.59	0.20
...N159	4	-1.78	0.07	4.19	0.65	2.41	0.62
The SMC	4	$\cdots$	$\cdots$	$\cdots$	$\cdots$	2.89	0.40

[a] Number of observed positions.

[b] Average of $\log(I_{CII}/I_{H_2})$. I_{H_2}, I_{CII}, and I_{CO} denote line intensities of H$_2$ (1,0) S(1), [C II] 158 μm, and CO $J = 1 \rightarrow 0$.

[c] standard deviation (a measure of how widely values are dispersed from the average value) of $\log(I_{CII}/I_{H_2})$.

Table 5.9.   Input parameters for the PDR Code

Parameter	Galaxy	LMC	SMC[a]
N_H[b]	1	4	10
Z_C[c]	1	0.25	0.1
Z_O	1	0.25	0.33
ρ_{dust}[d]	1	0.25	0.1
ζ[e]	$5(-17)$	$5(-17)$	$5(-17)$

[a] Only for a standard model with $n_H = 5 \times 10^3 \mathrm{cm}^{-3}$ and $I_{UV} = 10^3$.

[b] H column density of the model cloud in units of $10^{22}\,\mathrm{cm}^{-2}$. $N_H = N(\mathrm{H}) + 2N(\mathrm{H}_2)$.

[c] Carbon and Oxygen abundances normalized to the Galactic values. Because the abundances are uncertain, we use simplified values in the model calculation: $[\mathrm{C}]^{GAL} = 1.6 \times 10^{-4}$, and $[\mathrm{O}]^{GAL} = 5 \times 10^{-4}$.

[d] Dust-to-gas ratio normalized to the Galactic value. $[\mathrm{A_V}/N_H]^{GAL} = 6.29 \times 10^{-22}$ mag/cm^{-2}, where $N_H = N(\mathrm{H}) + 2N(\mathrm{H}_2)$ (Bohlin et al. 1983; Black & van Dishoeck 1987).

[e] An atomic hydrogen cosmic-ray ionizing frequency, in units of s^{-1}.

Table 5.10. Derived Cloud Sizes

Object	N[a]	$\log n_H$	$\log I_{UV}$	$N(X_{C+})$[b]	ϵ_{CO}[c]	$N_H(2R_{cloud})$[d]
Galactic Plane[e]	$\cdots$	(3.7)	1.6	0.29	> 0.63	> 1.4
Orion	4	4.7	2.5	0.27	0.44	1.6
NGC 2024:Prop	4	3.7	2.5	0.45	> 0.63	> 4.3
NGC 2024:Edge	7	3.7	1.8	0.32	0.083	0.89
30 Dor	5	4.0	2.7	1.5	0.048	3.9
N160	8	4.2	2.7	1.5	0.17	5.0
N159$(-1.5, 0)$	1	4.1	2.7	1.5	> 0.63	> 15
N159$(+1, +1)$	1	3.9	2.7	1.7	0.36	8.4
N159$(0, 0)$	1	3.7	2.7	1.8	0.15	5.8
N159$(0, +3)$	1	4.1	2.3	1.2	0.063	3.2
SMC[e]	4	(3.7)	2.6	4.5	> 0.1	> 13

[a] Number of observed positions.

[b] Depth from the surface of the cloud to the C^+-to-C-CO transition layers in units of $10^{22}\,\mathrm{cm}^{-2}$.

[c] Parameter of the spherical geometry effect.

[d] The central column density of the spherical cloud in units of $10^{22}\,\mathrm{cm}^{-2}$. Note that $N_H(2R_{cloud}) = 2R_{cloud}n_H$, and $R_{cloud} = X_{C+} + R_{CO}$.

[e] We assume that $\log n_H = 3.7$. We derive $\log I_{UV}$ from IRAS far-IR data. See the text for details.
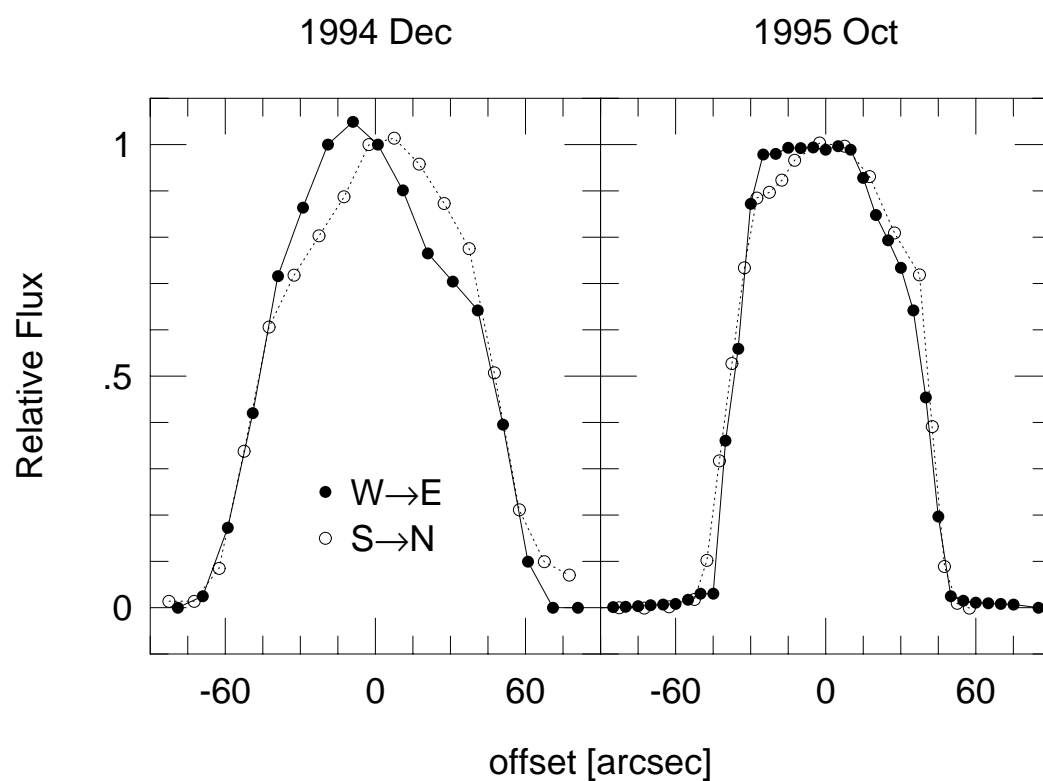
Figure 5.1.— Beam profiles of the University of Texas Near-Infrared Fabry-Perot Spectrometer at the CTIO 1.5 m telescope in 1994 December and 1995 October. We scanned the telescope across a bright star from west to east and from south to north.
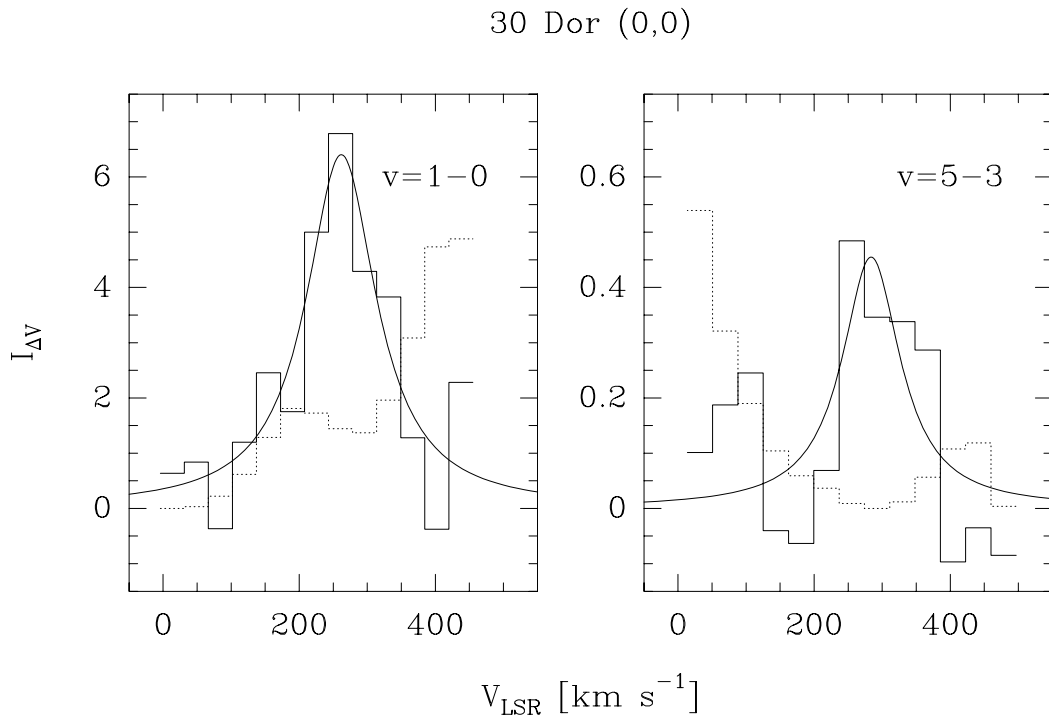
Figure 5.2.— Spectra of H_2 (1,0) S(1) and (5,3) O(3) emission lines (solid line) at the $(0,0)$ position of 30 Doradus in units of 10^{-8} ergs s^{-1} cm^{-2} sr^{-1} (km s^{-1})$^{-1}$. We fit the spectra with the instrument parameters using *GaussFit* (Jefferys 1990). The overlapped telluric OH lines (dotted line), measured at an off-source position, are scaled down by 20 on the H_2 (1,0) S(1) spectrum and by 100 on the H_2 (5,3) O(3) spectrum.
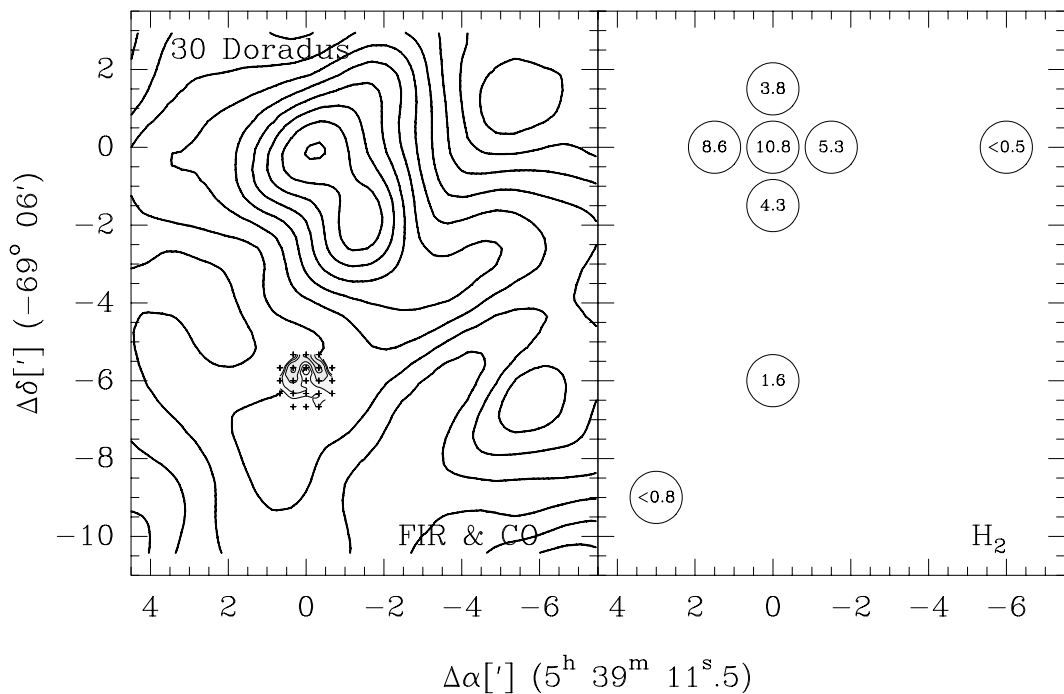
Figure 5.3.— Intensity maps of the 30 Doradus region. **Far-IR** *(thick lines on the left map)*: The contour intervals are in logarithmic scale: $0.398, 0.631, 1.00, 1.58, 2.51, 3.98, 6.31,$ $10.0, 15.8, 25.1, 39.8$ (i.e., $10^{0.2n}$, $n = -2, -1, ..., 8$) in units of 10^{-2} $\mathrm{ergs\,s^{-1}\,cm^{-2}\,sr^{-1}}$. The far-IR intensity is calculated using $I_{60\mu m}$ and $I_{100\mu m}$ in Equation 5.1. **CO** $J = 1 \rightarrow 0$ *(thin lines near (0, -6') on the left map)*: The contour values are in logarithmic scale: $0.398,$ $0.631, 1.00, 1.58$ $\mathrm{K\,km\,s^{-1}}$ (i.e., $10^{0.2n}$, $n = -2, -1, 0, 1$). The observed positions in CO are plotted as crosses. **H$_2$** (1,0) S(1) *(the right map)*: The H$_2$ intensities are plotted within the circles on the right map in units of 10^{-6} $\mathrm{ergs\,s^{-1}\,cm^{-2}\,sr^{-1}}$. The size of the circles are the equivalent-disk size of the UT FPS beam.
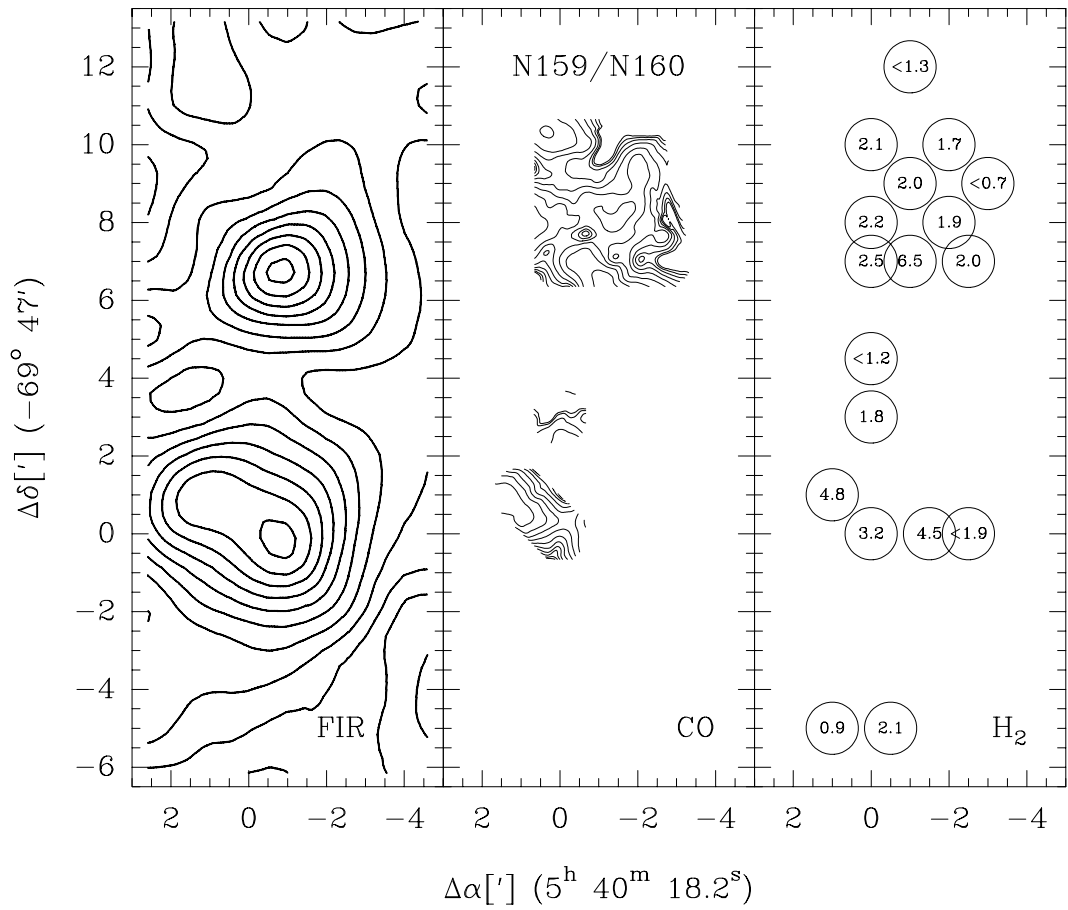
Figure 5.4.— Intensity maps of the N159/N160 region. **Far-IR**: The contour intervals are in logarithmic scale: 0.158, 0.251, 0.398, 0.631, 1.00, 1.58, 2.51, 3.98, 6.31, 10.0, 15.8 in units of 10^{-2} ergs s^{-1} cm^{-2} sr^{-1}. The far-IR peak at $(-1', +7')$ is near N160 and the peak at $(-1', 0)$ is near N159. **CO** $J = 1 \rightarrow 0$: See the caption in Figure 5.5. **H$_2$** (1,0) S(1): Same as in Figure 5.3.

CO in N159/N160
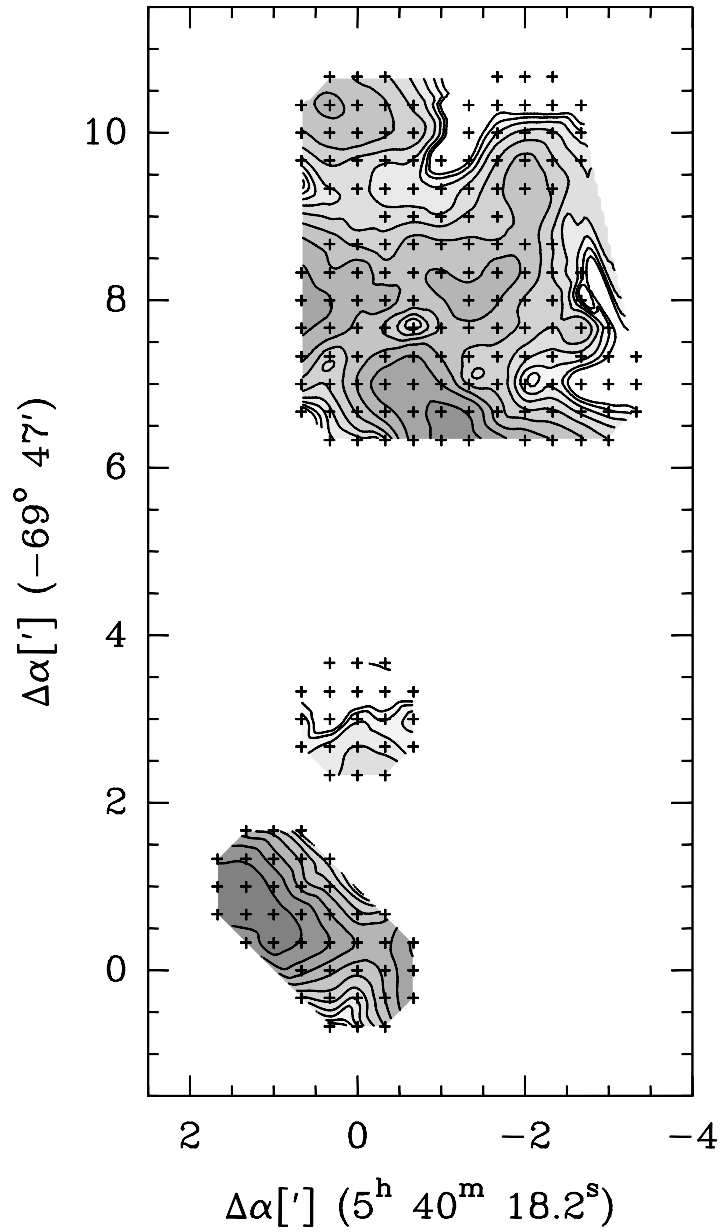
Figure 5.5.— CO $J = 1 \rightarrow 0$ intensity maps of the N159/N160 region. The contour values are in logarithmic scale: (for the $(-1', +8\rlap{.}'5)$ region) 0.398, 0.631, 1.00, 1.58, 2.51, 3.98, 6.31, 10.0, 15.8 K km s^{-1}; (for the $(0, +3')$ region) 0.398, 0.631, 1.00, 1.58 K km s^{-1}; (for the $(+0\rlap{.}'5, +0\rlap{.}'5)$ region) 0.398, 0.631, 1.00, 1.58, 2.51, 3.98, 6.31, 10.0, 15.8, 25.1 K km s^{-1}. The observed positions are plotted in plus signs.
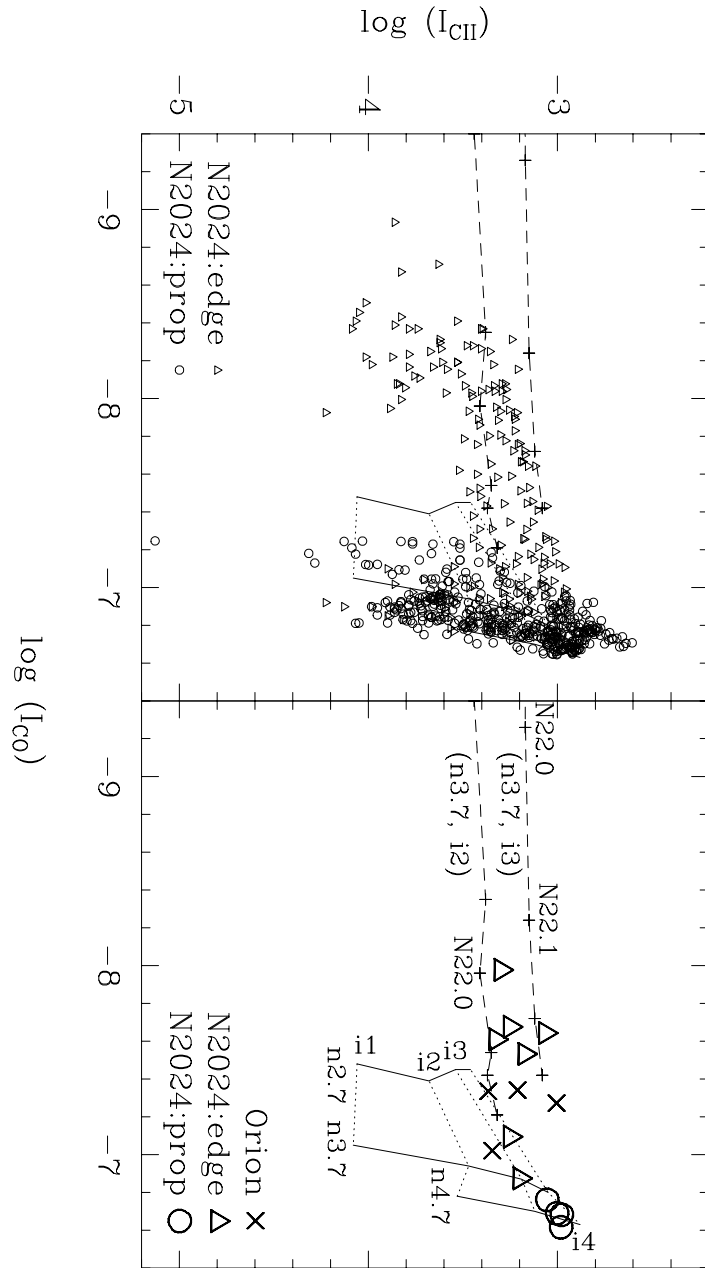
Figure 5.6.— [C II] 158 μm intensity versus CO (1,0) S(1) intensity in units of ergs s^{-1} cm^{-2} sr^{-1}. The left plot is replicated from Figure 4 in Jaffe et al. (1994). The right plot shows the distribution of the Galactic data which we are using in this work. We also overlay the results from the plane-parallel models, using the Galactic parameters. See Figures 5.8 and 5.9 for explanations.
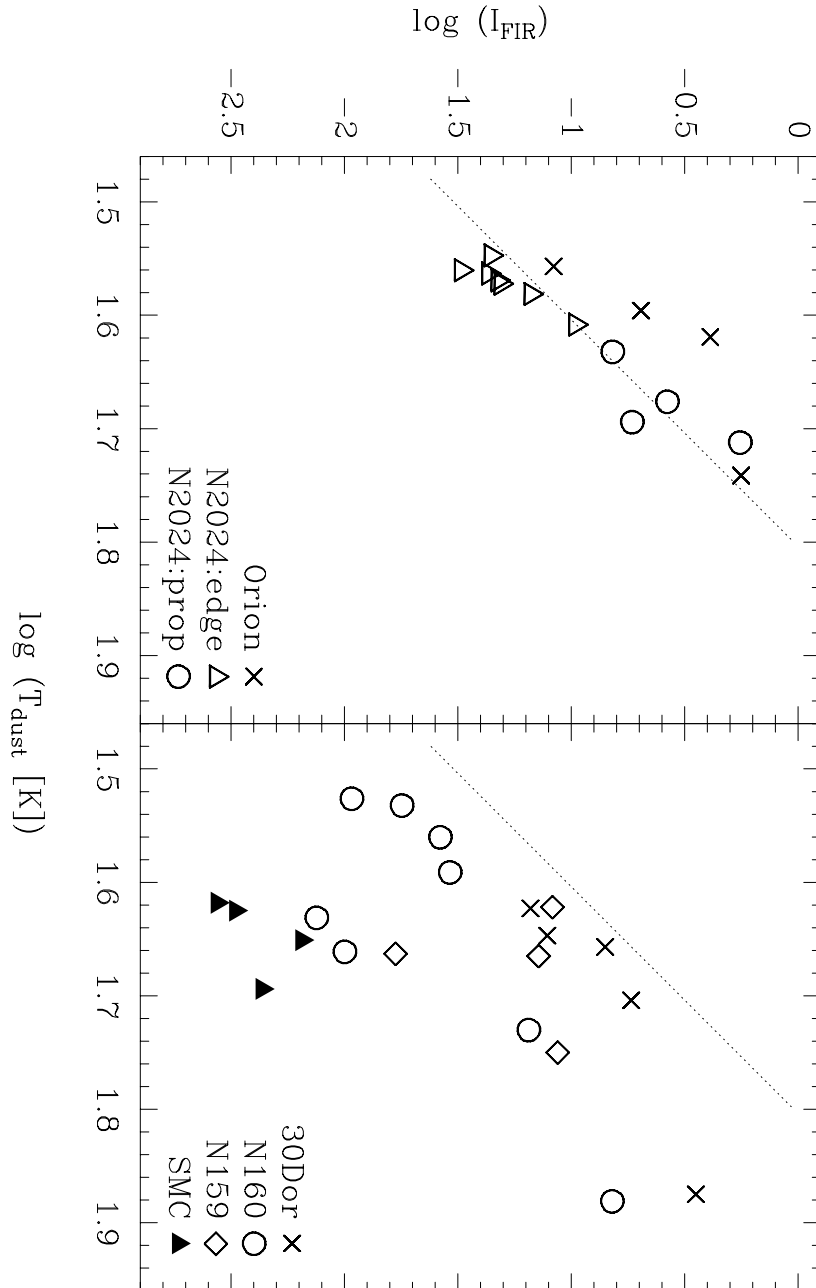
Figure 5.7.— far-IR intensities (Equation 5.1 and Tables 4 and 7) versus T_{dust} (Equation 5.2 and Tables 4 and 7). I_{FIR} is in units of $\mathrm{ergs\,s^{-1}\,cm^{-2}\,sr^{-1}}$. The data in the left plot are from the Galactic clouds and, in the right plot, from the LMC. The dotted line shows the model in Equation 5.7. We do not include the spherical geometry effect (ϵ_{FIR}, see Section 5.5.4) in the model calculation.
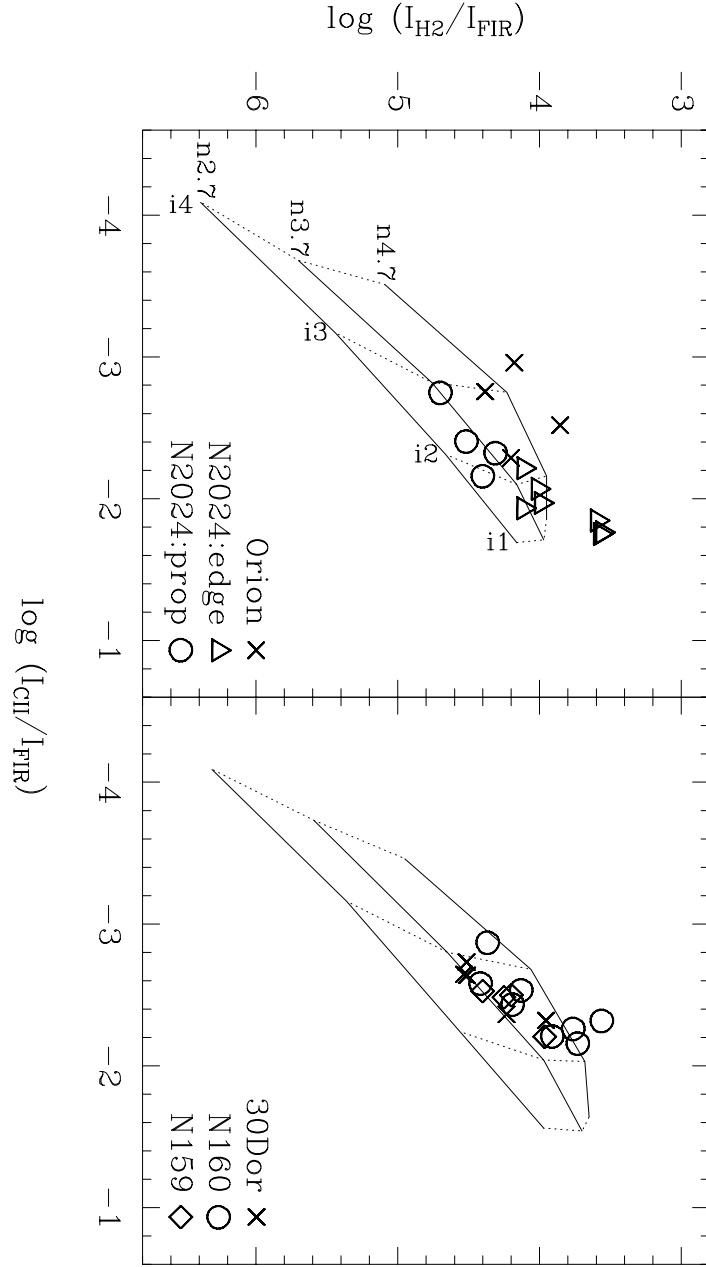
Figure 5.8.— I_{H_2}/I_{FIR} versus I_{CII}/I_{FIR}. The data in the left plot is from the Galactic clouds and the right plot from the LMC. We overlay the results from the two-sided plane-parallel models (see Section 5.5.3). We used the Galactic parameters for the model results in the left plot and the LMC parameters in the right plot (see Table 9 for the list of parameters). In the model grids, the solid-lines and the dotted lines connect the same n_H and the same I_{UV} respectively. $n3.7$ denotes $n_H = 5 \times 10^3 \mathrm{cm}^{-3}$, and $i3$ denotes $I_{UV} = 10^3$.
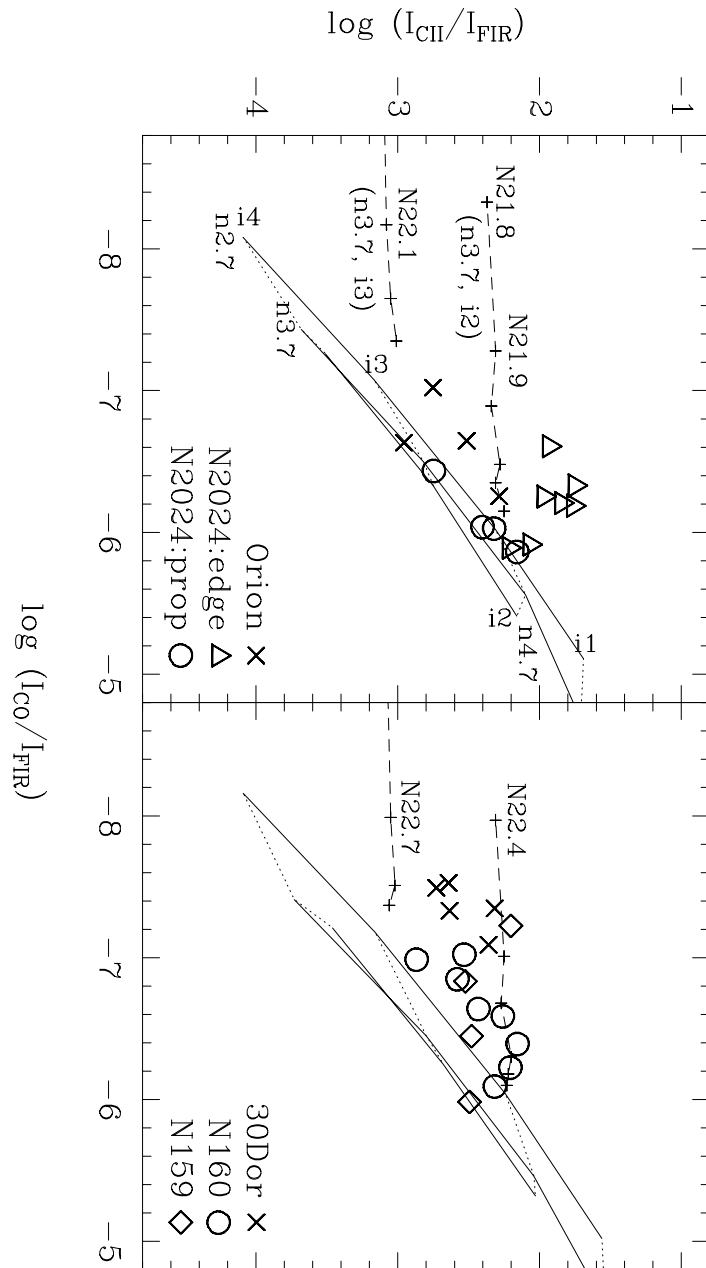
Figure 5.9.— I_{CII}/I_{FIR} versus I_{CO}/I_{FIR}. See Figure 5.8 for the explanations of the model grids of the solid lines and the dotted lines. We also plot models which include the effects of spherical geometry (shown as dashed lines, see Section 5.5.4). The dashed lines connect the spherical models with the same n_H and I_{UV} with different cloud sizes: the upper dashed line is for $n_H = 5 \times 10^3$ cm^{-3} and $I_{UV} = 10^2$; and the lower line for $n_H = 5 \times 10^3$ cm^{-3} and $I_{UV} = 10^3$. The plus sign on the dashed line marks the cloud size spaced by 0.1 in logarithmic-scale. $N22.3$ denotes $N_H(2R_{cloud}) = 2n_H R_{cloud} = 10^{22.3}$ cm^{-2}. Also see Figure 5.13 for another plot of these data.

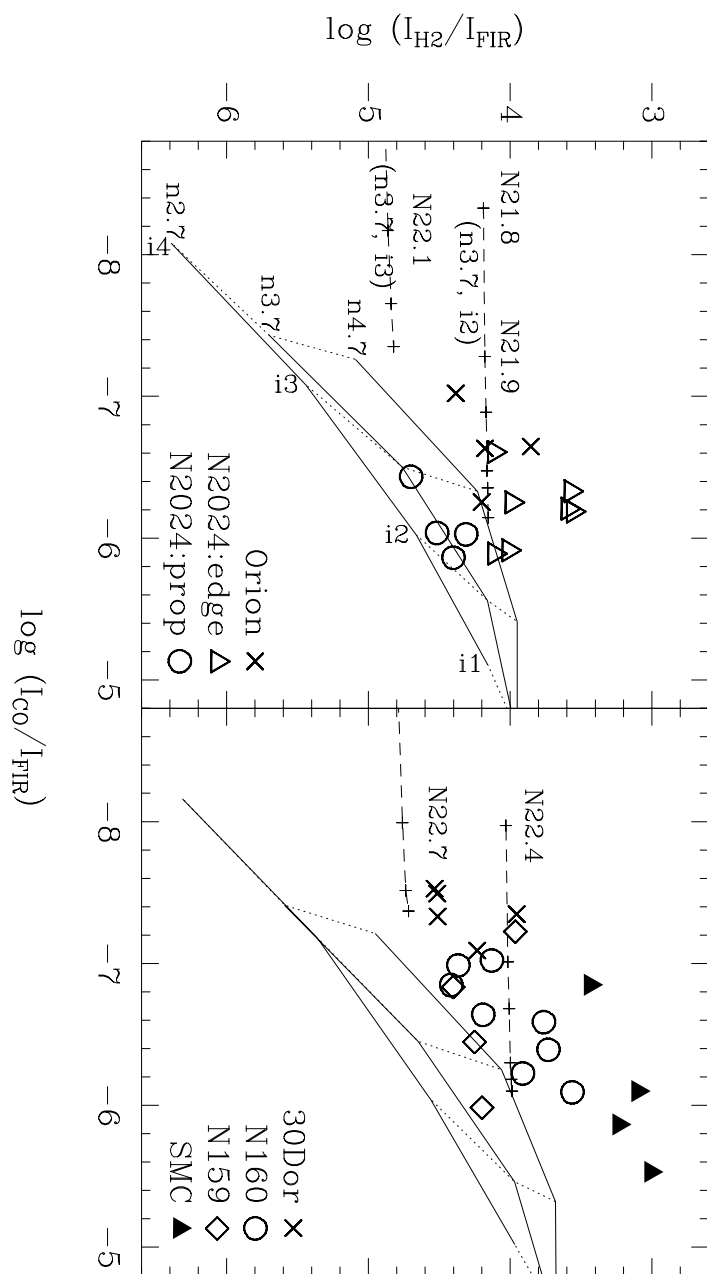Figure 5.10.— I_{H_2}/I_{FIR} versus I_{CO}/I_{FIR}. See Figures 5.8 and 5.9 for the explanations.
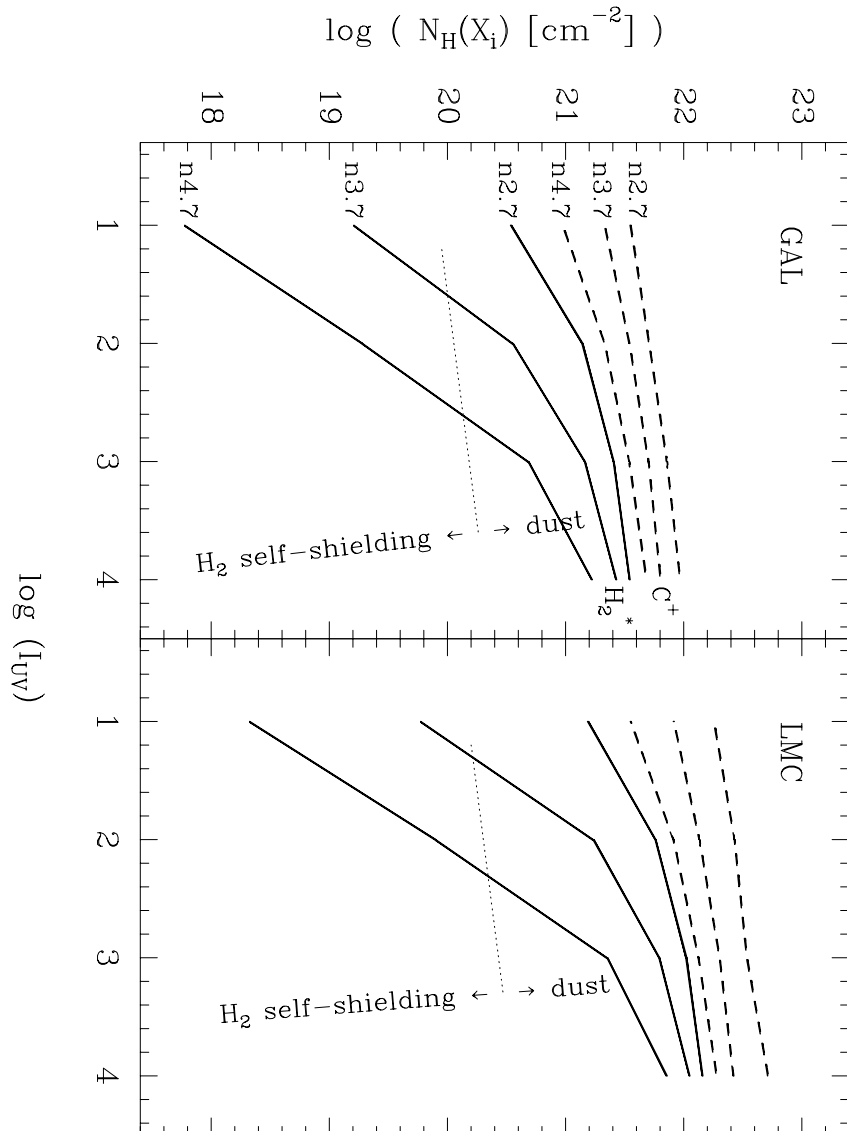
Figure 5.11.— I_{UV} versus the depths ($N_H(X) = X n_H$) from the surface of the cloud to the H-to-H$_2$ transition layer (where the abundance of H becomes same as that of H$_2$, shown as solid lines), and to the C$^+$-to-C-to-CO transition layers (where the abundance of C$^+$ becomes same as that of CO, shown as dashed lines). We changed the initial parameters, e.g., n_H, I_{UV}, and Z, for each model. $n2.7$ denotes $n_H = 5 \times 10^2$ cm^{-3}. At fixed density, the dashed lines and the solid lines show the change of X_{C+} and $X_{H_2^*}$ respectively. The dotted line divides the (I_{UV}, n_H, $X_{H_2^*}$) space into the H$_2$ self-shielding dominant space and the dust absorption dominant space (see Equation 5.20).
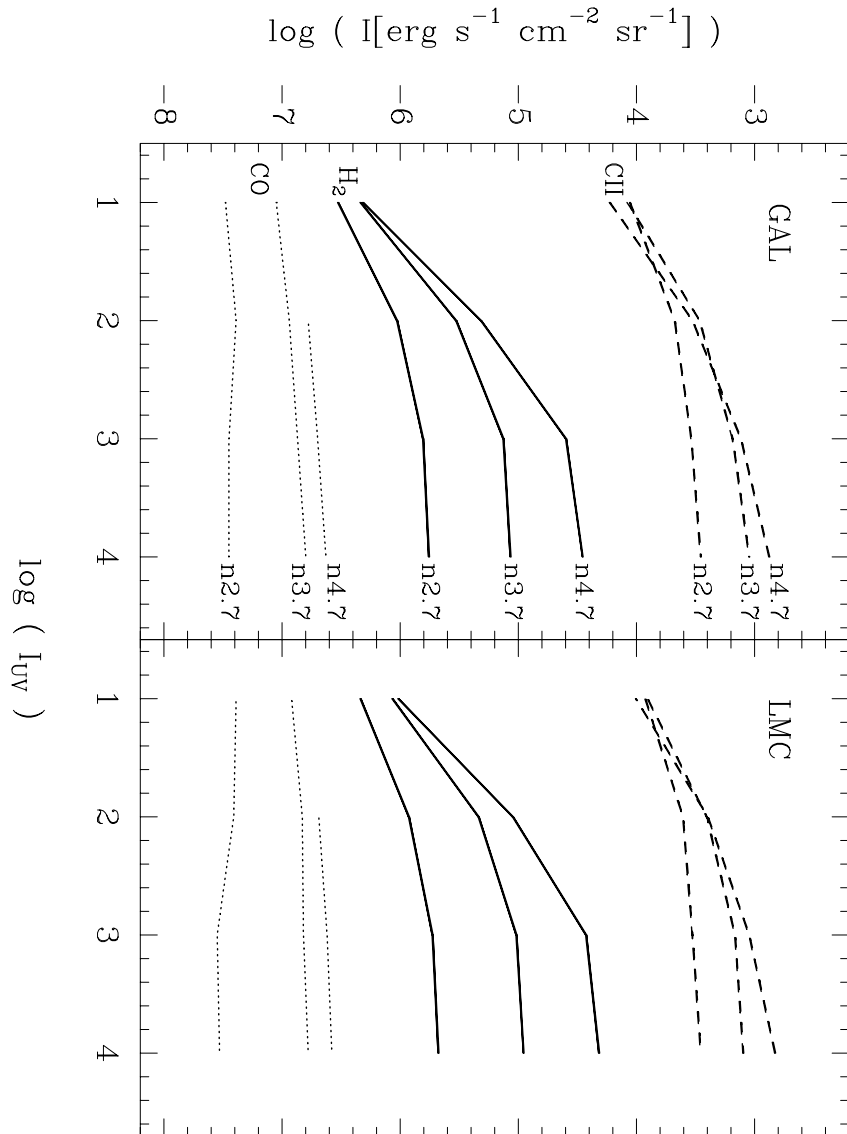
Figure 5.12.— I_{UV} versus [C II] (dashed line), H_2 (1,0) S(1) (solid line), and CO $J = 1 \rightarrow 0$ (dotted line) emission line intensities at fixed density. We assume that $\eta = 1$ and the intensities do not include the geometry effect ($\epsilon_i = 1$): $I_i = f_i(n_H, I_{UV}, Z)$.
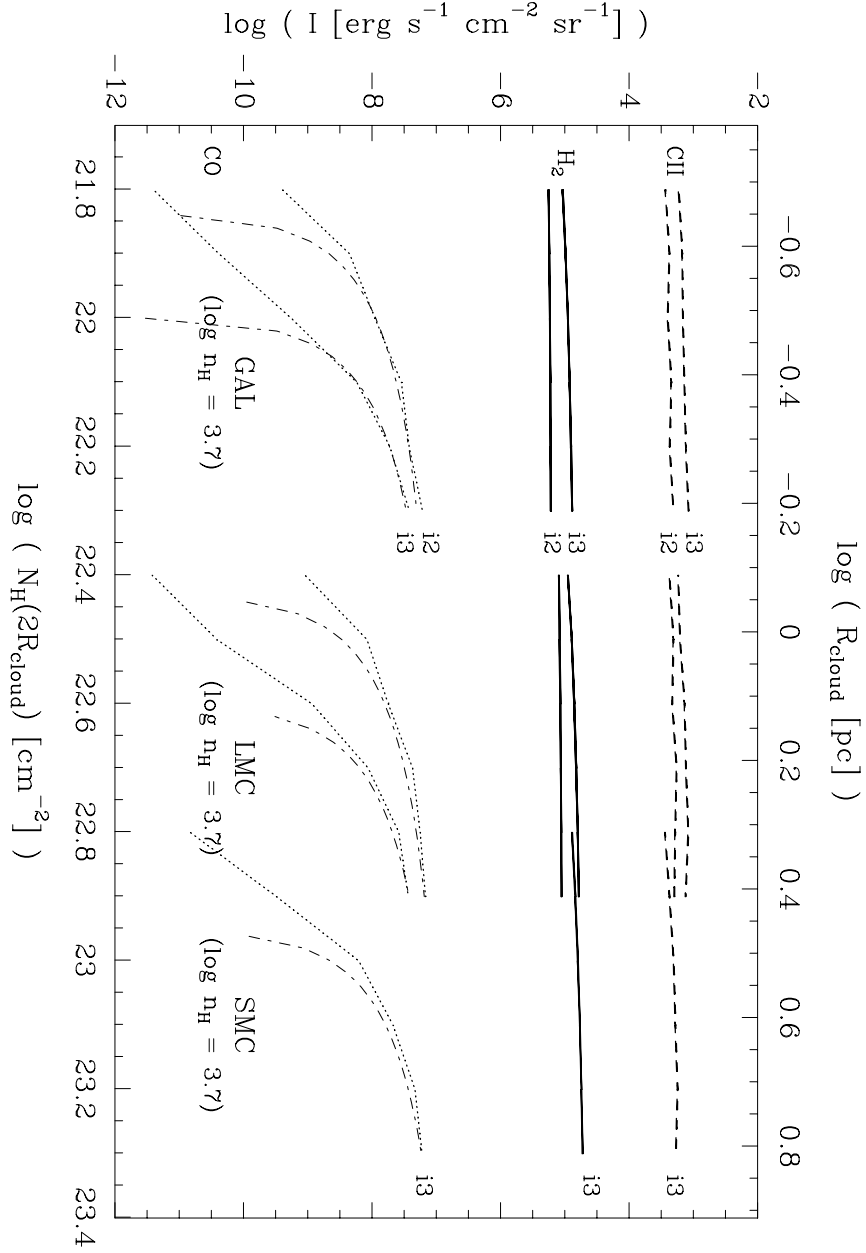
Figure 5.13.— [C II] (dashed line), H_2 (1,0) S(1) (solid line), and CO $J = 1 \rightarrow 0$ (dotted line) line intensities versus R_{cloud} at ($n_H = 5 \times 10^3$ cm^{-2}; $I_{UV} = 10^2$, 10^3). We assume that $\eta = 1$ and the intensities include the effect of spherical geometry: $I_i = \epsilon_i f_i(n_H, I_{UV}, Z)$. I_{CII} and I_{CO} are directly from the VT code, and I_{H_2} is from $\epsilon_{H_2} f_{H_2}$ with Equations 5.24 and 5.27. We also plot $I_{CO} = \epsilon_{CO} f_{CO}$ with Equation 5.29 (dash-and-dot line). We plot only the range of N_H where significant changes take place in each model. The upper axis shows the cloud radius in pc, and the lower axis the central column density of the spherical cloud in cm^{-2}: $N_H(2R_{cloud}) = 2R_{cloud} n_H$. Note that $N_H(X)$ in Figure 5.11 is $X n_H$, where $X_{C+} = R_{cloud} - R_{CO}$.
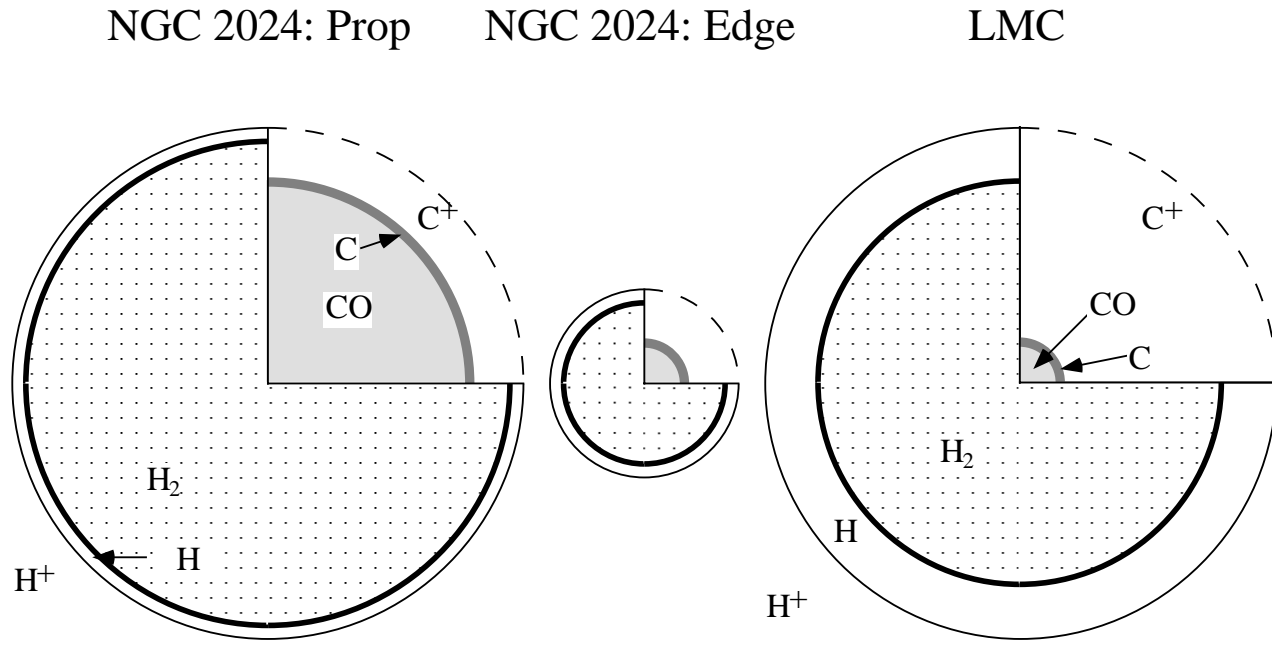
NGC 2024: Prop   NGC 2024: Edge   LMC

Figure 5.14.— Chemical Structures of Clouds. **The left** model is for the clouds in the cloud proper zone in NGC 2024, **the middle** one for the clouds in the western edge zone in NGC 2024, and **the right** one for the clouds in the LMC. We assume that the far-UV fields are same in the three cases. Note that our result shows that the average size of the clouds is inverse proportional to the metallicity of the galaxy (see Section 5.5.7).
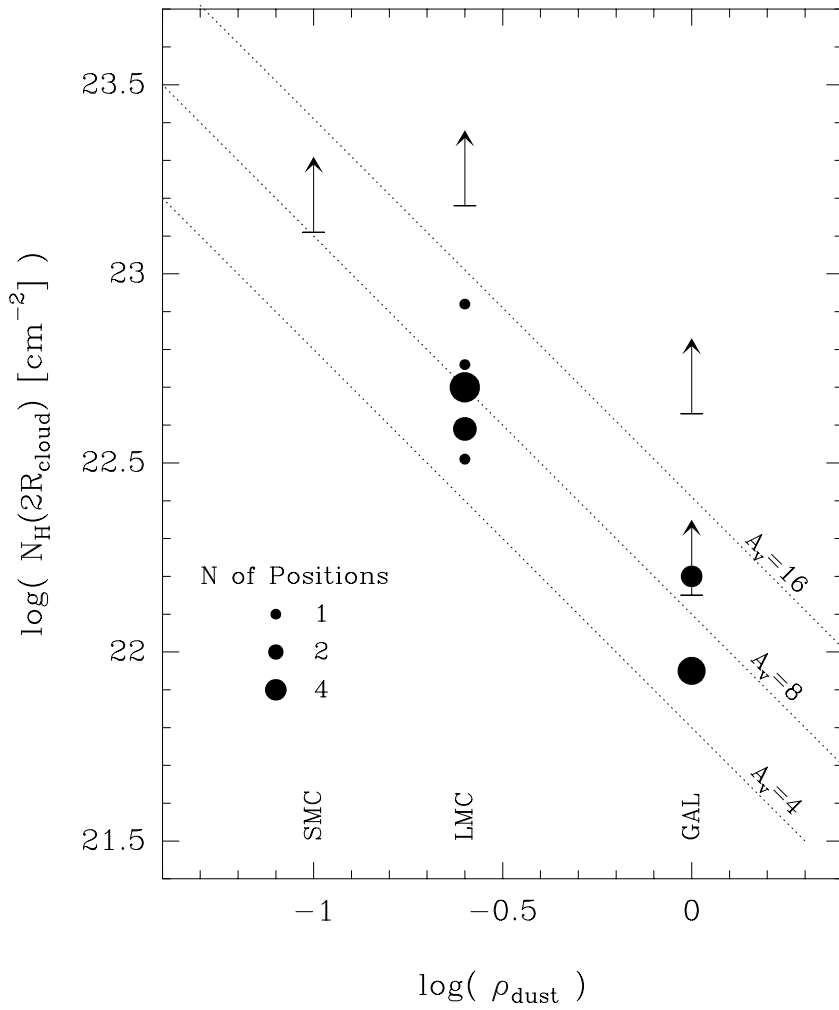
Figure 5.15.— Central column density of spherical cloud versus dust-to-gas ratio from the Galaxy, the LMC, and the SMC (see also Table 5.10). Note that: $N_H(2R_{cloud}) = 2R_{cloud}n_H$, and ρ_{dust} is normalized to the Galactic value. The area of the filled circle represents the number of observed positions. The arrow shows the lower limit. To compare with the theory of photoionization-regulated star formation, we overlay the constant optical depths at $A_V = 4, 8,$ and 16 mag.

REFERENCES

Anthony-Twarog, B. J. 1982, AJ, 87, 1213

Arimoto, N., Sofue, Y., & Tsujimoto, T. 1996, PASJ, 48, 275

Aumann, H. H., Fowler, J. W., & Melnyk, M. 1990, AJ, 99, 1674

Black, J. H., & van Dishoeck, E. F. 1987, ApJ, 322, 412

Bloemen, J. B. G. M., Strong, A. W., Blitz, L., Cohen, R. S., Dame, T. M., Grabelsky, D. A., Hermsen, W., Lebrun, F., Mayer-Hasselwander, H. A., & Thaddeus, P. 1986, A&A, 154, 25

Bohlin, R. C., Hill, J. K., Jenkins, E. B., Savage, B. D., Snow, T. P., Jr., Spitzer, L., Jr., & York, D. G. 1983, ApJS, 51, 277

Booth, R. S. 1993, in the Second European Meeting on the Magellanic Clouds, New Aspects of Magellanic Cloud Research, eds. B. Baschek, G. Klare, & J. Lequeux (Springer-Verlag), 26

Burton, M. G., Brand, P. W. J. L., Geballe, T. R., & Webster, A. S. 1989, MNRAS, 236, 409

Burton, M. G., Hollenbach, D. J., & Tielens, A. G. G. M. 1990, ApJ, 365, 620

Choi, M., Evans, N. J., II, Gregersen, E. M., Wang, Y. 1995, ApJ, 448, 742

Cohen, R. S., Dame, T. M., Garay, G., Montani, J., Rubio, M., Thaddeus, P. 1988, ApJ, 331, L95

Draine, B. T. 1978, ApJS, 36, 595

Draine, B. T. 1980, ApJ, 241, 1021

Draine, B. T., & Bertoldi, F. 1996, ApJ, 468, 269

Draine, B. T., & Lee, H. M. 1984, ApJ, 285, 89

Draine, B. T., Roberge, W. G., & Dalgarno, A. 1983, ApJ, 264, 485

Dufour, R. J. 1984, in IAU Symp. No. 108, Structure and Evolution of the Magellanic Clouds, eds. S. van den Bergh & K. S. de Boer (Dordrecht: Reidel), 353

Greve, A., van Genderen, A. M., Laval, A. 1990, A&AS, 85, 895

Habing, H. J. 1968, Bull. Astr. Inst. Netherlands, 19, 421

Helou, G., Khan, I. R., Malek, L., & Boehmer, L. 1988, ApJS, 68, 151

Heydari-Malayeri, M., & Testor, G. 1985, A&A, 144, 98

Hollenbach, D. J., & McKee, C. F. 1989, ApJ, 342, 306

Hollenbach, D. J., Takahashi, T., & Tielens, A. G. G. M. 1991, ApJ, 377, 192

Israel, F. P. 1988, in Proc. of an International Summer School held at Stirling in Scotland, Millimetre and Submillimetre Astronomy, eds. R. D. Wolstencroft & W. B. Burton (Kluwer Academic Publishers), 281

Israel, F. P., de Graauw, Th., van de Stadt, H., & de Vries, C. P. 1986, ApJ, 303, 186

Israel, F. P., & Koornneef, J. 1992, A&A, 250, 475

Israel, F. P., & Maloney, P. R. 1993, in the Second European Meeting on the Magellanic Clouds, New Aspects of Magellanic Cloud Research, eds. B. Baschek, G. Klare, & J. Lequeux (Springer-Verlag), 44

Israel, F. P., Maloney, P. R., Geis, N., Hermann, F., Madden, S. C., Poglitsch, A., & Stacey, G. J. 1996, ApJ, 465, 738

Jaffe, D. T., Zhou, S., Howe, J. E., Herrmann, F., Madden, S. C., Poglitsch, A., van der Werf, P. P., Stacey, G. J. 1994, ApJ, 436, 203

Jefferys, W. H. 1990, Biometrika, 77, 597

Johansson, L. E. B., Olofsson, H., Hjalmarson, Å, Gredel, R., Black, J. H. 1994, A&A, 291, 89

Jura, M. 1974, ApJ, 191, 375

Kawara, K., Nishida, M., Taniguchi, Y. 1988, PASP, 100, 458

Koornneef, J. 1984, in IAU Symp. No. 108, Structure and Evolution of the Magellanic Clouds, eds. S. van den Bergh & K. S. de Boer (Dordrecht: Reidel), 333

Krabbe, A., Storey, J., Rotaciuc, V., Drapatz, S., & Genzel, R. 1991, in IAU Symp. No. 148, The Magellanic Clouds, eds. R. Haynes & D. Milne (Kluwer Academic Publishers), 205

Lee, M. G., 1991, in IAU Symp. No. 148, The Magellanic Clouds, eds. R. Haynes & D. Milne (Kluwer Academic Publishers), 207

Li, W. 1997, Ph.D. Thesis, University of Texas at Austin (in preparation)

Luhman, M.L., & Jaffe, D.T. 1996, ApJ, 463, 191

Luhman, M. L., Jaffe, D. T., Keller, L. D., & Pak, S. 1994, ApJ, 436, L185

Luhman, M. L., Jaffe, D. T., Keller, L. D., & Pak, S. 1995, PASP, 107, 184

Luhman, M. L., Jaffe, D. T., Sternberg, A., Herrmann, F., & Poglitsch, A. 1997, ApJ, 482 (June 10 issue)

Maloney, P., & Black, J. H. 1988, ApJ, 325, 389

Maloney, P., & Wolfire, M. G. 1997, in Proc. of the 170th IAU Symp., CO: Twenty-Five Years of Millimeter-Wave Spectroscopy, eds. W. B. Latter, S. J. E. Radford, P. R. Jewell, J. G. Mangum, & J. Bally (Kluwer Academic Pub.), 299

McKee, C. F. 1989, ApJ, 345, 782

Mochizuki, K., Nakagawa, T., Doi, Y., Yui, Y. Y., Okuda, H., Shibai, H., Yui, M., Nishimura, T., & Low, F. J. 1994, ApJ, 430, L37

Mochizuki, K. 1996, Ph.D. Thesis, University of Tokyo

Nakagawa, T., Doi, Y., Yui, Y. Y., Okuda, H., Mochizuki, K., Shibai, H., Nishimura, T., Low, F. 1995, ApJ, 455, L35

Poglitsch, A., Krabbe, A., Madden, S. C., Nikola, T., Geis, N., Johansson, L. E. B., Stacey, G. J., & Sternberg, A. 1995, ApJ, 454, 293

Press, W. H., Teukolsky, S. A., Vetterling, W. T., & Flannery, B. P. 1992, in Numerical Recipes in C, 2nd Ed. (Cambridge University Press), 699

Oliva, E., & Origlia, L. 1992, A&A, 254, 466

Richter, M. J., Graham, J. R., & Wright, G. S. 1995, ApJ, 454, 277

Rieke, G. H., & Lebofsky, M. J. 1985, ApJ, 288, 618

Rubio, M., Lequeux, J., Boulanger, F., Booth, R. S., Garay, G., de Graauw, Th., Israel, F. P., Johansson, L. E. B., Kutner, M. L., & Nyman, L.-A. 1993, A&A, 271, 1

Schloerb, F. P., & Loren, R. B. 1982, in Ann. NY Acad. Sci., 395, Symposium on the Orion Nebula to Honor Henry Draper, eds. A. E. Glassgold, P. J. Huggins, & E. L. Schucking, 32

Scoville, N. Z., Yun, M. S., Clemens, D. P., Sanders, D. B., & Waller, W. H. 1987, ApJS, 63, 821

Solomon, P. M., Rivolo, A. R., Barrett, J., & Yahil, A. 1987, ApJ, 319, 730

Spaans, M., Tielens, A. G. G. M., van Dishoeck, E. F., & Bakes, E. L. O. 1994, ApJ, 437, 270

Stacey, G. J., Jaffe, D. T., Geis, N., Genzel, R., Harris, A. I., Poglitsch, A., Stutzki, J., & Townes, C. H. 1993, ApJ, 404, 219

Stacey, G. J., Townes, C. H., Poglitsch, A., Madden, S. C., Jackson, J. M., Herrmann, F., Genzel, R., & Geis, N. 1991, ApJ, 382, 37

Sternberg, A., & Dalgarno, A. 1989, ApJ, 338, 197

Störzer, H., Stutzki, J., & Sternberg, A. 1996, A&A, 310, 592

Tielens, A. G. G. M., & Hollenbach, D. 1985, ApJ, 291, 722

van Dishoeck, E. F., & Black, J. H. 1986, ApJS, 62, 109

van Dishoeck, E. F., & Black, J. H. 1988, ApJ, 334, 771

van Dishoeck, E. F., & Black, J. H. 1988, in Molecular Clouds in the Milky Way and External Galaxies, eds. R. L. Dickman, R. L. Snell, & J. S. Young (Springer-Verlag), 168

Westerlund, B. E. 1990, A&A Rev., 2, 29

Wilson, C. D. 1995, ApJ, 448, L97

Wolfire, W. G., Hollenbach, D., & Tielens, A. G. G. M. 1989, ApJ, 344, 770

Vita

Soojong Pak was born in Seoul, South Korea, on April 7, 1967, the son of Kwang-Hyun Pak and Bok-Hee Lee. He has an elder brother, Soo-Keun, and an elder sister, Suehee. After graduating from Joong-Ang High School, Seoul, in February 1986, he entered Seoul National University, Seoul, majoring in Astronomy. He received his degree of Bachelor of Science from Seoul National University in February 1990. He re-entered a junior course in the Department of Electrical Engineering and studied for a year, but he did not finish the degree course. In September 1991, he entered a Graduate Program in the Department of Astronomy in the University of Texas at Austin. He received his degree of Master of Arts in May 1994 from the University of Texas at Austin.

He married Soyoung Lee on June 22, 1991. She received her Doctor of Philosophy in the program of Foreign Language Education in the University of Texas at Austin in December 1995. She also received her Master of Art in the program of Instructional Technology from the University of Texas at Austin in May 1997. They have a daughter, Elaine Seoyoung Pak, who was born on August 4, 1994.

Permanent address: c/o Kwang-Hyun Pak
F-3 Kwang-Myung Villa
129 Dongsoong-Dong, Jongno-Gu
Seoul 110-510
South Korea

This dissertation was typed by the author.